University of Alberta

The Porgera gold deposit: Fluid characteristics, ore deposition processes, and duration of the ore forming event

by

Elisabeth Ronacher

A thesis submitted to the Faculty of Graduate Studies and Research in partial fulfillment of the requirements for the degree of Doctor of Philosophy

Department of Earth and Atmospheric Sciences

Edmonton, Alberta

Fall 2002

National Library of Canada
Bibliothèque nationale du Canada

Acquisitions and Bibliographic Services
Acquisitions et services bibliographiques

395 Wellington Street
Ottawa ON K1A 0N4
Canada

395, rue Wellington
Ottawa ON K1A 0N4
Canada

Your file Votre référence

Our file Notre référence

The author has granted a non-exclusive licence allowing the National Library of Canada to reproduce, loan, distribute or sell copies of this thesis in microform, paper or electronic formats.

L'auteur a accordé une licence non exclusive permettant à la Bibliothèque nationale du Canada de reproduire, prêter, distribuer ou vendre des copies de cette thèse sous la forme de microfiche/film, de reproduction sur papier ou sur format électronique.

The author retains ownership of the copyright in this thesis. Neither the thesis nor substantial extracts from it may be printed or otherwise reproduced without the author's permission.

L'auteur conserve la propriété du droit d'auteur qui protège cette thèse. Ni la thèse ni des extraits substantiels de celle-ci ne doivent être imprimés ou autrement reproduits sans son autorisation.

0-612-81260-X

Canada

University of Alberta

Library Release Form

Name of Author: Elisabeth Ronacher

Title of Thesis: The Porgera gold deposit: Fluid characteristics, ore deposition processes, and duration of the ore forming event

Degree: Doctor of Philosophy

Year this Degree Granted: 2002

Permission is hereby granted to the University of Alberta Library to reproduce single copies of this thesis and to lend or sell such copies for private, scholarly or scientific research purposes only.

The author reserves all other publication and other rights in association with the copyright in the thesis, and except as herein before provided, neither the thesis nor any substantial portion thereof may be printed or otherwise reproduced in any material form whatever without the author's prior written permission.

Elisabeth Ronacher

Marktstrasse 61
A-5582 St. Michael
Austria

Date: 08/30/2002

University of Alberta

Faculty of Graduate Studies and Research

The undersigned certify that they have read, and recommend to the Faculty of Graduate Studies and Research for acceptance, a thesis entitled The Porgera gold deposit: Fluid characteristics, ore deposition processes, and duration of the ore forming event by Elisabeth Ronacher in partial fulfillment of the requirements for the degree of Doctor of Philosophy.

Dr. Jeremy P. Richards (Supervisor)

Dr. Thomas Chacko (Committee Member)

Dr. Karlis Muehlenbachs (Committee Member)

Dr. Sarah Gleeson (Committee Member)

Dr. Clayton V. Deutsch (Committee Member)

Dr. Andrew R. Campbell (External Examiner)

Date: 3/7/2002

Abstract

This study focuses on ore formation at the Porgera gold deposit, Papua New Guinea. The duration of the ore-forming event was determined using the laser probe $^{40}Ar/^{39}Ar$ technique on magmatic and hydrothermal minerals, where the date on igneous biotite (5.99 ± 0.11 Ma) was interpreted to be the age of the intrusive event, and the average date obtained from two hydrothermal roscoelite samples (5.99 ± 0.08 Ma) is the age of ore formation. These results show that ore formation occurred within ≤0.1 my of intrusion.

Gold-bearing veins from a high-grade zone (North Zone) were characterized petrographically, and the fluid from which the vein material precipitated was investigated using fluid inclusion microthermometry, gas and ion chromatography, and stable isotope analysis (O, H, C) on vein quartz. The aim of these analyses was to study the evolution of the hydrothermal fluid along the North Zone and the process(es) by which this zone formed.

The veins consist dominantly of quartz but the main ore mineral, native gold, is intergrown with roscoelite [$K(V,Al)_2(AlSi_3O_{10})(OH,F)_2$], pyrite, and minor quartz. The vein centers are filled with anhydrite and carbonate. The homogenization temperature of primary inclusions hosted by quartz ranges from 127° ± 12°C (n = 37) to 165° ± 25°C (n = 27), and average salinities fall between 8 and 9 equiv. wt % NaCl where a minority of samples contains a low salinity group (~4 equiv. wt % NaCl) in addition to the higher salinity inclusions. Vapor-rich inclusions were observed to coexist with liquid-rich inclusions in a minority of samples. The microthermometric and petrographic data were used together with the results of the chromatographic analyses

as input parameters for numerical simulations of ore deposition using the software CHILLER. The modeling results indicate that stage II veins are most likely formed by cooling of a slightly acidic, oxidized fluid that had interacted with the surrounding sedimentary rocks. The observation of vapor-rich fluid inclusions suggesting that phase separation occurred during vein formation, and continuous salinity trends in some samples indicates that fluid mixing occurred locally. In addition, gold was observed in pyrite in the altered wall-rock. Hence, the results indicate that more than one precipitation mechanism was involved in vein formation. This result connects and integrates previous hypotheses of ore formation at Porgera.

Acknowledgements

A large number of colleagues and friends supported me during the last four and a half years. Although I am only naming a few of them here, I thank them all for their patience, tolerance, and willingness to share their ideas with me.

First and foremost, I am grateful to my supervisor Jeremy Richards who initiated a fantastic project and supported me over the years. He taught and encouraged me and waited patiently for the results of my work. I thank him for all he has done for me during the last four years, except that he continuously wanted me to watch Monty Python (in a country where torture is illegal!!).

I am indebted to the Porgera Joint Venture, not only for sponsoring the project, but also for generous support during my stays on the Porgera mine site and for continuous communication when I was not there and needed information. In particular, I thank Mike Johnston, Rod Henham, Shawn Crispin, Paul Adams, John Foley, Sonia Konopa, Tony Burgess, and John Butterworth. I would also like to express my gratitude to the PNG nationals who made my work at Porgera a fabulous experience: Phillip Winjat and Roger Redenut for drafting numerous cross sections and maps, Taki Pakapi for helping me in the core shed, and most of all Martin Torovi whose insight into the geology of the Porgera mine is extraordinary.

During the Ph.D. program I was financially supported by the Austrian Academy of Sciences and the Izaac Walton Killam Memoral Foundation. This support is greatly appreciated.

I am grateful to Paul Spry for his support from the first to the last minute and for having the patience to listen to me. I thank Tom Chacko for his support in difficult times, Karlis Muehlenbachs for the time he spent with me discussing parts of my thesis, and Sarah Gleeson for her enthusiastic and cordial support. Andy Campbell is thanked for his willingness to be my external examiner, for coming to Edmonton, and for his input in my thesis. I also thank Paul Kitto for the discussions on Porgera and for sharing his vast knowledge. I am indebted to Friedrich Koller who helped me on the way to Canada.

I am grateful to a number of collaborators who made my research possible. Mike Villeneuve (Geological Survey of Canada) let us use the Ar/Ar facilities, Colin Bray and Ed Spooner (University of Toronto) provided access to their lab and the expertise to use it. Most of all I thank Mark Reed (University of Oregon) for taking a month to introduce me to the wonders of thermodynamic modeling. Mark's inspiration is an incredible gift to me. Steve Taylor (University of Calgary), Chris Holmes (University of Saskatchewan) and Bob Drimmie (University of Waterloo) analyzed some of our samples which is greatly appreciated.

Finally I would like to thank all my friends and colleagues at the University of Alberta, especially Pedro Jugo whose support in every aspect made it possible to complete this thesis.

Contents

Chapter 1

Introduction 1
References 4

Chapter 2

Introduction 6
Geologic Setting 6
The Porgera gold deposit 7
Sample descriptions 8
Methodology 11
Results 12
    Igneous rocks 13
        Peruk 13
        Rambari 13
    Hydrothermal minerals 14
        Biotite 14
        Roscoelite 14
Discussion 14
    Age of the Porgera Intrusive Complex 14
    Age of ore deposition 16
    Life-span of magmatism and mineralization at Porgera 17
Comparison of K- and Ar-based dating techniques 18
Summary and conclusions 18
References 20
Tables 23
Figures 28

Chapter 3

Introduction 37
Samples 38
Vein textures 38
Analytical Techniques 39
Fluid Inclusions 39
Discussion 41
Conclusions 43
References 44
Tables 47
Figures 48

Chapter 4

Introduction 55
Geology of the Porgera gold deposit 57
    The Porgera Intrusive Complex 57
    Mineralization 57
Samples 60
Analytical Methods 60
    Fluid inclusion microthermometry 60
    Gas and ion chromatography 61
    Light stable isotopes 61
Results 63
    Fluid inclusion microthermometry 63
    Gas and ion chromatography 65
    Light stable isotopes 66
        Oxygen and hydrogen 66
        Carbon 67

Sulfur 67
Interpretation of analytical data 67
Fluid inclusion microthermometry 68
Fluid inclusion gas contents 70
Ion chromatography 71
Stable isotopes 71
Oxygen and hydrogen 71
Carbon 72
Sulfur 73
Observational constraints on fluid sources and hydrothermal processes 74
Bimodal salinity distribution 74
Observations indicating boiling 75
Observations indicating fluid mixing 76
Observations indication fluid sources 77
Numerical Modeling 81
CHILLER geochemical modeling – approach and limitations 81
Starting solution composition 82
Composition of the mixing solution 83
Assumptions and limitations of the method 83
Experimental models 84
Boiling 84
Fluid mixing 84
Cooling 85
Water – wall-rock alteration 85
Modeling Results and Interpretation 85
Boiling 85
Fluid mixing 86
Cooling 86
Water – wall-rock alteration 87
Interpretation of modeling results 87
Discussion 88

Porgera in the context of alkalic rock-related gold deposits 91
Common depositional mechanisms 91
Is Porgera unique? Implications for exploration for "Porgera-type"deposits 92
Conclusions 94
References 95
Tables 103
Figures 113

Chapter 5
Conclusions 131
References 132

List of Tables

Chapter 2

2.1 Apparent ages, MSWD values, and intercepts of the regression lines on the ordinate of the analyzed minerals

2.2 Chemical compositions of magmatic biotite and alteration biotite

2.3 Chemical compositions of roscoelite P41 and P43

2.4 Analytical details of the $^{40}Ar/^{39}Ar$ analysis

Chapter 3

3.1 Ice melting, salinity, and $Th_{(L)}$ values for liquid-rich fluid inclusions from boiling assemblages and from liquid-rich-only groups

Chapter 4

4.1 Ore and gangue mineralogy in stage II veins

4.2 Average homogenization temperatures and salinities of fluid inclusions hosted by stage II quartz

4.3 Results of gas chromatographic analysis

4.4 Results of ion chromatographic analysis

4.5 Oxygen and hydrogen isotope data

4.6 Carbon isotope data

4.7 Sulfur isotope data

4.8 Salinity data corrected for the presence of CO_2, and salinity values calculated based on the amount of Na^+ and Cl^-.

4.9 Input parameters for thermodynamic modeling

4.10 Chemical composition of the mixing solution

List of Figures

Chapter 2

2.1 Location of the Porgera gold mine

2.2 Schematic map showing surface expressions of individual intrusions from the Porgera Intrusive Complex

2.3 Total alkali silica diagram showing the positions of hawaiite (i.e. sodic trachybasalt) and mugearite (i.e. sodic basaltic trachyandesite)

2.4 Photomicrograph of the magmatic minerals dated for this study taken in plane polarized light

2.5 Photomicrographs of the hydrothermal minerals analyzed taken in plane polarized light

2.6 Inverse isochron plots and gas-release diagrams of sample 88-20

2.7 Inverse isochron plots and gas-release diagrams of hornblende (hbl) 88-15 from the Rambari alkali gabbro

2.8 Inverse isochron plots and gas-release diagrams of biotite P98-8 from the alteration selvage of early magnetite-sulfide±gold veins

2.9 Inverse isochron plots and gas-release diagrams of roscoelite (rosc) P42 (a) and P43 (b)

Chapter 3

3.1 Simplified map showing the location of the Porgera gold deposit, Papua New Guinea

3.2 Simplified sketch section at 22260E (mine grid) showing sample locations and sample numbers

3.3 Typical banded stage II quartz-roscoelite-gold vein

3.4 Photomicrographs showing coexisting primary liquid-rich and vapor-rich fluid inclusions in stage II quartz indicating boiling conditions

3.5 Histograms of (a) $Th_{(L)}$ (°C) and (b) salinity (equiv. wt. % NaCl) for liquid-rich primary fluid inclusions in quartz from boiling assemblages and from groups of liquid-rich only inclusions

3.6 Th-salinity plot of fluid inclusion data from stage II quartz

3.7 Pressure-temperature plot showing two CO_2 isochores an their intersection with the 160°C isotherm

Chapter 4

4.1 Map showing the location of the Porgera gold deposit

4.2 Simplified and schematic NS cross section through the deposit with sample locations

4.3 Photographs of hand specimens of stage II veins

4.4 Photomicrographs of stage II veins

4.5 Photomicrographs of fluid inclusions

4.6 Graph of homogenization temperature versus salinity of representative samples

4.7 Graph of homogenization temperature versus salinity of all samples

4.8 Histogram of all measure salinity data

4.9 Histogram comparing homogenization temperatures of samples containing liquid-rich only inclusions and coexisting liquid-rich and vapor-rich inclusions

4.10 Comparison of Br^-/Cl^- ratios of fluids from various environments

4.11 Graph of δD vs $\delta^{18}O$

4.12 CO_2-CH_4 solubility curve

4.13 $Br^-/Cl^- \times 10^3$ versus $I^-/Cl^- \times 10^3$

4.14 Modeling results for adiabatic boiling

4.15 Modeling results for fluid mixing

4.16 Modeling results for cooling

4.17 Modeling results for water—wall rock interaction

Chapter 1

Introduction

The subject of this thesis is the Porgera gold mine in Papua New Guinea. The deposit is famous for its high gold grades of up to 1000 grams/tonne. For the last fifteen years, exploration geologists and scientists have tried to explain the formation of this rich deposit. This work is thus building upon numerous previous studies (e.g., Handley and Bradshaw, 1986; Fleming et al., 1986; Richards, 1990a, b; Richards et al., 1990; Richards and McDougall, 1990; Richards, 1992; Richards and Kerrich, 1993; Wall et al., 1995), but investigates an area of the mine that has previously not been studied because drill core from this area has only been exposed during the last few years. The goal was to add to the understanding of ore-forming processes at Porgera because a number of apparently contradictory hypotheses were established previously. Unraveling the ore-forming mechanism leads to identification of parameters critical to ore formation and finally to models that can be used in the search for similar deposits, and the importance of such a models is therefore not restricted to the mine-scale but may have regional and even global implications.

The thesis is presented in paper format where each of the subsequent chapters consists of one individual paper. The first two papers have been published recently (Ronacher et al., 2000: chapter 3; Ronacher et al., 2002: chapter 2) and the third paper will be submitted shortly. In the second chapter, results of laser probe $^{40}Ar/^{39}Ar$ dating of magmatic and hydrothermal minerals are presented. Although the age of the igneous rocks that are associated with the deposit was established previously (Richards and McDougall, 1990), the ore-forming event was not well constrained, and the aim of this the dating work was to establish the duration of ore-forming event by dating minerals from the igneous host rocks and by analyzing the hydrothermal minerals from the earliest and latest vein-forming event. The laser probe technique was chosen because of its potential resolution that is necessary to achieve this goal. The results showed that both the intrusive event and ore formation occurred within less than 0.26 my where the resolution of the technique does not allow for a more accurate constraint. Thus, the

geologic events that we tie to ore formation need not last for millions of years for giant deposits to form (Stein and Cathles, 1997).

Apart from providing editorial assistance, J.P. Richards, first co-author of this paper (Ronacher et al., 2002), provided some of the sample material and allowed it to be re-analyzed using the laser probe technique. M.E. Villeneuve (Geological Survey of Canada, Ottawa) granted access to the $^{40}Ar/^{39}Ar$ geochronology laboratory at the Geological Survey of Canada, Ottawa and introduced the first author to the Ar laser probe technique. In addition, he was responsible for the sample preparation and the data reduction. M.D. Johnston, former chief geologist, Porgera Joint Venture, granted access to the Porgera mine and supported the study financially. The first author analyzed the samples in Ottawa, interpreted the data, and wrote the paper.

The third chapter reports the observation of vapor-rich fluid inclusions in quartz from gold-rich veins. Such inclusions imply that phase separation occurred during the formation of quartz and are therefore crucial for establishing a model for ore formation. Although this process has been postulated before, firm evidence in the fluid inclusion record was only produced during this study. In most cases vapor-rich inclusions are not hosted by quartz intergrown with gold but occur in quartz immediately overlying the roscoelite-gold band and phase separation can thus not be directly linked to ore deposition (for one exception see Ronacher et al., 2000b). Nevertheless, the presence of vapor-rich inclusions shows that the conditions for phase separation were favorable even at inferred depths of ore formation of 2.0 to 2.5 km. The co-authors of this paper (Ronacher et al., 2000a) are J.P. Richards who granted access to his fluid inclusion laboratory and trained the first author in fluid inclusion microthermometry analysis in addition to providing editorial assistance. M.D. Johnston provided access to the Porgera mine, allowed that sample material be shipped to Canada, and supported this study financially. The first author collected the samples, analyzed them, interpreted the data, and wrote the paper.

The work presented in the fourth chapter focused on a high-grade zone of the Porgera mine that was sampled along >600m with the aim of determining how this ore shoot formed and interpreting its formation in the light of previous hypotheses of ore formation. The gold-bearing quartz vein samples were analyzed

microthermometrically, isotopically (O, H, C, S), and by ion/gas chromatography with the goal of characterizing the chemical composition of the hydrothermal fluid that was responsible for gold-vein formation. The data collected were then used to numerically simulate ore deposition with the software CHILLER. The results show that more than one process was involved in ore formation, and it was possible to combine apparently contradictory previous hypothesis to one unifying model of ore formation.

The first co-author, J.P. Richards allowed access to his fluid inclusion laboratory and provided editorial assistance. M.H. Reed introduced the first author to numerical modeling at the University of Oregon and provided the software. C.J. Bray introduced the first author to gas and ion chromatography and helped with the data reduction. E.T.C. Spooner allowed access to the F.G. Smith Fluid Inclusion Laboratory at the University of Toronto. P.D. Adams, senior geologist, Porgera Joint Venture, provided assistance in the field. The first author conducted the microthermometric and chromatographic analyses as well as the numerical simulations, interpreted the data, and wrote the paper.

References

Fleming, A.W., Handley, G.A., Williams, A.L., Hills, A.L., and Corbett, G.J, 1986, The Porgera gold deposit, Papua New Guinea: Econ. Geol., v. 81, p. 660-680.

Handley, G.A., and Bradshaw, P.M.D., 1986, The Porgera gold deposit, Papua New Guinea, *in* MacDonald, A.J., ed., Gold '86: International Symposium on the Geology of Gold Deposits: Willowdale, Ontario, Konsult International, p. 416-424.

Richards, J.P., 1990a, Petrology and geochemistry of alkalic intrusives at the Porgera gold deposit, Papua New Guinea: J. Geochem. Exploration, v. 35, p. 141-199.

Richards, J.P., 1990b, The Porgera gold deposit, Papua New Guinea: Geology, Geochemistry and Geochronology: Unpulished Ph.D. Thesis, Canberrra, Australian National University, 106 p.

Richards, J.P., 1992, Magmatic-epithermal transition in alkalic systems: Porgera gold deposit, Papua New Guinea: Geology, v. 20, p. 547-550.

Richards, J.P., and Kerrich, R., 1993, The Porgera gold mine, Papua New Guinea: Magmatic hydrothermal to epithermal evolution of an alkalic-type precious metal deposit: Econ. Geol., v. 88, p. 1017-1052.

Richards, J.P., and McDougall, I., 1990, Geochronology of the Porgera gold deposit, Papua New Guinea: Resolving the effects of excess argon on the K-Ar and

$^{40}Ar/^{39}Ar$ age estimates for magmatism and mineralization: Geochim. Cosmochim. Acta, v. 54, p. 1397-1415.

Richards, J.P., Chappell, B.W., and McCulloch, M.T., 1990, Intraplate-type magmatism in continent-island-arc collision zone: Porgera intrusive complex, Papua New Guinea: Geology, v. 18, p. 958-961.

Ronacher, E., Richards, J.P., and Johnston, M.D., 2000a, Evidence for phase separation in high-grade ore zones at the Porgera gold deposit, Papua New Guinea: Mineralium Deposita, v. 35, p. 683-688.

Ronacher, E., Richards, J.P., and Johnston, M.D., 2000b, Evidence for boiling during ore deposition at Porgera, Papua New Guinea: Geological Society of America Program with Abstracts, vol. 32, p. A280.

Ronacher, E., Richards, J.P., Villeneuve, M.E., and Johnston, M.D., in press, Short life-span of the hydrothermal system at Porgera, Papua New Guinea: Laser $^{40}Ar/^{39}Ar$ dates for roscoelite, biotite, and hornblende: Mineralium Deposita Thematic Issue ("Gold Deposits Associated with Alkalic Rocks").

Stein, H.J., and Cathles, L.M., 1997, A Special Issue on timing and duration of hydrothermal events: Preface: Econ. Geol., v. 92, p. 763-765.

Wall, V.J., Munroe, S.M., Cameron, G.H., Heinrich, C.A., Cox, S.F., and Walshe, J.L., 1995, Porgera: plumbing and processes of gold mineralization, in Clark, A.H., ed., Giant ore deposits – II. Proceedings of the Second Giant Ore Deposits Workshop, Queens University, Kingston, Ontario, p 649-667.

Chapter 2

Short life-span of the ore-forming system at the Porgera gold deposit, Papua New Guinea: Laser $^{40}Ar/^{39}Ar$ dates for roscoelite, biotite, and hornblende

A version of this paper was published the Journal Mineralium Deposita, 2002, v. 37, p. 75-86. The co-authors are J.P. Richards, Department of Earth and Atmospheric Sciences, University of Alberta, Edmonton, Alberta T6G 2E3, Canada, M.E. Villeneuve, [2]Geological Survey of Canada, 601 Booth Street, Ottawa, Ontario K1A 0E8, Canada, and M.D. Johnston, Porgera Joint Venture, P.O. Box 484, Mt.Hagen, Papua New Guinea.

Introduction

The Porgera gold mine is located in the Pliocene fold and thrust belt of central Papua New Guinea (Fig. 2-1), and is one of the largest gold producers in the South Pacific region. Since the start of production in 1990 the mine has recovered 9.1 million ounces (Moz) of gold, with remaining proven and probable reserves of 9.8 Moz of gold at June 31, 2000.

The deposit is spatially associated with late Miocene (6.0 ± 0.3 Ma; Richards and McDougall, 1990) alkalic intrusions of the Porgera Intrusive Complex (PIC), and ore is hosted both by the intrusive rocks and the late Mesozoic sedimentary rocks into which the intrusions were emplaced. Relatively late, high-grade veins are hosted by extensional structures that cut the intrusive complex. The highest gold grades in excess of 1000 g/t occurred in Zone VII (now mined out), located in the Roamane Fault, a late normal fault that post-dates all intrusions (Fig. 2-2). Gold occurs in three mineralogically and microthermometrically distinct vein assemblages: magnetite-sulfide±gold veins, base-metal sulfide-carbonate veins with minor gold (stage I), and quartz-roscoelite-pyrite veins and breccias with native gold and Au-Ag-tellurides (stage II).

In addition to the spatial relationship between the ore deposit and the PIC, a temporal relationship between the intrusive and mineralizing events was predicted by Fleming et al. (1986) and Handley and Bradshaw (1986) and tested by Richards and McDougall (1990). Richards and McDougall (1990) dated hydrothermal sericite from alteration associated with stage I mineralization and roscoelite intergrown with gold in stage II veins using the K-Ar technique, but pure mineral concentrates in the amount required for K-Ar analysis could not be obtained, and the quartz contamination in roscoelite separates contained excess ^{40}Ar (probably in fluid inclusions). In addition, sericite and roscoelite are prone to Ar loss because they are extremely fine-grained, and therefore the broad age range for these minerals of 5.1 to 6.1 Ma obtained by Richards and McDougall (1990) probably reflects both the effects of excess ^{40}Ar and minor radiogenic ^{40}Ar loss.

In this paper, we readdress the question of longevity of the ore-forming hydrothermal system at Porgera by dating new samples of roscoelite from the youngest stage of veining, using the $^{40}Ar/^{39}Ar$ laser probe step-heating method. Samples of biotite from alteration selvages of the earliest veins were also dated in order to bracket the duration of the mineralizing event at Porgera. Magmatic hornblende and biotite from individual intrusions of the PIC were dated to confirm the original ages obtained using the furnace-based $^{40}Ar/^{39}Ar$ step-heating method.

Geologic setting

The Porgera gold deposit is spatially, temporally, and genetically associated with shallow level, mafic, sodic-alkalic intrusions, termed the Porgera Intrusive Complex (PIC; Fleming et al., 1986; Handley and Henry, 1990; Richards, 1990; Richards and McDougall, 1990; Richards et al., 1991; Fig. 2-2). In the absence of an appropriate classification scheme for hypabyssal rocks, Richards (1990) used the nomenclature for volcanic rocks (LeBas et al., 1986) and classified the intrusions as an alkali basalt—hawaiite—mugearite fractionation suite based on their sodic chemical composition (Fig. 2-3). The magmas were emplaced into late Cretaceous calcareous shales and

black (carbonaceous) mudstones and siltstones deposited on the margin of the Australasian continental plate (Chim Formation; Davies, 1983; Gunson et al., 2000). The depth of emplacement of the exposed intrusions is estimated to be approximately 2.5 km based on stratigraphic reconstructions (Davies, 1983, 1990; Fleming et al., 1986; Gunson et al., 1997). The intrusions occur as small balloon-shaped stocks with narrow contact halos (of a few meters to a few tens of meters) in the sedimentary rocks around them, and are interpreted to be apophyses derived from a much larger pluton at depth, as indicated by a circular aeromagnetic anomaly five kilometers in diameter (Fig. 2-2).

Although the chemical and petrologic compositions of the intrusions suggest a temporal evolution from mafic alkali basalts through intermediate hawaiites to relatively felsic mugearites, a clear temporal sequence of intrusions could not be determined from cross-cutting relationships. All intrusions are deuterically altered to variable degrees, and all intrusive phases appear to pre-date ore deposition because they host mineralized veins.

The Porgera gold deposit

Ore deposition at Porgera occurred in two main stages, preceeded by a subeconomic set of magnetite-rich veins. These pre-stage I veins occur in the deep central parts of the mine approximately 600 m below the bottom of the current open pit, and are characterized by magnetite-pyrite-chalcopyrite-pyrrhotite±gold in carbonate gangue with minor quartz. Preliminary microthermometric analyses on fluid inclusions in rare quartz indicate higher temperatures of formation of these veins (Th = 354 ± 43°C, n = 16) and higher salinity values (up to halite saturation at room temperature; Ronacher et al., 1999). The magnetite-sulfide veins are locally cross-cut by stage I veins and are therefore interpreted to represent an earlier, higher temperature stage of hydrothermal activity and mineralization. The alteration selvages around these veins contain fine-grained biotite, which has locally retrogressed to chlorite.

Stage I is characterized by disseminated auriferous pyrite and by base-metal sulfide-carbonate veins with pyrite, sphalerite, and galena as the dominant sulfides. Chalcopyrite is rare, and gold is present only in minor abundance as inclusions of native gold in pyrite and as refractory gold in arsenical pyrite. Complex Mn-Fe-Ca-Mg carbonates and minor quartz form the gangue material in these veins. Fluid inclusions in sphalerite and rare quartz in stage I veins exhibit an average homogenization temperature (Th) of 299° ± 33°C (n = 274) and a salinity of 9.5 ± 1.8 equivalent weight percent NaCl (equiv. wt. % NaCl). The trapping temperature was estimated to be ~ 325°C (Richards and Kerrich, 1993). Dominant alteration minerals in selvages around stage I base-metal sulfide-carbonate veins are fine-grained muscovite and illite and dolomitic carbonate.

Stage II, the main ore stage, consists of quartz-roscoelite (V-bearing mica, $K[V^{3+}, Al, Mg]_2AlSi_3O_{10}[OH]_2$) veins and breccia veins with pyrite, gold, and locally Au-Ag tellurides. A typical stage II vein is characterized by a rim of very fine-grained quartz, followed by a layer of fine-grained roscoelite intergrown with quartz, pyrite, and gold; these layers are overlain by barren, coarse-grained comb quartz, and vuggy centers are sometimes filled with Ca-Fe-Mg-Mn carbonate. Fluid inclusions in stage II comb quartz exhibit an average Th of 146° ± 13°C (n = 519) which is interpreted to be close to the trapping temperature because of local evidence for phase separation in stage II quartz (Richards and Kerrich, 1993; Ronacher et al., 2000) The inclusions define a bimodal salinity distribution with averages of 4.2 ± 0.3 (n = 104) and 7.8 ± 0.7 (n = 346) equiv. wt. % NaCl (Richards and Kerrich, 1993).

Sample descriptions

Six mineral separates of hornblende, biotite, and roscoelite, representing magmatic and hydrothermal minerals from five different samples, were selected for $^{40}Ar/^{39}Ar$ analysis (Table 2-1).

Igneous Rocks

Rambari Intrusion

Hornblende was separated from a gabbro cumulate from the Rambari intrusion in the center of the PIC (sample 88-15; Figs. 2-2, 2-4a). Richards (1990) suggested that the gabbroic intrusions represented the least evolved end member of a comagmatic fractionation suite based on whole-rock geochemistry. PIC magmas define apparent fractionation trends on diagrams of major element oxides versus SiO_2. Their SiO_2 contents are typically ~40-45 wt. % (Fig. 2-3), and rare earth and minor element patterns are identical to the patterns of the more felsic magmas of the PIC (hawaiites, mugearites). The gabbros contain clinopyroxene and olivine altered to carbonate and Fe-oxides. The hornblende is pleochroic from dark brown to yellowish brown, and is of magnesio-hastingsite composition (Richards, 1990). Poikilitic rims enclose clinopyroxene, apatite, magnetite, and plagioclase. The gabbro is variably altered, and hornblendes, where altered, are typically green as opposed to the brown color of the fresh hornblendes.

Peruk

Mineral separates of hornblende and biotite were analyzed from a porphyritic hawaiite intrusion from the Peruk area (sample 88-20; Figs. 2-2, 2-4b,c). This intrusion is of intermediate composition (47-50 wt. % SiO_2; Fig. 2-3) and is characterized by phenocrysts of clinopyroxene, apatite, magnetite, plagioclase, biotite, and hornblende. The brown hornblende displays oscillatory zoning and is typically overgrown by sub-ophitic dark brown rims. Locally, hornblende rims are altered to chlorite, but only unaltered grains were picked for analysis. Biotite is strongly pleochroic from dark brown to yellow-brown. Its composition is phlogopitic, as shown in Table 2-2.

Hydrothermal minerals

Biotite

Biotite from an alteration selvage from a magnetite-sulfide vein was separated in order to constrain the age of the oldest mineralizing event at Porgera (sample P98-8; Fig. 2-5a). This biotite is distinct from primary biotite in the intrusions because it is finer-grained and occurs pervasively dispersed in altered host alkali basalt. It is locally retrogressed to chlorite but only the freshest, least altered grains were selected by hand

picking. Alteration biotite is not only texturally but also compositionally distinct from primary magmatic biotite because it is richer in Cl (0.17 versus 0.05 wt. %; Table 2-2), whereas magmatic biotite is richer in Na_2O (0.79 versus 0.43 wt. %; Table 2-2) and total iron (FeO = 15.80 versus 13.19 wt. %; Table 2-2). The sample contains abundant disseminated magnetite and minor chalcopyrite, pyrite, and pyrrhotite.

Roscoelite

Roscoelite is intimately intergrown with gold and pyrite in stage II veins, and therefore its age represents the age of the gold mineralization. The stoichiometric formula of roscoelite is $K(V^{3+}, Al, Mg)_2AlSi_3O_{10}(OH)_2$ (Gaines et al., 1997) which is equivalent to muscovite except that the octahedral aluminum is partially substituted by V and Mg. However, Heinrich and Levinson (1955) observed on X-ray powder patterns that muscovite and roscoelite have different inter-layer spacings and therefore they concluded that roscoelite cannot be thought of as a vanadiferous muscovite but must be considered as a separate mineral. The optical properties of roscoelite were summarized by Wright (1914) who described roscoelite as an "olive-brown to green" mineral typically occurring as rosettes. The chemical composition of roscoelite from its type locality at the Stockslager gold mine, El Dorado County, California, is shown in Table 2-3 (Hillebrand et al., 1899).

Two roscoelite samples from Porgera were selected for age determination. Sample P41 is from a typical, layered, stage II quartz-roscoelite vein consisting of bands of very fine-grained quartz intergrown with very-fine grained crystals of light green roscoelite, followed by layers of green to brown rosettes of roscoelite intergrown with tetrahedrite, and overgrown by coarse grained comb quartz (Fig. 2-5b). In sample P43 bands of fine-grained roscoelite intergrown with pyrite in fine grained quartz alternate with bands of coarse-grained comb quartz (Fig. 2-5c). Both samples are from veins hosted by the HD3 intrusion (Fig. 2-2). The chemical compositions of the two roscoelite samples were determined using an electron micro-probe and representative analyses are shown in Table 2-3. Concentrations of V_2O_3 are up to 30 wt. %, and are higher than V_2O_3 concentrations in roscoelite from the type locality (Table. 2-3). The Porgera roscoelites contain up to 0.44 wt. % Cr_2O_3. No chromium analyses exist for the type-locality roscoelite for comparison, but compared to analyses of the vanadium mica from

the Hemlo gold deposit, Ontario, Canada, the Porgera roscoelite contains higher concentrations of Cr_2O_3 (Hemlo: average Cr_2O_3 = 0.23 wt. %, n = 10; Pan and Fleet, 1992).

Methodology

The CO_2 laser based $^{40}Ar/^{39}Ar$ step-heating technique used in this study shows significant advantages over the K-Ar, the furnace-based $^{40}Ar/^{39}Ar$ step-heating, and the $^{40}Ar/^{39}Ar$ single-step laser fusion methods (McDougall and Harrison, 1999; Villeneuve and MacIntyre, 1997): (1) potassium concentration does not have to be analyzed as in the K-Ar method, so no separate sample aliquot is required; (2) very small sample sizes are sufficient (e.g., 3-5 grains of mica of <1 mm in diameter for Mesozoic to Tertiary samples; less for older material) so that maximum purity of the separate can be more easily attained; (3) the relatively large beam diameter of the CO_2 laser allows even heating of the whole sample in controlled step-increments (as opposed to spot analyses); (4) the 10.6 μm wave length of the CO_2 laser couples well with most minerals used in Ar geochronology; and (5) the relatively small volume of the extraction system yields low Ar blanks (Hodges, 1998; McIntosh and Heizler, 1994).

Biotite and hornblende mineral separates for laser $^{40}Ar/^{39}Ar$ analysis were prepared by crushing the samples with a steel pestle and mortar, sieving to a grain size of 0.15 to 0.5 mm, and washing in an ultrasonic bath to remove fine dust adhering to the mineral grains. Heavy liquid separation was carried out using a mixture of tetrabromoethane and methylene iodide for samples 88-15 and 88-20, and the separates were washed in acetone and deionized water multiple times.

Roscoelite was drilled out of the hand specimens using a carbide-tipped drill. Those roscoelite samples intergrown with quartz were broken off the hand sample and crushed with an agate pestle and mortar. All samples were hand-picked under a binocular microscope in order to obtain pure separates. Roscoelite is typically finely intergrown with quartz, and the samples were hand picked to maximize roscoelite:quartz ratios. Grain size ranges from 0.1 to 1.0 mm.

At the Geological Survey of Canada laboratories (Ottawa, Ontario), about 20 to 40 grains of the separates were loaded into 3 mm x 3 mm aluminum foil packets along with a single grain of Fish Canyon Tuff Sanidine (FCT-SAN) to act as flux monitor (apparent age of 28.03 ± 0.18 Ma; Renne et al., 1994). The packets were placed into six tubes arranged radially in an aluminum can of 40 mm length × 19 mm diameter. Samples were irradiated for 2 to 12 hours at the research reactor of McMaster University, Hamilton, Ontario, in an approximate fast neutron flux of 4×10^{13} neutrons $cm^{-2}s^{-1}$. The J-factor was interpolated from up to ten monitors that were interspersed along the entire 40 mm length of the irradiation canister.

Upon return from the reactor, samples were split into two to three multiple-grain aliquots and loaded into individual holes of 4 mm depth × 1.5 mm diameter in a copper planchet. Each aliquot was independently step heated in 3 to 11 increments, from 0.1 to 20 % of the nominal laser power of 10 watts, using a Merchantek® MIR-10 10W CO_2 continuous laser (wave length = 10.6 μm) equipped with 2 mm × 2 mm flat-field lens, obviating the need for beam panning and allowing for step-heating of the whole aliquot by incrementally increasing the laser power (instead of total fusion of a spot). Data collection protocols follow those detailed in Villeneuve and MacIntyre (1997) and data reduction procedures for individual aliquots follow Roddick (1988) and Villeneuve and MacIntyre (1997) where the decay constant used is from Steiger and Jäger (1977). External error in the J-factor (± 0.5%, 1σ) is applied to the final age, but the uncertainty on the age of the flux monitor is not.

Results

Analytical results are presented in Table 2-4 and Figures 2-6 to 2-9. All results are reported with errors at the 2σ level of uncertainty unless otherwise stated. Gas-release plots containing all individual gas release steps are shown as inserts in the inverse isochron plots for illustration and comparative purposes (Roddick et al., 1980). Two to three aliquots of each sample were analyzed and the combined gas released is plotted

cumulatively on one diagram with the individual aliquots indicated in different shadings. The inverse isochron plots were constructed primarily using those steps that contained the highest proportion of radiogenic ^{40}Ar, and these steps are marked by arrows above the heating steps in the gas-release plots. All dates and uncertainties were calculated by regression through points representing the marked steps (Roddick, 1988; York 1969). The inverse isochron treatment provides a mechanism for delineation of any excess ^{40}Ar component and facilitates the interpretation of multi-component mixing data (Roddick et al., 1980).

Igneous rocks

Peruk

Both hornblende and biotite were analyzed from the sample from the Peruk area (sample 88-20). Biotite gave a date of 5.99 ± 0.11 Ma (MSWD = 3.7; Fig. 2-6a), excluding the two last steps of aliquot B. Although these two steps are relatively radiogenic, they appear disturbed relative to the steps in aliquot A. The individual steps exhibit relatively small errors, and the MSWD value of 3.0 is reasonable for $^{40}Ar/^{39}Ar$ laser step heating analyses.

All heating steps from the hornblende separate from sample 88-20 were used to calculate a date of 6.35 ± 0.23 Ma (MSWD = 1.0; Fig. 2-6b). The low MSWD value of 1.0 indicates excellent correlation of data points for this hornblende separate. The error on the calculated age is slightly larger than for the biotite, however, because of smaller concentrations of K in hornblende and consequently the smaller amounts of radiogenic ^{40}Ar relative to the trapped Ar and blank.

Rambari

The three aliquots of the Rambari hornblende separate gave reproducible results, although the highest temperature steps of aliquot A (steps at 5.0%-12.0% of the total laser power) show deviation from the mixing line derived from aliquots B and C (sample 88-15; Fig. 2-7; Table 2-4). The steps at 5.5% and 12.0% laser power appear to be dominated by atmospheric Ar, whereas the 5.0% step shows a component of excess ^{40}Ar ($^{40}Ar/^{36}Ar = 341 \pm 18$). Regression through the most radiogenic steps results in a five

point isochron date of 6.3 ± 0.7 Ma (MSWD = 2.6). Due to the relatively large error associated with this date, it is reported to one decimal place only.

Hydrothermal minerals

Biotite

Two aliquots of biotite from the alteration selvage of early magnetite veins were analyzed (sample 98-8). For calculation of the regression line, the two lowest and the two highest temperature steps of aliquot A and the three lowest temperature steps of aliquot B were omitted because they show the presence of either excess ^{40}Ar or are dominated by atmospheric Ar (Fig. 2-8). A date was determined by regression through the radiogenic steps and atmospheric Ar, yielding an apparent age of 5.98 ± 0.13 Ma (MSWD = 2.7).

Roscoelite

A date for stage II roscoelite of 5.92 ± 0.09 Ma (MSWD = 2.0; Fig. 2-9a) was obtained from sample P41, where the lowest temperature (≤ 2.3% laser power) and highest temperature (≥ 6.2% laser power aliquots A and C; ≥ 7.0% laser power aliquot B) steps of each aliquot were omitted from the regression line for similar reasons to above. For the second roscoelite sample (P43) only the least radiogenic steps scatter from the line, again suggesting the presence of small amounts of excess ^{40}Ar. However, the most radiogenic components display a relatively linear trend, and using these steps to calculate the regression line gives a date of 5.92 ± 0.17 Ma (MSWD = 2.0; Fig. 2-9b).

Discussion

Age of the Porgera Intrusive Complex

Richards and McDougall (1990) determined an average age for the PIC of 6.0 ± 0.3 Ma using the K-Ar and the furnace-based $^{40}Ar/^{39}Ar$ techniques. Their $^{40}Ar/^{39}Ar$ step-

heating spectra of hornblende were saddle-shaped indicating the presence of excess ^{40}Ar, which they discussed in detail. Nevertheless, the central parts of the spectra yielded plateaux, and Richards and McDougall (1990) used these plateaux to calculate ages for magmatic hornblende that were identical within error to the ~6.0 Ma ages for biotite obtained using the K-Ar technique.

As a check on these results using new laser sampling technology, three of the samples of magmatic hornblende and biotite dated by Richards and McDougall (1990) were re-analyzed in this study. Biotite from Peruk (sample 88-20) yielded a date of 5.99 ± 0.11 Ma (MSWD = 3.7; Fig. 2-6a), whereas hornblende from the same intrusion yielded a date of 6.35 ± 0.23 Ma (MSWD = 1.0; Fig. 2-6 b). Hornblende from the Rambari intrusion (sample 88-15) yielded a date of 6.3 ± 0.7 Ma (MSWD = 2.6; Fig. 2-7). At first glance, the hornblende samples appear to be older than the biotite. We do not believe that this apparent age difference is real, however, and argue that biotite is providing a more accurate age of magmatic emplacement for two reasons. Firstly, the low gas yields of the hornblende samples and the resultant relatively large errors, suggest that these dates should be viewed with caution. Secondly, hornblende in these samples is known to contain excess ^{40}Ar. Using the furnace-based $^{40}Ar/^{39}Ar$ step-heating method, Richards and McDougall (1990) were able to resolve the Ar spectrum from a large aliquot of hornblende from sample 88-15 into 19 steps, from which a well-defined inverse isochron age of 5.97 ± 0.19 Ma was calculated. This age agrees closely with those obtained by K-Ar and $^{40}Ar/^{39}Ar$ for magmatic biotite. We conclude that the smaller number of steps obtained from these hornblende samples by laser step-heating was insufficient to resolve fully the effect of excess ^{40}Ar in this case. Finally, it might be supposed that the younger dates returned by igneous biotites are due to overprinting by a hydrothermal event at ~6.0 Ma, which did not affect the hornblendes. However, the intrusive rock samples chosen for dating were selected specifically for their minimal degree of alteration, and biotites hand-picked from these samples are very fresh. Moreover, their compositions are distinct from those of hydrothermal biotites (Table 2-2). We therefore conclude that the biotite date of 5.99 ± 0.11 Ma provides the best estimate for the age of the intrusive complex.

Age of ore deposition

Based on K-Ar dating of alteration minerals, and K-Ar and $^{40}Ar/^{39}Ar$ dating of igneous biotite and hornblende, Richards and McDougall (1990) suggested that ore deposition at Porgera occurred within 1 m.y. of the time of emplacement of the PIC at 6.0 ± 0.3 Ma, but they were unable to constrain the timing of mineralization more precisely. The hydrothermal minerals analyzed in this study yield analytically well defined dates for early and late stages of ore deposition, and these dates help constrain the relationship between ore formation and magmatism.

Biotite P98-8 from the alteration selvage of an early magnetite-sulfide±gold vein yielded a date of 5.98 ± 0.13 Ma (MSWD = 2.7; Fig. 2-8). The inferred temperature of hydrothermal fluids in these veins (~350°C) is close to the Ar closure temperature in biotite (~250°–350°C; McDougall and Harrison, 1999), and therefore this date is interpreted to represent closely the age of alteration (rather than cooling), and by inference the age of mineralization. These veins are paragenetically the earliest in the deposit, and this date is therefore interpreted to reflect the age of the onset of mineralizing hydrothermal activity at Porgera.

The age of the main ore-bearing quartz-roscoelite-gold veins which represent the last significant pulse of mineralization, was determined by analyzing roscoelite. The best result was obtained from sample P41, which yielded a date of 5.92 ± 0.09 Ma (MSWD = 2.0; Fig. 2-9a); roscoelite P43 yielded an identical but slightly less precise date of 5.92 ± 0.17 Ma (MSWD = 2.0; Fig. 2-9b). Both dates are interpreted to reflect the age of formation of roscoelite from low temperature hydrothermal fluids (140°–160°C, based on inferred trapping temperatures measured in quartz from quartz-roscoelite veins; Richards and Kerrich, 1993; Ronacher et al., 2000), and their average age of 5.92 ± 0.08 Ma is considered to be the age of stage II ore deposition (weighted mean of the error calculated using the program ISOPLOT; Ludwig, 1991). The ages for alteration biotite and vein-hosted roscoelite overlap within error, which suggests that the different stages of ore formation were separated by less than 0.26 m.y.

Life-span of magmatism and mineralization at Porgera

No age difference could be resolved between the individual intrusions of the PIC in this study or in the previous study by Richards and McDougall (1990), suggesting that the intrusions cooled quickly (probably within 0.1 m.y. of emplacement). Such a result is geologically reasonable given the small size of the intrusions (≤500 m in diameter) and their isolated, shallow-level emplacement into wet, poorly consolidated sediments (peperitic contacts are commonly observed). The short cooling period of the PIC is also consistent with results on the solidification of plutons obtained by Jaeger (1968) and with the modeling of Shinohara and Hedenquist (1997), who showed that a 5 km-thick magma chamber would crystallize within 120,000 years, whereas a chamber of 1 km thickness would solidify in only 6000 years. Results on the same order of magnitude were obtained by Marsh et al. (1997), who suggested based on numerical models that an intrusion 500 m in diameter would cool within less that 40,000 years, and that hydrothermal circulation would have the effect of shortening that time span. Cathles et al. (1997) also showed that if hydrothermal circulation occurred, even large intrusions would cool "in at most a few tens of thousands of years".

The duration of the mineralizing system at Porgera is constrained by the age of hydrothermal biotite from alteration associated with early high-temperature magnetite-sulfide-gold veins, and the age of roscoelite that is intimately intergrown with gold in late quartz-roscoelite-gold veins and breccias (5.98 ± 0.13 Ma and 5.92 ± 0.08 Ma respectively). Hydrothermal activity continued beyond this stage, but is manifested only by deposition of barren quartz and carbonate veins, and late sulfate (anhydrite) veins.

The ages of hydrothermal biotite and roscoelite overlap within error, and also overlap with the age of magmatism (5.99 ± 0.11 Ma), indicating that the combined duration of the intrusive and mineralizing events at Porgera was ≤0.26 m.y. This result is comparable to estimates for the duration of hydrothermal activity at the Far South East and Lepanto deposits, Philippines (<0.25 m.y.; Arribas et al. 1995). Furthermore, the result is in agreement with Marsh et al.'s (1997) conclusion that the life-span of

many hydrothermal systems cannot be resolved with currently available geochronological techniques.

Comparison of K and Ar-based dating techniques

Three techniques based on the radioactive decay of ^{40}K were used in an attempt to constrain the age of magmatic and hydrothermal minerals by Richards and McDougall (1990) and in this study. Each of these techniques showed distinct strengths and weaknesses. The laser $^{40}Ar/^{39}Ar$ step-heating technique proved to be suitable for analysis of very small samples where the amount of material required for furnace-based techniques is not available, and it is therefore the method of choice for dating the very fine-grained hydrothermal minerals of which only small amounts of pure separates can be obtained. Roscoelite, for example, is intergrown with quartz containing excess ^{40}Ar, and therefore it is essential to analyze only the purest mineral separates that are free of quartz. However, the potential problem of Ar loss due to the fine grain size of these minerals, and the problem of small amounts of excess ^{40}Ar in roscoelite and biotite cannot be resolved even with the laser probe.

For the magmatic minerals, the furnace-based $^{40}Ar/^{39}Ar$ technique and, for biotite, the K-Ar method provided equally well or better constrained dates, because the greater amount of sample material used yielded more radiogenic Ar allowing for higher resolution of the gas release spectra, which facilitates interpretation of multi-component mixing trends and probably helps resolving the problem of excess ^{40}Ar in these samples better than laser step-heating technique.

Summary and conclusions

Laser $^{40}Ar/^{39}Ar$ age dating of magmatic biotite and hornblende (5.99 ± 0.11 Ma), representing the intrusive event, and of hydrothermal biotite (5.98 ± 0.13 Ma) and roscoelite (5.92 ± 0.08 Ma), representing the mineralizing event, show that the life-span of the magmatic and mineralizing system at the Porgera gold deposit, Papua New Guinea, was less than 0.26 m.y. The age differences between the intrusive and

mineralizing events, and between the individual stages of the of ore deposition, are too small to be resolved with currently available geochronological techniques.

References

Arribas A Jr, Hedenquist JW, Itaya T, Okada T, Concepción R A, Garcia JS Jr (1995) Contemporaneous formation of adjacent porphyry and epithermal Cu-Au deposits over 300 ka in northern Luzon, Philippines. Geology 23: 337-340

Cathles LM, Erendi AH, Barrie T (1997) How log can a hydrothermal system be sustained by a single intrusive event?. Econ Geol 92: 766-771

Davies HL (1983) Wabag 1:250,000 Geological Series Explanatory Notes, Sheet SB/54-8. Dept Minerals and Energy, Geol Survey Papua New Guinea, 84 pp

Davies HL (1990) Structure and Evolution of the Border Region of New Guinea. In: Carman GJ, Carman Z (eds) Petroleum Exploration in Papua New Guinea: Proceedings of the First PNG Petroleum Convention, Port Moresby, pp 245-269

Fleming AW, Handley GA, Williams KL, Hills AL, Corbett GJ (1986) The Porgera gold deposit, Papua New Guinea. Econ Geol 81: 660-680

Gaines RV, Skinner HC, Foord EE, Mason B, Rosenzweig A (1997) Dana's New Mineralogy: The System of Mineralogy of James Dwight Dana and Edward Salisbury Dana, 8th Edition, John Wiley & Sons, 1872 p

Gunson MJ, Haig DW, Kruman B, Mason RA, Perembo RCB, Stewart R (1997) Stratigraphic reconstruction of the Porgera region, Papua New Guinea. Australasian Institute of Mining and Metallurgy, Papua New Guinea Geology, Exploration, and Mining Conference, Madang, pp 99-108

Gunson MJ, Hall G, Johnston M (2000) Foraminiferal coloration index as a guide to hydrothermal gradients around the Porgera intrusive complex, Papua New Guinea. Econ Geol 95: 271-282

Handley GA, Bradshaw PMD (1986) The Porgera gold deposit, Papua New Guinea. In: Macdonald AJ (ed) Gold '86, Willodale, Ontario, 416-425

Handley GA, Henry DD (1990) Porgera gold deposit. In: Hughes FE (ed) Geology of the mineral deposits of Australia and Papua New Guinea: 1717-1724

Heinrich EW, Levinson AA (1955) Studies in the mica group: X-ray data on roscoelite and barium-muscovite, Am J Science 253: 39-43

Hilleband WF, Turner HW, Clarke FW (1899) On Roscoelite. Am J Science 42: 451-458

Hodges KW (1998) $^{40}Ar/^{39}Ar$ geochronology using the laser microprobe. In: McKibben MA, Shanks WC III, Ridley WI (eds) Applications of microanalytical techniques to understanding mineralizing processes. Reviews in Economic Geology 7: 53-72

Jaeger JC (1968) Cooling and solidification of igneous rocks. In: Hess HH, Poldervaart A (eds) The Poldervaart treatise on rocks of basaltic composition, vol 2: 503-536

Le Bas MJ, Le Maitre RW, Streckeisen A, Zanettin B (1986) A chemical classification of volcanic rocks based on the total alkali-silica diagram. J Petrol 27: 745-750

Ludwig KR (1991) ISOPLOT: A plotting and regression program for radiogenic isotope data. Version 2.53. USGS Open-File Report 91-445, 39 p

Marsh TM, Einaudi MT, McWilliams M (1997) $^{40}Ar/^{39}Ar$ geochronology of Cu-Au and Au-Ag mineralization in the Potrerillos District, Chile. Econ Geol 92: 784-806

McIntosh WC, Heizler MT (1994) Application of CO_2 laser heating in $^{40}Ar/^{39}Ar$ geochronology. USGS Circular 1107: 212

McDougall I, Harrison TM (1999) Geochronology and Thermochronology by the $^{40}Ar/^{39}Ar$ Method. Oxford University Press, 269 p

Pan Y, Fleet ME (1992) Mineral chemistry and geochemistry of vanadian silicates in the Hemlo gold deposit, Ontario, Canada, Contrib Mineral Petrol 109: 511-525

Renne PR, Deino AL, Walter RC, Turrin BD, Swisher CC, Becker TA, Cyrtis GH, Sharp WD, Jaouni AR (1994) Intercalibration of astronomical and radioisotopic time. Geology 22: 783-786

Richards JP (1990) Petrology and geochemistry of alkalic intrusives at the Porgera gold deposit, Papua New Guinea. J Geochem Exploration 35: 141-199

Richards JP, Kerrich R (1993) The Porgera gold mine, Papua New Guinea: Magmatic hydrothermal to epithermal evolution of an alkalic-type precious metal deposit. Econ Geol 88: 1017-1052

Richards JP, McCullock MT, Chappell BW, Kerrich R (1991) Source of metals in the Porgera gold deposit, Papua New Guinea: Evidence from alteration, isotopes, and noble metal geochemistry. Geochim Cosmochim Acta 55: 565-580

Richards JP, McDougall I (1990) Geochronology of the Porgera gold deposit, Papua New Guinea: Resolving the effects of excess argon on K-Ar and $^{40}Ar/^{39}Ar$ age estimates for magmatism and mineralization. Geochim Cosmochim Acta 54: 1397-1415

Roddick JC (1988) The assessment of errors in $^{40}Ar/^{39}Ar$ dating. In: Radiogenic age and isotope studies: Report 2. Geological Survey of Canada: Paper 88-2. pp 7-16

Roddick JC, Cliff RA, Rex DC (1980) The evolution of excess argon in alpine biotites-a $^{40}Ar/^{39}Ar$ analysis. Earth Planetary Science Letters 48: 185-208

Ronacher E, Richards JP, Johnston MD (1999) New mineralisation and alteration styles at the Porgera gold deposit, Papua New Guinea. In: Weber G (ed) Pacific Rim Congress Proceedings, Bali, Indonesia, pp 91-94

Ronacher E, Richards JP, Johnston MD (2000) Evidence for boiling during ore deposition at Porgera, Papua New Guinea. Geological Society of America Abstracts with Programs 32: A-280

Shinohara H, Hedenquist JW (1997) Constraints on magma degassing beneath the Far Southeast porphyry Cu-Au deposit, Philippines. J Petrology 38: 1741-1752

Steiger RH, Jäger E (1977) Subcommission on geochronology: Convention on the use of decay constants in geo- and cosmochronology. Earth Planetary Science Letters 36: 359-362

Villeneuve ME, MacIntyre D G (1997) Laser $^{40}Ar/^{39}Ar$ ages of the Babine porphyries and Newman Volcanics, Fulton Lake map area, west-central British Columbia. In: Radiogenic Age and Isotope Studies: Report 10; Geological Survey of Canada, Current Research 1997-F, 131-139

Wright FE (1914) The optical properties of roscoelite, Am J Science 38: 305-308

York D (1969) Least squares fitting of a straight line with correlated errors. Earth Planetary Science Letters 5: 320-324

Table 2-1: Apparent ages, MSWD values, and $^{40}Ar/^{36}Ar$ of the analyzed minerals.

Sample	Mineral	Age	MSWD	$^{40}Ar/^{36}Ar$
88-20	Biotite	5.99±0.11	3.7	295.5
88-20	Hornblende	6.35±0.23	1.0	311±9
88-15	Hornblende	6.3 ± 0.7	2.6	341±18
P98-8	Biotite	5.98±0.13	2.7	295.5
P41	Roscoelite	5.92±0.09	2.0	295.5
P43	Roscoelite	5.92 ±0.17	2.0	320±6

Table 2-2: Chemical compositions of magmatic biotite (sample 88-20) from the hawaiitic Peruk intrusion, and hydrothermal biotite from the alteration selvage of magnetite-sulfide-gold veins (sample P98-8), determined by electron microprobe. Atomic proportions (atom. prop.) calculated based on 22 oxygens.

	Biotite			
	88-20		P98-8	
	wt %	atom. prop.	wt %	atom. prop.
SiO_2	37.67	5.52	38.39	5.53
TiO_2	3.62	0.40	3.98	0.43
Al_2O_3	14.16	2.42	14.65	2.49
Cr_2O_3	0.02	0.00	0.03	0.00
FeO	15.80	1.94	13.19	1.59
MnO	0.27	0.03	0.11	0.01
MgO	16.12	3.52	17.30	3.72
CaO	0.02	0.00	0.08	0.01
Na_2O	0.79	0.22	0.43	0.12
K_2O	9.26	1.73	9.48	1.74
V_2O_3	0.00	0.00	0.00	0.00
F	0.04	0.02	0.05	0.02
Cl	0.05	0.01	0.17	0.04
Totals	97.82	15.82	97.86	15.70

Table 2-3: Chemical compositions of roscoelite P41 and P43 (determined by electron microprobe) in comparison with Hillebrand's (1899) analysis of roscoelite from its type locality in the Stockslager mine, California. Atomic proportions (atom. prop.) calculated based on 22 oxygens.

	P41		P43		Hillebrand, 1899
	wt %	atom. prop.	wt %	atom. prop.	wt %
SiO_2	45.86	6.74	45.60	6.71	45.17
TiO_2	0.08	0.01	0.08	0.01	0.78
Al_2O_3	7.69	1.33	8.37	1.45	11.45
Cr_2O_3	0.44	0.05	0.40	0.05	n.a.
FeO	0.16	0.02	0.29	0.04	1.60
MnO	0.01	0.00	0.02	0.00	n.a.
MgO	0.91	0.20	1.09	0.24	1.64
CaO	0.02	0.00	0.02	0.00	n.a.
Na_2O	0.01	0.00	0.05	0.02	0.06
K_2O	9.53	1.79	9.81	1.84	10.37
V_2O_3	30.02	3.54	28.88	3.41	24.01
F	0.00	0.00	0.00	0.00	0.00
Cl	0.00	0.00	0.00	0.00	n.a.
Totals	94.73	13.69	94.61	13.77	95.08

Table 4: Analytical details of the $^{40}Ar/^{39}Ar$ analyses

Power[a]	Volume ^{39}Ar $x10^{-11}$ cc	$^{36}Ar/^{39}Ar$	$^{37}Ar/^{39}Ar$	$^{38}Ar/^{39}Ar$	$^{40}Ar/^{39}Ar$	$\%^{40}Ar$ Atm[d]	$*^{40}Ar/^{39}Ar$	f_{39}[b] (%)	Apparent Age Ma[c]
88-20 Hornblende; J=.00047050									
				Aliquot: A					
3.9	0.0691	0.6129±0.0582	10.223±137.399	0.023±0.043	197.689±18.641	91.6	16.565±25.042	1.2	14.01±21.09
5.0	0.5235	0.0400±0.0027	5.886±31.471	0.029±0.003	20.311±0.598	58.2	8.483±0.841	8.9	7.19±0.71
12.0	0.7211	0.0265±0.0016	6.939±17.338	0.028±0.002	15.377±0.339	51.0	7.542±0.417	12.3	6.39±0.35
				Aliquot: B					
3.9	0.1296	0.4668±0.0227	7.740±63.527	0.041±0.009	152.305±6.341	90.6	14.371±8.975	2.2	12.16±7.57
5.0	0.7680	0.0283±0.0019	6.135±25.918	0.028±0.003	16.497±0.398	50.6	8.144±0.569	13.1	6.90±0.48
12.0	1.0178	0.0164±0.0016	7.143±26.084	0.026±0.002	12.437±0.303	38.9	7.593±0.491	17.3	6.43±0.42
				Aliquot: C					
3.9	0.1053	0.8307±0.0297	10.777±30.919	0.024±0.014	262.811±5.380	93.4	17.346±9.956	1.8	14.66±8.38
5.0	0.8414	0.0442±0.0016	6.431±20.424	0.028±0.002	21.510±0.401	60.7	8.447±0.514	14.3	7.16±0.44
12.0	1.7109	0.0182±0.0007	7.082±17.012	0.028±0.001	13.208±0.215	40.7	7.832±0.248	29.1	6.64±0.21
88-20 Biotite; J=.00048180									
				Aliquot: A					
2.4	0.0440	0.1397±0.0250	1.321±144.695	0.074±0.024	46.166±6.593	89.4	4.892±7.549	0.4	4.25±6.55
3.4	0.6161	0.0282±0.0014	0.098±51.626	0.011±0.003	15.007±0.416	55.6	6.669±0.383	5.0	5.79±0.33
4.4	1.0130	0.0102±0.0009	0.037±38.333	0.017±0.000	9.766±0.216	30.9	6.747±0.187	8.2	5.86±0.16
5.5	1.3828	0.0078±0.0006	0.033±40.464	0.015±0.001	9.058±0.160	25.3	6.767±0.126	11.2	5.87±0.11
12.0	0.5119	0.0095±0.0021	0.103±117.964	0.015±0.002	9.570±0.427	29.2	6.773±0.500	4.1	5.88±0.43
				Aliquot: B					
2.8	0.3011	0.0844±0.0029	1.042±29.650	0.029±0.003	32.719±0.742	76.3	7.769±0.657	2.4	6.74±0.57
3.4	1.5723	0.0129±0.0008	0.096±71.311	0.015±0.001	10.957±0.156	34.7	7.159±0.205	12.7	6.21±0.18
4.4	2.4639	0.0056±0.0003	0.136±40.349	0.013±0.000	8.600±0.097	19.3	6.938±0.079	19.9	6.02±0.07
5.5*	3.0209	0.0029±0.0005	0.073±31.111	0.014±0.000	8.511±0.076	9.9	7.666±0.147	24.4	6.65±0.13
12.0*	1.4441	0.0045±0.0007	0.028±71.130	0.016±0.001	8.598±0.169	15.3	7.279±0.171	11.7	6.32±0.15
				Aliquot: C					
88-15 Hornblende; J=.00046770									
				Aliquot: A					
2.8*	0.0138	1.8491±0.3116	8.627±241.872	0.016±0.092	577.241±94.371	94.7	30.829±130.313	0.2	25.83±108.39
3.9*	0.0545	0.4008±0.0352	3.241±86.384	0.060±0.020	134.613±8.051	88.0	16.170±12.089	0.9	13.59±10.12
4.5	0.1924	0.0906±0.0053	5.906±53.314	0.023±0.007	38.016±1.753	70.5	11.231±1.834	3.2	9.45±1.54
5.0*	0.5316	0.0192±0.0019	5.840±19.019	0.030±0.003	15.183±0.533	37.4	9.504±0.575	8.9	8.00±0.48
5.5*	0.1199	0.0770±0.0089	5.532±68.364	0.037±0.010	29.463±2.160	77.2	6.713±2.472	2.0	5.66±2.08
12.0*	0.1992	0.0949±0.0058	6.281±24.345	0.008±0.011	34.164±1.090	82.1	6.128±1.467	3.4	5.16±1.23
				Aliquot: B					
3.9*	0.2014	0.4734±0.0194	7.104±48.955	0.027±0.010	153.996±4.994	90.8	14.102±7.474	3.4	11.86±6.27
5.0	1.4976	0.0283±0.0008	5.802±12.986	0.025±0.002	17.470±0.410	47.9	9.097±0.438	25.2	7.66±0.37
12.0	1.1866	0.0228±0.0019	6.142±19.260	0.028±0.002	14.694±0.376	45.9	7.950±0.624	19.9	6.70±0.53
				Aliquot: C					
3.9*	0.1109	0.5252±0.0375	8.089±88.512	0.018±0.018	175.293±10.534	88.5	20.108±15.087	1.9	16.89±12.61
5.0	0.5904	0.0503±0.0034	6.049±33.347	0.026±0.004	24.161±0.681	61.6	9.289±1.126	9.9	7.82±0.95
12.0	1.2544	0.0177±0.0008	6.323±21.017	0.028±0.002	13.452±0.298	38.9	8.226±0.302	21.1	6.93±0.25
P98-8 Biotite; J=.00199730									
				Aliquot: A					
2.0*	0.0454	0.0553±0.0149	0.513±122.113	0.234±0.025	63.062±6.924	25.9	46.726±5.376	0.2	160.97±17.72
2.3	0.0718	0.1073±0.0137	0.327±108.982	0.235±0.019	32.700±3.446	97.0	0.988±3.569	0.3	3.56±12.84
2.7	0.1370	0.0653±0.0052	0.102±204.165	0.213±0.005	20.526±1.473	94.0	1.229±0.523	0.5	4.42±1.88
3.4	1.1158	0.1244±0.0029	0.055±76.134	0.195±0.006	38.828±0.831	94.7	2.056±1.172	4.4	7.39±4.21
4.0	1.5211	0.0661±0.0017	0.028±72.906	0.192±0.003	21.731±0.221	89.9	2.193±0.506	6.0	7.88±1.81
4.8	2.9677	0.0537±0.0011	0.015±33.744	0.187±0.003	17.514±0.168	90.6	1.652±0.365	11.6	5.94±1.31
5.5	1.6497	0.1310±0.0017	0.008±238.577	0.186±0.004	41.210±0.296	93.9	2.495±0.569	6.5	8.97±2.04
7.0	0.4971	0.1885±0.0066	0.024±99.961	0.164±0.009	59.078±1.093	94.3	3.377±2.169	2.0	12.13±7.76
12.0	0.1686	1.1571±0.0208	0.114±110.446	0.240±0.024	344.033±4.482	99.4	2.111±7.432	0.7	7.59±26.67
				Aliquot: B					
2.7*	0.3976	0.0818±0.0025	0.323±67.621	0.157±0.005	27.604±0.685	87.5	3.441±0.701	1.6	12.36±2.51
3.4*	1.5868	0.0297±0.0006	0.073±79.036	0.168±0.003	11.024±0.187	79.6	2.246±0.192	6.2	8.07±0.69
4.0	1.6326	0.0097±0.0005	0.042±31.022	0.177±0.003	4.599±0.129	62.2	1.738±0.110	6.4	6.25±0.40
5.0	7.4077	0.0031±0.0002	0.019±38.451	0.166±0.002	2.493±0.029	36.3	1.589±0.056	29.0	5.72±0.20

6.0	3.2880	0.0025±0.0004	0.011±50.380	0.161±0.002	2.392±0.065	31.2	1.646±0.091	12.9	5.92±0.33
12.0	3.0188	0.0019±0.0002	0.016±45.170	0.196±0.003	2.221±0.073	24.6	1.674±0.033	11.8	6.02±0.12

P41 Roscoelite; J=.00199480

Aliquot: A

2.0*	0.1823	0.2051±0.0059	0.061±124.592	0.034±0.004	69.133±1.246	87.7	8.524±1.490	0.3	30.42±5.27
2.3*	0.8129	0.0347±0.0018	0.013±186.778	0.012±0.002	14.164±0.309	72.3	3.920±0.516	1.5	14.05±1.84
3.0	5.1632	0.0030±0.0002	0.005±98.864	0.003±0.000	2.577±0.042	34.3	1.693±0.047	9.6	6.08±0.17
3.7	3.2904	0.0028±0.0004	0.005±272.824	0.003±0.000	2.531±0.063	32.8	1.700±0.102	6.1	6.11±0.37
4.3	2.0689	0.0097±0.0004	0.011±51.268	0.005±0.000	4.549±0.100	63.2	1.672±0.063	3.9	6.01±0.23
5.5*	0.9053	0.3190±0.0076	0.017±53.221	0.011±0.003	96.275±0.986	97.9	2.019±2.444	1.7	7.25±8.76
6.2*	0.6254	0.6163±0.0127	0.023±41.145	0.009±0.004	186.750±3.785	97.5	4.646±5.309	1.2	16.64±18.93
7.0*	0.1397	1.7772±0.0382	0.104±67.404	0.071±0.012	545.101±8.753	96.3	19.925±14.156	0.3	70.32±49.00
7.8*	0.0960	1.1266±0.0262	0.127±48.578	0.132±0.009	371.679±5.874	89.6	38.757±9.279	0.2	134.35±31.00
12.0*	0.1543	0.3005±0.0070	0.092±83.418	0.159±0.006	153.895±2.008	57.7	65.085±2.237	0.3	220.22±7.13

Aliquot: B

2.0*	0.3166	0.2681±0.0064	0.040±129.740	0.030±0.004	79.435±1.559	99.7	0.199±2.284	0.6	0.72±8.22
2.3*	0.3279	0.0648±0.0034	0.028±385.281	0.019±0.007	23.026±0.750	83.2	3.869±0.897	0.6	13.87±3.20
3.0	3.9676	0.0030±0.0002	0.006±69.412	0.004±0.001	2.521±0.053	34.7	1.646±0.035	7.4	5.91±0.13
3.7	6.6121	0.0012±0.0002	0.006±75.303	0.003±0.001	1.999±0.032	17.8	1.643±0.046	12.3	5.90±0.17
4.3	5.0379	0.0017±0.0001	0.006±134.829	0.003±0.000	2.135±0.043	23.9	1.625±0.026	9.4	5.84±0.09
5.0	0.6122	0.0150±0.0017	0.024±122.990	0.007±0.002	6.111±0.352	72.3	1.693±0.416	1.1	6.08±1.49
5.5	0.2682	0.0297±0.0028	0.053±56.893	0.024±0.008	10.722±0.768	81.9	1.944±0.379	0.5	6.98±1.36
6.2	0.6245	0.0201±0.0013	0.024±94.307	0.010±0.004	7.870±0.346	75.6	1.919±0.257	1.2	6.89±0.92
7.0*	0.2463	0.2492±0.0063	0.041±201.138	0.030±0.002	81.668±1.834	90.2	8.019±2.339	0.5	28.63±8.28
12.0*	0.5324	0.1911±0.0064	0.042±94.664	0.042±0.003	69.266±1.456	81.5	12.790±2.339	1.0	45.45±8.21

Aliquot: C

2.3*	2.5635	0.0594±0.0013	0.009±52.126	0.006±0.001	20.394±0.157	86.1	2.838±0.400	4.8	10.18±1.43
3.0	11.2397	0.0015±0.0002	0.005±24.657	0.002±0.000	2.136±0.020	20.6	1.697±0.044	20.9	6.10±0.16
3.7	4.4441	0.0019±0.0002	0.008±38.895	0.002±0.000	2.198±0.048	25.2	1.643±0.051	8.3	5.90±0.18
4.3	1.7021	0.0096±0.0004	0.017±56.655	0.004±0.001	4.409±0.128	64.1	1.585±0.077	3.2	5.69±0.28
12.0*	1.8622	0.0762±0.0020	0.021±54.346	0.015±0.002	29.203±0.308	77.2	6.651±0.661	3.5	23.78±2.35

P43 Roscoelite; J=.00196890

Aliquot: A

2.0*	0.1402	0.1415±0.0070	0.059±270.436	0.066±0.009	43.346±1.544	96.4	1.542±1.616	0.3	5.47±5.72
2.3*	0.2371	0.0555±0.0045	0.034±321.108	0.048±0.004	18.050±0.937	90.9	1.644±1.111	0.6	5.83±3.93
2.7*	1.1454	0.0113±0.0009	0.013±146.462	0.017±0.001	5.972±0.179	56.1	2.619±0.195	2.7	9.28±0.69
3.0	3.2314	0.0020±0.0003	0.006±50.350	0.004±0.000	2.282±0.067	26.4	1.680±0.057	7.7	5.96±0.20
3.7	3.9045	0.0014±0.0003	0.006±71.780	0.003±0.000	2.082±0.055	19.2	1.682±0.062	9.3	5.97±0.22
4.3	1.2498	0.0043±0.0008	0.011±55.086	0.009±0.001	2.999±0.163	42.8	1.714±0.196	3.0	6.08±0.69
5.0*	0.3473	0.0166±0.0025	0.034±55.028	0.017±0.002	7.842±0.585	62.5	2.939±0.465	0.8	10.41±1.64
6.2*	0.1870	0.0453±0.0042	0.061±181.870	0.041±0.004	17.076±1.156	78.4	3.688±0.794	0.4	13.05±2.80
12.0*	0.1919	0.0461±0.0041	0.042±441.704	0.091±0.004	44.469±1.170	30.7	30.835±0.832	0.5	106.33±2.79

Aliquot: B

2.0*	0.5339	0.1702±0.0047	0.023±147.706	0.024±0.003	51.995±1.196	96.7	1.705±1.766	1.3	6.04±6.25
2.3*	0.7845	0.0368±0.0014	0.018±57.721	0.013±0.002	12.447±0.328	87.3	1.586±0.378	1.9	5.62±1.34
2.7	2.7610	0.0045±0.0003	0.008±162.712	0.004±0.000	3.086±0.076	43.3	1.749±0.056	6.6	6.20±0.20
3.0	2.8886	0.0026±0.0003	0.008±53.783	0.003±0.000	2.446±0.071	30.9	1.692±0.073	6.9	6.00±0.26
3.7	3.5891	0.0018±0.0003	0.007±51.534	0.003±0.000	2.234±0.058	24.1	1.696±0.059	8.5	6.01±0.21
4.3	2.1744	0.0036±0.0003	0.009±63.196	0.004±0.001	2.798±0.097	37.5	1.749±0.056	5.2	6.20±0.20
5.5*	0.7362	0.0381±0.0016	0.021±106.147	0.011±0.001	13.036±0.297	86.4	1.769±0.410	1.8	6.27±1.45
12.0*	0.6303	0.2125±0.0054	0.026±139.803	0.028±0.002	69.798±1.080	90.0	7.014±1.885	1.5	24.74±6.61

Aliquot: C

2.7	5.7040	0.0091±0.0002	0.007±46.295	0.006±0.000	4.589±0.039	58.7	1.897±0.034	13.6	6.73±0.12
3.7	6.7231	0.0019±0.0002	0.007±82.229	0.003±0.000	2.349±0.031	24.3	1.779±0.035	16.0	6.31±0.12
12.0*	4.9174	0.0269±0.0004	0.008±52.570	0.010±0.001	11.914±0.079	66.8	3.961±0.137	11.7	14.02±0.48

a: As measured by laser in % of full nominal power (10W)

b: Fraction ^{39}Ar as percent of total run

c: Errors are analytical only and do not reflect error in irradiation parameter J

d: Atm = atmospheric

*: Step not included in age determination

All uncertainties quoted at 2σ level

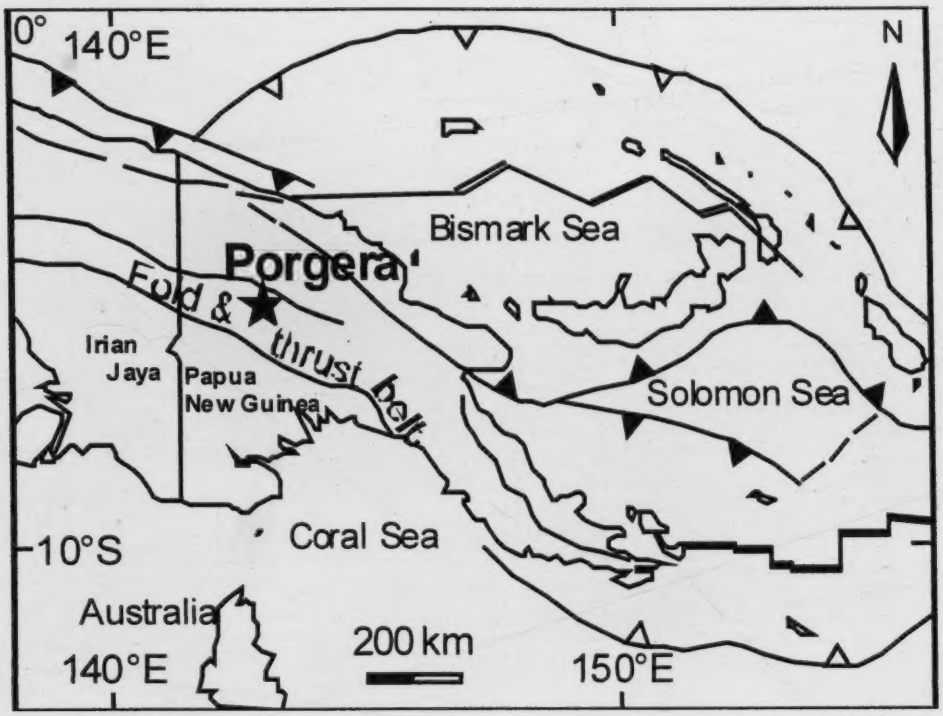

Figure 2-1: Location of the Porgera gold mine in the fold and thrust belt of central Papua New Guinea. This Pliocene belt marks the edge of the Australasian continental plate. Modified from Richards and Kerrich (1993)

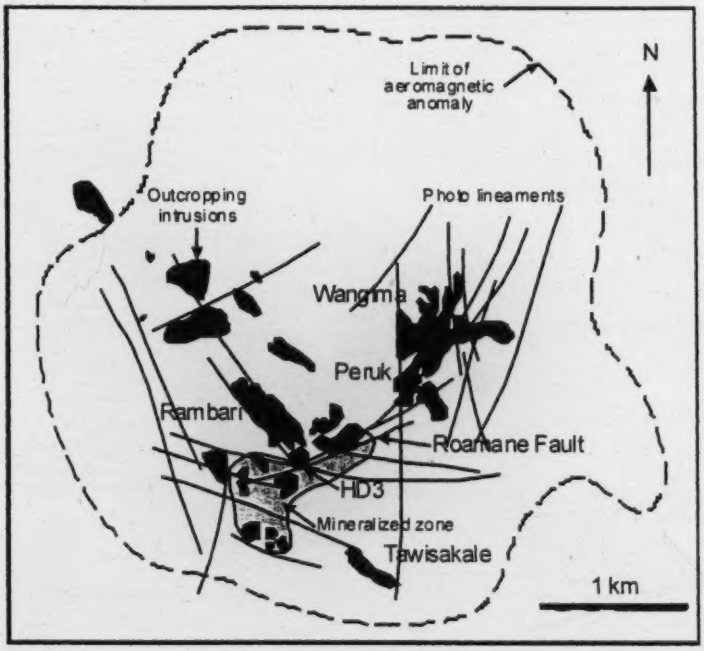

Figure 2-2: Schematic map showing surface expression of individual intrusions from the Porgera Intrusive Complex (PIC), which are interpreted to be apophyses of a larger pluton at depth indicated by an aeromagnetic anomaly shown as dashed line. Also shown is the Roamane Fault, a late normal fault that hosted the highest grade ore zones. Modified from Richards (1990)

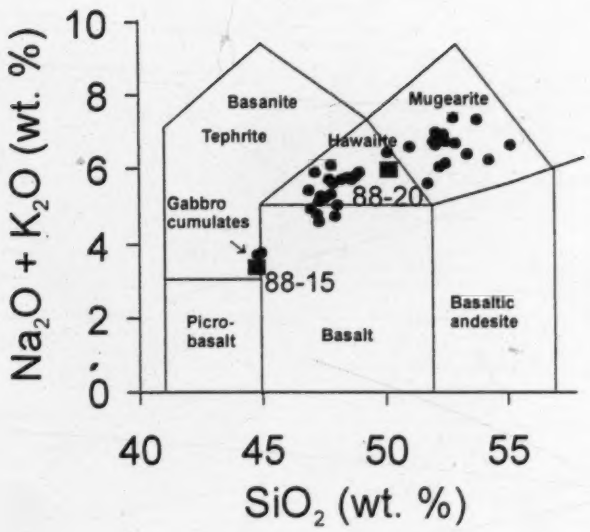

Figure 2-3: Total alkali-silica diagram showing the positions of hawaiite (i.e., sodic trachybasalt) and mugearite (i.e., sodic basaltic trachyandesite). The dots represent compositions of samples analyzed by Richards (1990), and the squares represent compositions of the samples dated in this study. The Porgera alkali basalts are cumulate phases. The samples plotted on the diagram were recalculated to 100% on an H_2O- and CO_2-free basis.

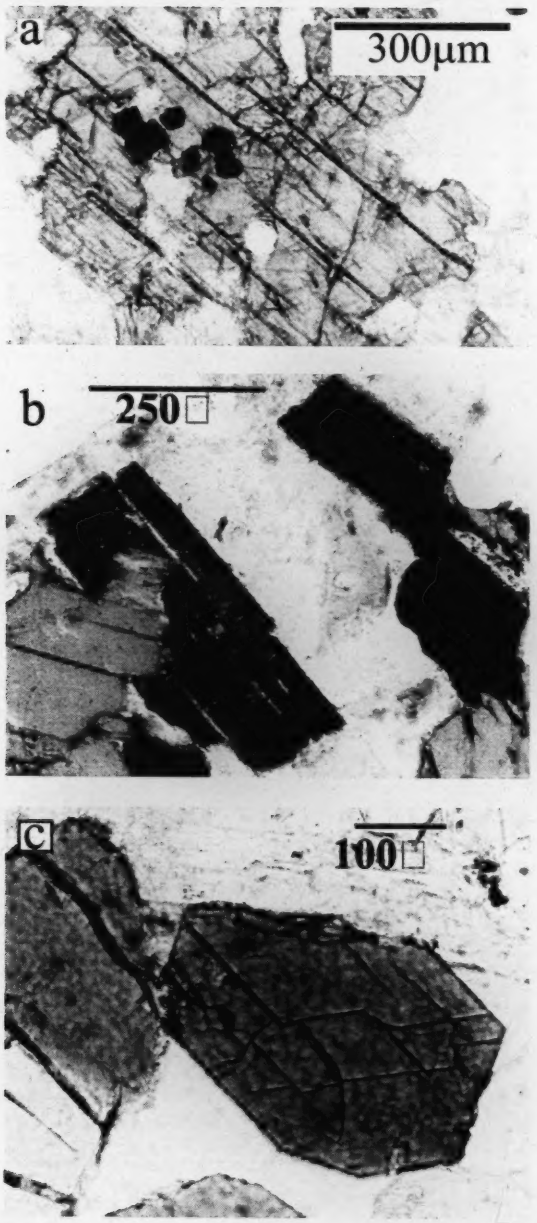

Figure 2-4: Photomicrograph of the magmatic minerals dated for this study taken in plane polarized light. (a) Hornblende from sample 88-15 from the Rambari alkali gabbro intrusion; (b) biotite and (c) hornblende from sample 88-20 from the hawaiitic Peruk intrusion.

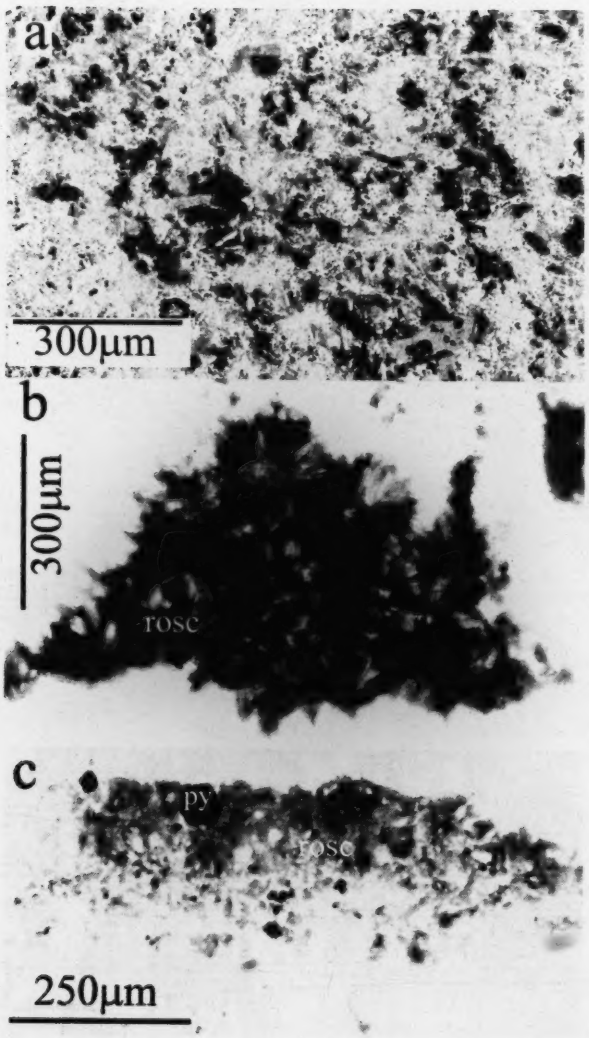

Figure 2-5: Photomicrographs of the hydrothermal minerals analyzed taken in plane polarized light. (a) Finely dispersed biotite from alteration selvages associated with magnetite-sulfide-gold veins; (b) roscoelite (rosc) rosettes from sample P41; and (c) fine-grained roscoelite (rosc) intergrown with pyrite (py) and quartz overlain by a band of coarse-grained comb quartz from sample P43

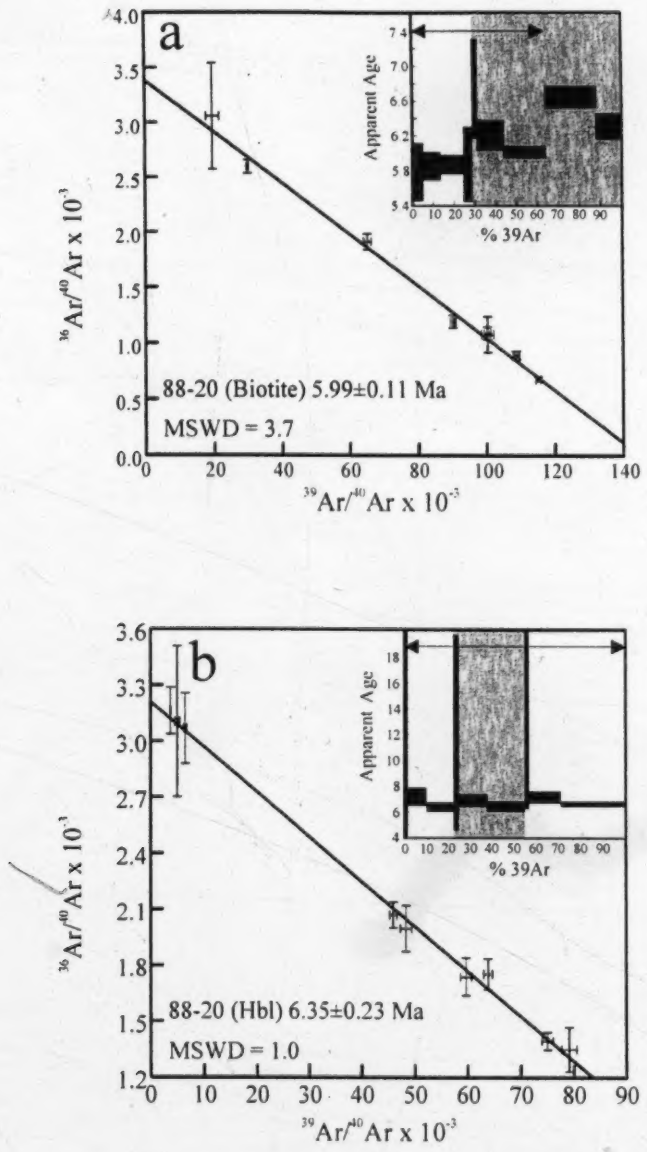

Figure 2-6: Inverse isochron plots and gas-release diagrams of sample 88-20. (a) biotite and (b) hornblende (hbl). The different shadings in the gas-release plots represent individual aliquots of the sample. All aliquots were combined to 100%. The arrows indicate which steps were plotted on the inverse isochron diagrams and used to calculate an age

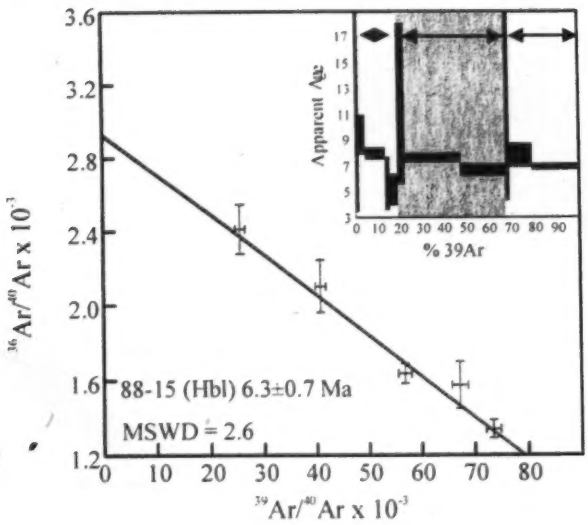

Figure 2-7: Inverse isochron and gas-release plot of hornblende (hbl) 88-15 from the Rambari alkali gabbro. The different shadings in the gas-release plot represent individual aliquots of the sample. All aliquots were combined to 100%. The arrows indicate which steps were plotted on the inverse isochron diagram and used to calculate an age

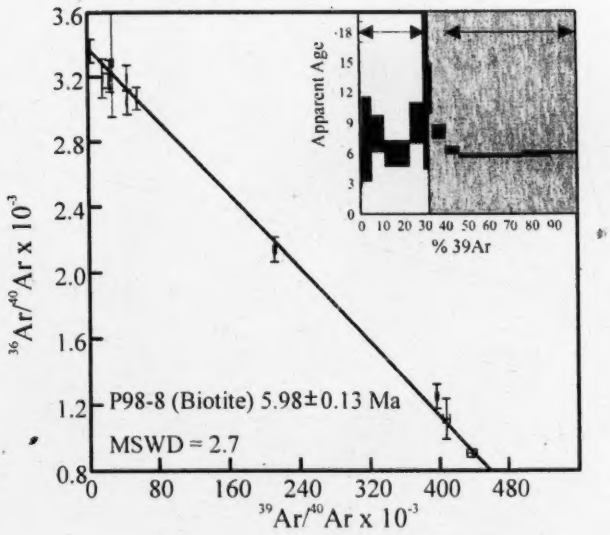

Figure 2-8: Inverse isochron and gas-release plot of biotite P98-8 from the alteration selvage of early magnetite-sulfide±gold veins. The different shadings in the gas-release plot represent individual aliquots of the sample. All aliquots were combined to 100%. The arrows indicate which steps were plotted on the inverse isochron diagram and used to calculate an age

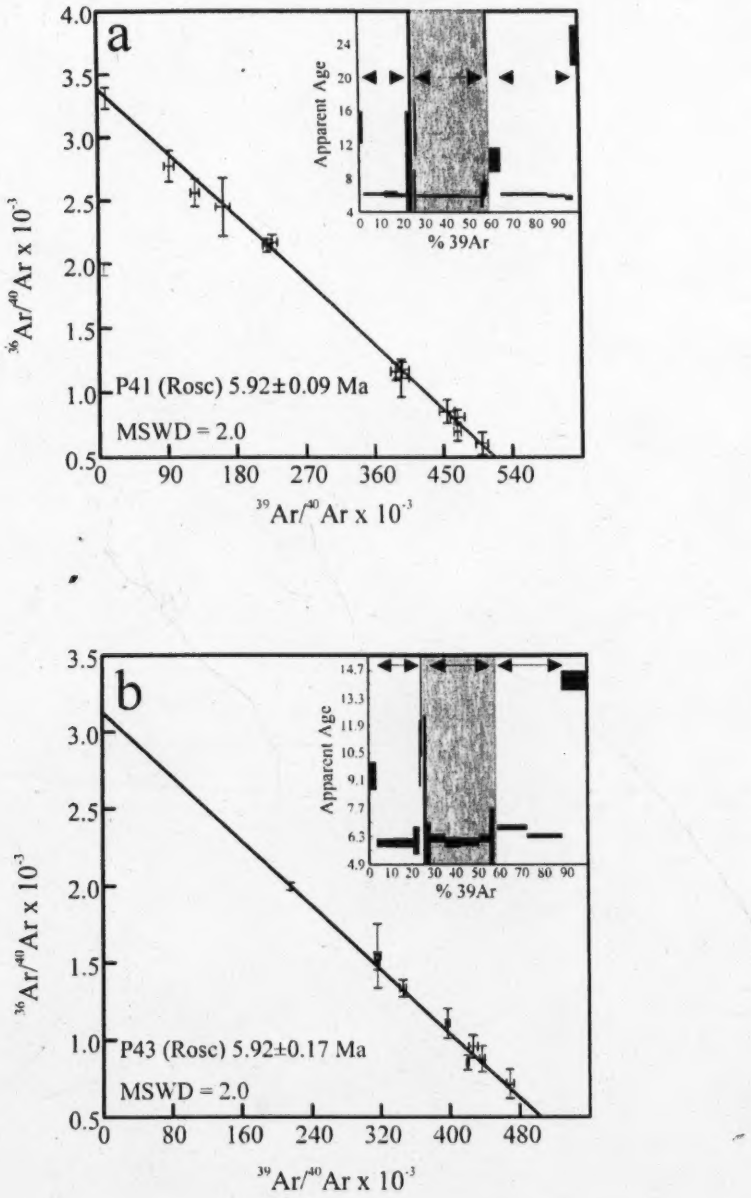

Figure 2-9: Inverse isochron and gas-release plots of roscoelite (rosc) P41 (a) and P43 (b). The different shadings in the gas-release plots represent individual aliquots of the sample. All aliquots were combined to 100%. The arrows indicate which steps were plotted on the inverse isochron diagrams and used to calculate an age

Chapter 3

Evidence for fluid phase separation in high-grade ore zones at the Porgera gold deposit, Papua New Guinea

A version of this paper was published in Mineralium Deposita, 2000, v. 35, p. 683-688.
The co-authors are J.P. Richards, Dept. of Earth and Atmospheric Sciences, University of Alberta, Edmonton, Alberta T6G 2E3, Canada, and M.D. Johnston, Porgera Joint Venture, P.O. Box 484, Mt. Hagen, Papua New Guinea

Introduction

The Porgera gold deposit is located in a Pliocene fold- and thrust-belt that forms the highlands of Papua New Guinea (Fig. 3-1). With 10.8 million mined ounces of gold and an 11 million ounce reserve, Porgera is one of the largest gold producers in the South Pacific region.

The deposit is spatially, temporally, and genetically associated with a 6.0 ± 0.3 Ma-old mafic, alkalic intrusive complex emplaced at shallow crustal levels in Cretaceous calcareous mudstones and carbonaceous siltstones (Davies 1983; Richards 1990; Richards and McDougall 1990; Richards and Kerrich 1993). Gold was introduced in two stages (Fleming et al. 1986; Handley and Bradshaw 1986; Richards and Kerrich 1993). Stage I is characterized by zones of sericite-carbonate alteration with disseminated auriferous pyrite, and sulfide-carbonate±quartz veins with pyrite, iron-rich sphalerite, galena, and minor native gold (Au°). Previous studies of fluid inclusions in sphalerite and rare early quartz from these veins yielded average homogenization temperatures (Th) of 299° ± 33°C (n = 274) and salinities of 9.5 ± 1.8 (n = 142) weight percent NaCl equivalent (wt % NaCl equiv) with minor amounts of CO_2 (up to 3.1 mole %; Richards et al. 1997). Stage II mineralization consists of quartz-roscoelite veins and hydrothermal breccias with locally abundant Au° or Au-Ag-tellurides. The highest-grade ore zones (≥1000 g/t Au°) are structurally controlled by the Roamane fault zone (Fig. 3-2), a late normal fault that post-dates all known intrusions. Liquid-rich aqueous fluid inclusions in stage II quartz veins are

characterized by an average Th of 146° ± 13°C (n = 519), but salinities define a bimodal population with average values of 4.2 ± 0.3 (n = 104) and 7.8 ± 0.7 (n = 346) wt % NaCl equiv. Fluid inclusions found in quartz directly associated with early precipitation of roscoelite and gold near the vein margins belong dominantly to the higher salinity group, whereas both types of inclusions are abundant in late vuggy quartz (Richards and Kerrich 1993).

Handley and Bradshaw (1986) speculated, on the basis of comparison with other epithermal systems, that the highest-grade stage II ore zone (Zone VII, Fig. 3-2) was generated by fluid boiling. Richards (1992) and Richards and Kerrich (1993) also suggested phase separation as a possible precipitation mechanism for gold based on textural observations (e.g., matrix-supported hydrothermal breccias with clasts rimmed by fine-grained silica), and Richards et al. (1997) presented a CO_2-exsolution model based on fluid inclusion gas-chromatographic data. However, unequivocal visual evidence of phase separation was not found in the fluid inclusion record in these earlier studies. Here we report new observations of coexisting primary liquid-rich and vapor-rich (CO_2-bearing) fluid inclusions in stage II quartz from high-grade zones of the Porgera gold deposit, which provide direct evidence for phase separation during vein formation.

Samples

Five samples of stage II quartz-roscoelite-Au° veins and breccias were selected for study from high-grade ore zones, one of which was from the highest grade area of the mine (Zone VII; sample P98-2204). Sample locations are plotted on Figure 3-2 where it can be seen that the samples were taken from various depths over a range of more than 250m. Four vein samples were taken from drill core, and one breccia sample (P98-2204) was collected from an abandoned stope in the underground workings.

Vein textures

Stage II quartz-roscoelite-Au° veins range from a few millimeters to several centimeters in width. Typically, the vein edge is rimmed by a band of very fine-grained

quartz where workable fluid inclusions are not present; qualitative electron microprobe analyses show that minor amounts of Ca-Fe-Mg carbonate, barite, anhydrite, and pyrite are intergrown with this quartz. These layers are succeeded by bands of fine-grained roscoelite-quartz-pyrite±Au°/Au-Ag-telluride, followed in turn by coarse-grained, barren comb quartz (Fig. 3-3). Repetition of this sequence is common, giving the veins a banded appearance. Vein centers are vuggy, sometimes with a late filling of Ca-Fe-Mg carbonate or gypsum. Quartz-roscoelite-Au° veins locally grade into hydrothermal breccias in which the highest grades of gold are found. The breccias are matrix-supported, with the matrix showing a similar paragenesis to the veins described above.

Analytical Techniques

Fluid inclusion microthermometry was conducted on a Linkam THMSG 600 heating-freezing stage, calibrated with synthetic fluid inclusions produced by Syn Flinc®. Measurements below 31.1°C (the critical point of CO_2) are accurate to within ±0.1°C, and measurements above this temperature to within ±1°C.

Calculation of salinity from ice melting points assumes the applicability of the NaCl-H_2O system as modeled by Bodnar (1993). The presence of clathrate in many inclusions indicated by sudden bubble movement upon heating to 10°C suggests that such calculations may overestimate true salinity (Hedenquist and Henley 1985; Collins 1979). However, no liquid-rich aqueous fluid inclusions contained liquid CO_2, so clathrate melting points could not be used to calculate fluid salinities. Richards and Kerrich (1993) calculated a maximum error of +3 wt % NaCl equiv for fluid inclusions in which clathration was significant.

Fluid inclusions

Primary fluid inclusions were studied from bands of clear quartz immediately adjacent to or between roscoelite-Au°-rich bands (intergrown on a scale of tens to hundreds of micrometers) because of the lack of preservation of fluid inclusions in the very fine-grained auriferous vein margins. Thus, although these inclusions are not

strictly coeval with periods of gold deposition, their entrapment immediately followed, or was bracketed by, these events.

The observed fluid inclusions are small (5-10μm) and commonly irregularly shaped. Typically, they are two phase liquid-rich inclusions with a small vapor bubble. However, rare vapor-rich primary fluid inclusions are also observed coexisting with liquid-rich inclusions in these samples (Fig. 3-4). Groups of coexisting vapor- and liquid-rich inclusions are termed boiling assemblages throughout the rest of this paper, although as is discussed below, this process actually involved separation of a CO_2-rich vapor rather than steam. It was not possible to measure $Th_{(V)}$ for the vapor-rich inclusions because typically they are completely dark and no changes were visible upon heating. The $Th_{(L)}$ and salinity values for liquid-rich inclusions from boiling assemblages and from groups of liquid-rich-only inclusions are presented in Figures 3-5 and 3-6, and summarized in Table 3-1. The $Th_{(L)}$ values are statistically indistinguishable for inclusions from boiling assemblages ($Th_{(L)}$ = 154 ± 16°C, n = 80, excluding one group of seven inclusions with Th > 220°C) and for groups of liquid-rich-only inclusions (Th = 146 ± 14°C, n = 184). However, occasional $Th_{(L)}$ values as high as 280°C were measured for some inclusions from boiling assemblages (average $Th_{(L)}$ = 262 ± 18°C, n = 7; Figure 3-5a). Ice melting points of inclusions in liquid-rich-only groups are bimodally distributed with average values of –2.8° ± 0.3°C (equivalent to 4.7 ± 0.5 wt % NaCl, n = 47) and –5.0° ± 0.5°C (7.8 ± 0.7 wt % NaCl equiv, n = 137), similar to the distribution observed by Richards and Kerrich (1993). In contrast, liquid-rich inclusions from boiling assemblages fall dominantly in the high-salinity group and exhibit an average salinity of 7.8 ± 0.8 wt % NaCl equiv (n = 86).

Microthermometric measurements of the vapor-rich fluid inclusions were generally impossible to make because of their dark appearance. Rarely, however, small granules of solid were visible in these inclusions after freezing, which melted near -56.6°C indicating the presence of CO_2. A few groups of higher-density three-phase inclusions were found in which liquid CO_2 was present at room temperature. Most of these inclusions also contain significant amounts of water, and are interpreted to have been heterogeneously trapped during phase separation. The carbonic phase in these

inclusions melted between –56.6° and –57.1°C indicating the dominance of CO_2, although small amounts of CH_4 may be present as suggested by gas-chromatographic analyses (Richards et al. 1997). Isochores for two CO_2-rich vapor inclusions where Th_{CO2} could be measured (near-critical homogenization at 31.0°C) were estimated using the program MacFlinCor (Brown and Hagemann 1994). Liquid-rich inclusions coexisting with these vapor-rich inclusions homogenized between 157° and 161°C (n = 10), and 160°C is therefore interpreted to represent the trapping temperature (Tt). Intersections of the CO_2 isochores with the 160°C isotherm indicate pressures of between 250 and 340 bars at the time of trapping (Fig. 3-7). This range of pressure reflects uncertainty in the calculation of isochores for critical compositions rather than real pressure variations, although such variations are likely. Moreover, given that many vapor-rich inclusions contained no visible liquid CO_2 and were therefore of lower density, these pressures likely indicate maximum values.

Discussion

Fluid inclusion assemblages indicating phase separation have been observed at various levels of the Porgera mine over a depth range of more than 250m. Boiling assemblages are preserved in bands of clear quartz adjacent to or between roscoelite-quartz-pyrite-Au° bands. Few workable fluid inclusions are hosted by the roscoelitic bands due to their very fine-grained nature, but the close spatial relationship between quartz containing boiling assemblages and gold-rich roscoelitic layers suggests that boiling may have been an important mechanism in gold deposition by destabilizing Au-bisulfide complexes through loss of H_2S to the vapor phase. Furthermore, the fine-grained, fluid inclusion-poor nature of silica in the roscoelitic bands is an expected consequence of rapid precipitation from oversaturated fluids during phase separation (Fournier 1985), as argued by Richards and Kerrich (1993).

Additional indirect evidence for the occurrence of phase separation is provided by the occurrence of sulfate and carbonate minerals in the fine-grained siliceous vein margins, and the negative $\delta^{34}S$ values of stage II sulfides (Richards and Kerrich 1993). These observations are consistent with fluid oxidation and pH increase, both of which

can be attributed to phase separation (Drummond and Ohmoto 1985; Spycher and Reed 1989).

Phase separation was most likely initiated by sudden depressurization (flashing) of the ore-forming fluids along active normal faults. The sudden and intermittent nature of flashing and the fine grain size of the resulting precipitates, may be the reason why boiling assemblages are rarely preserved in the fluid inclusion record.

Liquid-phase fluid inclusions from stage II veins have broadly uniform homogenization temperatures, but define a bimodal population in terms of salinity. On the scale of an individual sample, fluid inclusions with different salinities are spatially separated, and we see no evidence in the fluid inclusion record for fluid mixing during vein deposition. The bimodal salinity distribution of the fluid(s) at similar Th remains unexplained at this point, although it appears that two different fluids of contrasting salinity had alternating access to the vein system (Richards and Kerrich 1993). Our new data show that liquid-phase fluid inclusions from boiling assemblages belong almost exclusively to the high salinity population. In tandem with this observation, Richards and Kerrich (1993) reported that rare fluid inclusions from quartz intergrown with roscoelite-Au° bands also typically belong to the high salinity population. We therefore deduce a causative relationship between the high salinity fluids, phase separation, and gold deposition, and suggest that the high salinity fluid was trapped preferentially, whereas the CO_2-rich fluid was trapped only locally (cf. Hedenquist and Henley 1985, pp. 1394).

Homogenization temperatures of liquid-rich fluid inclusions from within and outside boiling assemblages, and from both salinity groups, are statistically indistinguishable. Although these Th values approximate the trapping temperature because of evidence for phase separation, trapping pressures cannot readily be calculated because of the presence of variable amounts of CO_2 and CH_4 in the fluid inclusions. Nevertheless, preliminary pressure estimates suggest values between 250 and 340 bars. Stratigraphic reconstructions suggest that the depth of emplacement of the intrusive complex and associated ore deposit was probably between 1.5 and 2 km below paleosurface (Davies 1983; Fleming et al. 1986) implying hydrostatic pressures of 150 to 200 bars, or lithostatic pressures of 400 to 500 bars. Thus, the pressures

indicated by the fluid inclusions are intermediate between hydrostatic and lithostatic values. Overpressuring of the vein fluids above hydrostatic conditions is consistent with sudden and rapid fluid flow in the veins, and the formation of hydrothermal breccias by explosive hydraulic fracturing.

The carbon dioxide concentration in typical epithermal systems is <1 mole % (Heald et al. 1987; Bodnar et al. 1985) but is relatively higher in hydrothermal gold deposits associated with alkalic rocks, as suggested by the abundance of clathrate in fluid inclusions (Mutschler and Mooney 1993; Richards 1995). For example, Richards et al. (1997) estimated a CO_2 concentration of ~1.5 mole % for pre-boiling fluids in stage II veins at Porgera. Only in rare cases, however, does CO_2 reach 4 mole % (~2.2 molal) in such deposits, the concentration required to form liquid CO_2 at room temperature (Hedenquist and Henley 1985). In this study, significant amounts of CO_2 were observed in vapor-rich fluid inclusions, suggesting that this gas was partitioned into the vapor phase during phase separation. The presence of dissolved gases, such as CO_2, in a hydrothermal fluid increases the pressure at which phase separation will occur at a given temperature (Takenouchi and Kennedy 1965; Bodnar et al. 1985), and this may explain the large vertical range (>700m) and unusual depth (1.5–2 km) of ore formation at Porgera. Similar fluid properties and depth of mineralization are observed at the Cripple Creek gold deposit, Colorado (Thompson et al. 1985), and the relative abundance of CO_2 in the hydrothermal fluids may, therefore, constitute a key difference between alkalic-type and calc-alkaline-associated epithermal deposits.

Conclusions

Direct evidence for phase separation has been found in quartz associated with high-grade ore at the Porgera gold deposit in the form of coexisting primary liquid-rich and vapor-rich (CO_2-bearing) fluid inclusions. We suggest that precipitation of gold was a direct consequence of this process, which resulted in the loss of H_2S to the vapor phase and destabilization of gold-bisulfide complexes in solution. Evidence for fluid oxidation and pH increase, both expected consequences of volatile exsolution, is found in the presence of carbonates and sulfates in fine-grained vein margins. Furthermore, the textural forms of hydrothermal breccias and fine-grained vein and

breccia margins are consistent with an origin by explosive phase separation, or flashing.

We suggest that the relatively gassy nature of fluids associated with alkalic-type gold deposits such as Porgera marks them apart from calc-alkaline-associated epithermal deposits, and may explain the characteristic large depth-range of ore deposition.

References

Bodnar RJ (1993) Revised equation and table for determining the freezing point depression of H_2O-NaCl solutions. Geochim Cosmochim Acta 57: 683–684

Bodnar RJ, Reynolds TJ, Kuehn CA (1985) Fluid-inclusion systematics in epithermal systems. Rev Econ Geol 2: 73–97

Brown PE, Hagemann SG (1994) MacFlinCor: A computer program for fluid inclusion data reduction and manipulation. In: De Vivo B, Frezzotti ML (eds.) Fluid Inclusions in Minerals: Methods and Application, Virginia Polytechnic Institute and State University Press, pp 231–250

Collins PLF (1979) Gas hydrates in CO_2-bearing fluid inclusions and the use of freezing data for estimation of salinity. Econ Geol 74: 1435–1444

Davies HL (1983) Wabag, Papua New Guinea—1: 250 000 geological series. Papua New Guinea Geol Survey Explanatory Notes, Sheet SB/54-8, pp 1–84

Drummond SE, Ohmoto H (1985) Chemical evolution and mineral deposition in boiling hydrothermal systems. Econ Geol 80:126–147

Fleming AW, Handley GA, Williams KL, Hills AL, Corbett GJ (1986) The Porgera gold deposit, Papua New Guinea. Econ Geol 81: 660–680

Fournier RO (1985) The behavior of silica in hydrothermal solutions: Rev Econ Geol 2: 45–61

Handley GA, Bradshaw PMD (1986) The Porgera gold deposit, Papua New Guinea. In: Macdonald AJ (ed) Gold '86. Konsult Internat, Willodale Ontario, pp 416–424

Heald P, Foley NK, Hayba DO (1987) Comparative anatomy of volcanic-hosted epithermal deposits: Acid-sulfate and adularia-sericite types. Econ Geol 82: 1–26.

Hedenquist JW, Henley RW (1985) The importance of CO_2 on freezing point measurements of fluid inclusions: Evidence from active geothermal systems and implications for epithermal ore deposition. Econ Geol 80: 1379–1404

Mutschler FE, Mooney TC (1993) Precious-metal deposits related to alkalic igneous rocks: Provisional classification, grade-tonnage data and exploration frontiers. In: Kirkham RV, Sinclair WD, Thorpe RI, Duke JM (eds) Mineral Deposit Modeling. Geol Assoc Canada Special Paper 40: 479–520

Richards JP (1990) Petrology and geochemistry of alkalic intrusives at the Porgera gold deposit, Papua New Guinea. J Geochem Exploration 35: 141–199

Richards JP (1992) Magmatic-epithermal transitions in alkalic systems: Porgera gold deposit, Papua New Guinea. Geology 20: 547–550

Richards JP (1995) Alkalic-type epithermal gold deposits — a review. In: Thompson JFH (ed) Magmas, fluids and ore deposits. Mineral Assoc Canada, Short Course Series 23: 367–400

Richards JP, Bray CJ, Channer DMDeR, Spooner ETC (1997) Fluid chemistry and processes at the Porgera gold deposit, Papua New Guina. Miner Deposita 32: 119–132

Richards JP, Kerrich R (1993) The Porgera gold mine, Papua New Guinea: Magmatic hydrothermal to epithermal evolution of an alkalic-type precious metal deposit. Econ Geol 88: 1017–1052

Richards JP, McDougall I (1990) Geochronology of the Porgera gold deposit, Papua New Guinea: Resolving the effects of excess argon on K-Ar and $^{40}Ar/^{39}Ar$ age estimates for magmatism and mineralization. Geochim Cosmochim Acta 54: 1397–1415

Thompson TB, Trippel AD, Dwelley PC (1985) Mineralized veins and breccias of the Cripple Creek District, Colorado. Econ Geol 80: 1669–1688.

Spycher NF, Reed MH (1989) Evolution of a broadlands-type epithermal ore fluid along alternative P-T paths: Implications for the transport and deposition of base, precious, and volatile metals. Econ Geol 84: 328–359

Takenouchi S, Kennedy GC (1965) The solubility of carbon dioxide in NaCl solutions at high temperatures and pressures. Am J Science 263: 445–454

Table 3-1: Ice melting, salinity, and $Th_{(L)}$ values for liquid-rich fluid inclusions from boiling assemblages and from liquid-rich-only groups. Number of samples analyzed shown in parentheses. $Th_{(L)}$ I refers to the lower $Th_{(L)}$ group within the boiling assemblages and $Th_{(L)}$ II is the calculated average for the higher $Th_{(L)}$ population (see Figure 3-5). Average salinity values for both Th populations in boiling assemblages fall in the high salinity group.

	boiling assemblage	liquid-rich only	
		low-salinity population	high-salinity population
Ice melting point (°C)	-5.0 ± 0.6 (86)	-2.8 ± 0.3 (47)	-5.0 ± 0.5 (137)
Salinity (wt % equiv NaCl)	7.8 ± 0.8 (86)	4.7 ± 0.5 (47)	7.8 ± 0.7 (137)
$Th_{(L)}$ I (°C)	154 ±16 (80)	139 ± 6 (47)	149 ± 15 (137)
$Th_{(L)}$ II (°C)	262±18 (7)		

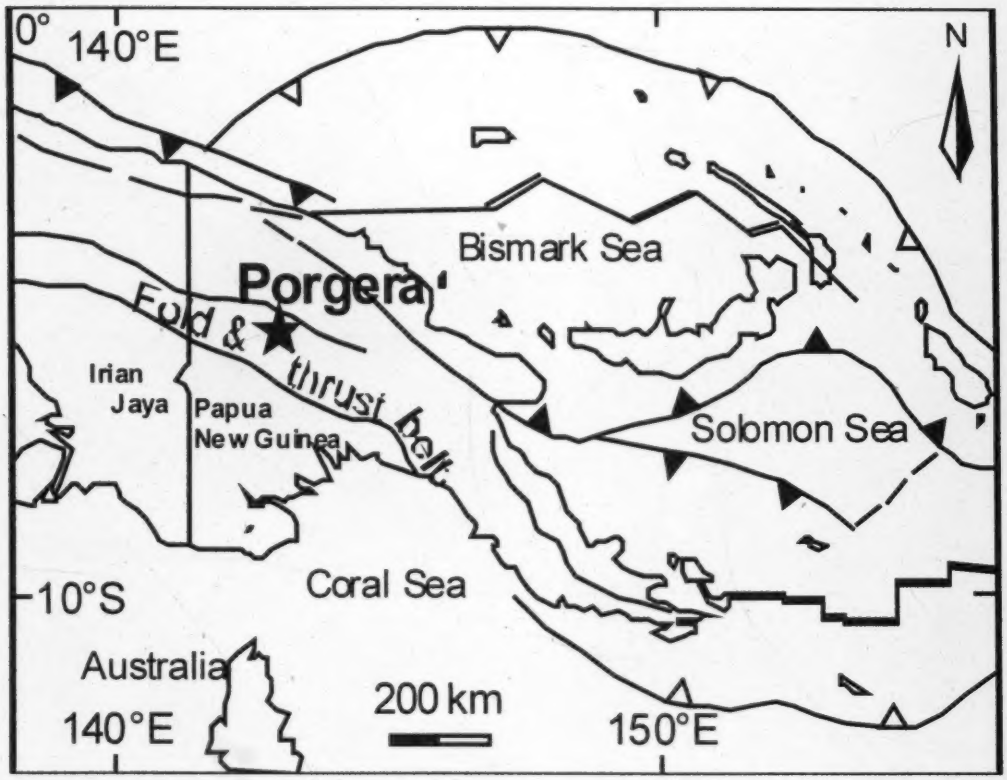

Figure 3-1: Simplified map showing the location of the Porgera gold deposit, Papua New Guinea (inset), and the geology of the surrounding area. Modified from Richards (1995).

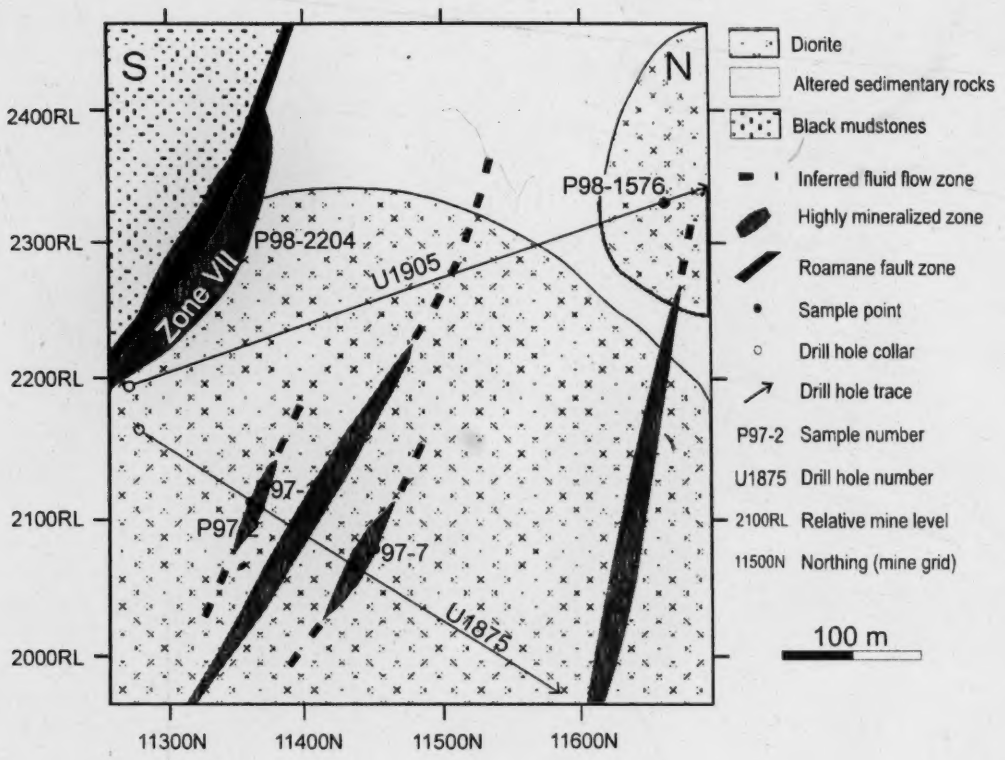

Figure 3-2: Simplified sketch section at 22260E (mine grid) showing sample locations and sample numbers. RL is relative mine level and corresponds to absolute elevation in meters above sea level. Drill holes U1905 and U1876 are indicated by thin straight lines with collars marked by open circles. Sample P98-2204 is from Zone VII, the highest grade area of the Porgera gold mine.

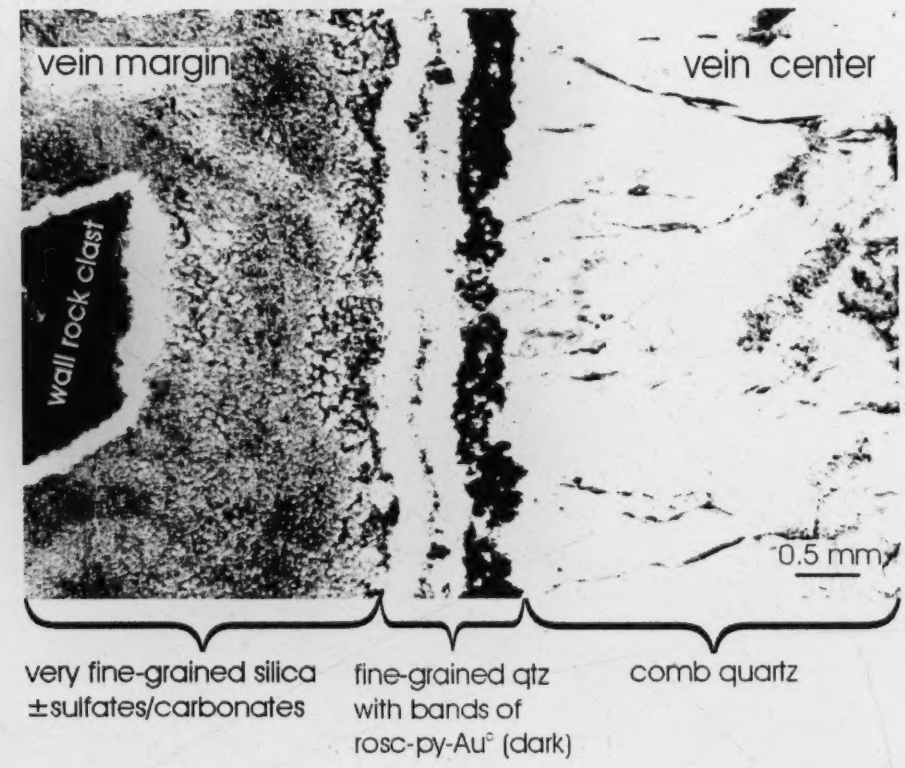

Figure 3-3: Typical banded stage II quartz-roscoelite-gold vein. The vein margin is characterized by a layer of very fine-grained silica ± sulfates and carbonates, followed by fine-grained quartz with bands of roscoelite-quartz-pyrite-gold. Barren comb quartz fills the vein center. Qtz = quartz, rosc = roscoelite, py = pyrite, Au° = gold.

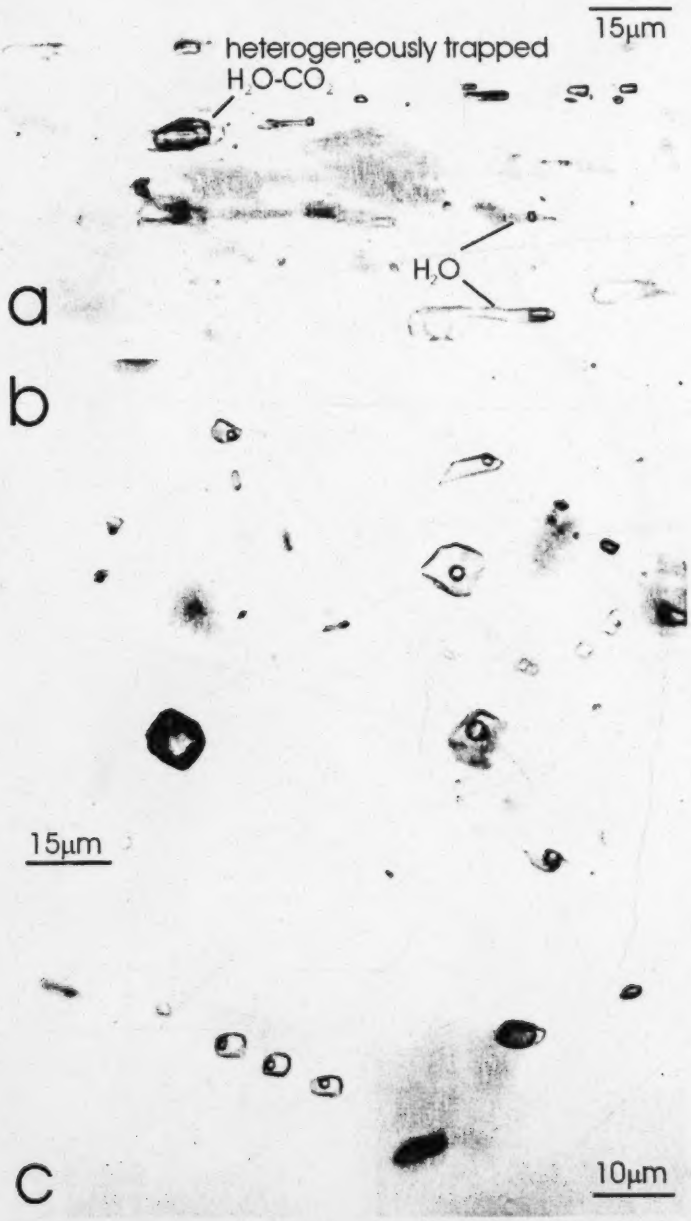

Figure 3-4: Photomicrographs showing coexisting primary liquid-rich and vapor-rich fluid inclusions in stage II quartz indicating boiling conditions. (a) Growth zone in quartz from sample P98-2204 from high-grade Zone VII. Note the three-phase fluid inclusion containing $CO_{2(l)}$, $CO_{2(v)}$, and $H_2O_{(l)}$, which is interpreted to be heterogeneously trapped from CO_2-rich vapor and H_2O-rich liquid; (b) P97-1; (c) P97-7.

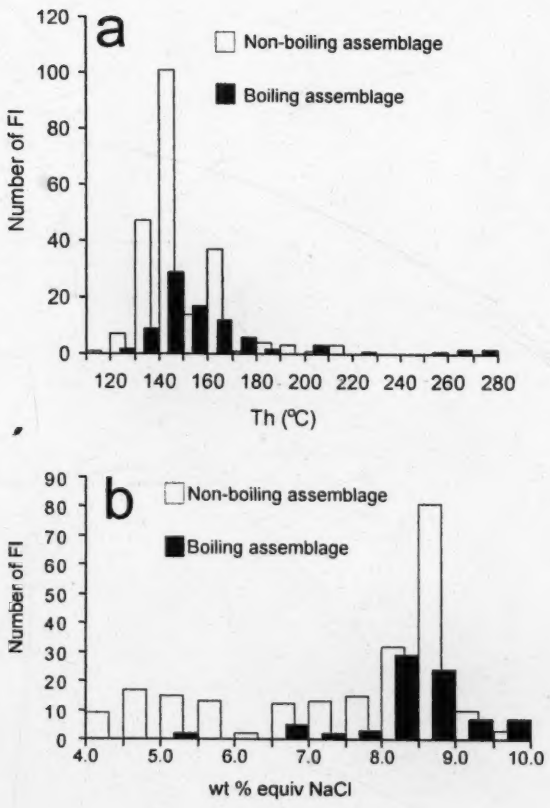

Figure 3-5: Histograms of (a) $Th_{(L)}$ (°C) and (b) salinity (wt % NaCl equiv) for liquid-rich primary fluid inclusions in quartz from boiling assemblages (black bars) and from groups of liquid-rich only inclusions (white bars). Note the statistically identical Th distribution. Salinity values of inclusions from non-boiling assemblages are bimodally distributed, whereas inclusions from boiling assemblages fall dominantly in the high salinity group.

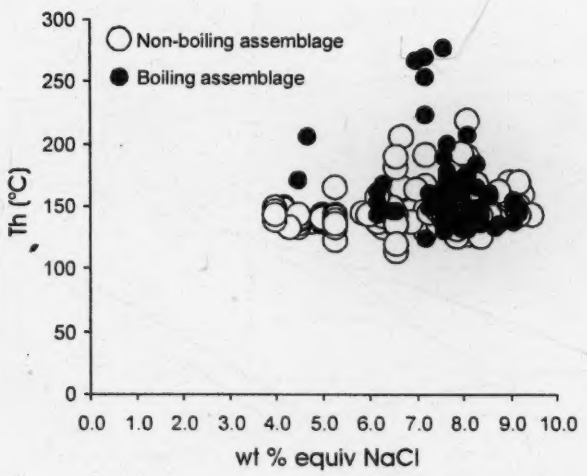

Figure 3-6: Th-salinity plot of fluid inclusion data from stage II quartz. Filled circles represent data from liquid-rich inclusions from boiling assemblages, open circles from liquid-rich-only groups. Note that inclusions from liquid-rich-only groups fall in both the low and high salinity groups, whereas the majority of inclusions from boiling assemblages fall in the high salinity group.

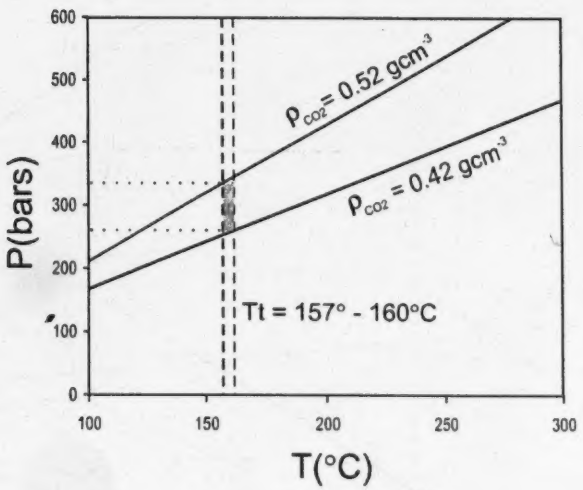

Figure 3-7: Pressure-temperature plot showing two CO_2 isochores and their intersection with the 160°C isotherm, representing the trapping conditions of a group of fluid inclusions undergoing phase separation (Tt = trapping temperature). Isochores were calculated from near critical CO_2 homogenization temperature using the program MacFlinCor (Brown and Hagemann, 1994), where $\rho = 0.52$ gcm^{-3} represents the calculated density for homogenization to the liquid phase, and $\rho = 0.42$ gcm^{-3} for homogenization to the vapor phase (it is not possible to calculate density for the critical composition using MacFlinCor). The trapping pressure is estimated by this method to be between 250 and 340 bars.

Chapter 4

Characteristics and evolution of the hydrothermal fluid in the North Zone high-grade area, Porgera gold deposit, Papua New Guinea

A version of this paper will be submitted to Economic Geology. The co-authors are J.P. Richards, Dept. of Earth and Atmospheric Sciences, University of Alberta, Edmonton, Alberta; M. H. Reed, Dept. of Geological Sciences, University of Oregon, Eugene, Oregon; J. Bray and E.T.C. Spooner, Department of Geology, University of Toronto; and P.D. Adams, Porgera Joint Venture, Porgera, Papua New Guinea.

Introduction

The Porgera gold deposit is located in the Pliocene fold and thrust belt that forms the highlands of Papua New Guinea (Fig. 4-1). With 10.3 million ounces of gold recovered between start of production in 1990 and June 2001, the mine is a significant gold producer in the Southwest Pacific region. Reserves and resources in June 2001 amount to 113 million tonnes of ore at a grade of 3.5 grams per tonne. The total contained gold at Porgera is thus ~20 Moz.

The deposit is hosted by 6 Ma-old alkalic intrusions and the sedimentary rocks into which the magmas were emplaced. Three types of gold-bearing vein assemblages occur: (1) Magnetite-sulfide-carbonate veins with minor gold (pre-stage I), (2) base-metal-sulfide±gold-carbonate veins (stage I), and (3) quartz-roscoelite-pyrite-gold veins (stage II).

Stage II hosts the highest gold grades and is economically most significant. The discovery of bonanza grades of gold in stage II veins hosted by a late normal fault and its splays, the Roamane Fault Zone, proved the economic potential of the deposit in 1983 (e.g., high-grade area called Zone VII where up to 1000 g/t Au occurred in quartz-roscoelite breccias; this area is now mined out). Much research has therefore

been focused on the quartz-roscoelite-pyrite-gold veins, and various different mechanisms for stage II ore formation have been proposed. Handley and Bradshaw (1986) and Handley and Henley (1990) suggested that boiling or fluid mixing could have occurred, but that the bonanza type zones were most likely a result of boiling (based on analogy with similar deposit types). Richards and Kerrich (1993) agreed with this interpretation and argued on the basis of mineralogical and textural grounds that vapor phase separation was responsible for stage II ore formation, a model further supported by fluid inclusion gas analyses (Richards et al., 1997). However, Wall et al. (1995) and Cameron (1998) concluded from studies of vanadium chemistry and mineralogical observations that mixing of an oxidized magmatic fluid and a reduced fluid expelled by carbonaceous sediments was responsible for the formation of high-grade zones. Most recently, Ronacher et al. (2000) suggested, on the basis of observations of coexisting vapor-rich and liquid-rich fluid inclusions in stage II quartz, that boiling* was, at least locally, responsible for ore formation.

This study focuses on a high-grade area, the North Zone, hosted by a diorite body and its surrounding sedimentary rocks in the footwall of the Roamane Fault (Fig. 4-2). Quartz-roscoelite-pyrite-gold veins were examined by petrography, fluid inclusion microthermometry and bulk crush-leach gas and ion chromatography, and stable isotope geochemistry (O, H, C, S) to characterize the hydrothermal fluid from which they formed. These data were used to simulate numerically mineral precipitation based on thermodynamic modeling using the software CHILLER (Reed, 1982, 1998) in order to determine the mechanism(s) of vein formation. Suggested mechanisms involved in high-grade ore formation are discussed in the light of previous hypotheses of ore deposition at Porgera.

*In this study, we use the term "boiling" to imply vapor phase separation of a saline, gas-rich fluid (c.f. Truesdell, 1985, p.7).

Geology of the Porgera gold deposit

Porgera Intrusive Complex

The Porgera gold deposit is hosted by a suite of mafic, sodic-alkalic intrusions, the Porgera intrusive complex (PIC), that was emplaced at an estimated paleodepth of ~2.0 to 2.5 km (Davies, 1983; Fleming et al., 1986). In absence of a classification scheme for subvolcanic alkalic rocks, Richards (1990) used LeBas et al.'s (1986) classification of volcanic rocks and determined that the hypabyssal intrusions were characterized by alkali basaltic, hawaiitic, to mugearitic compositions. Texturally, the plutons are gabbros, porphyritic diorites, and feldspar-porphyries, intruded as stocks (≤500 m diameter) and dikes.

The PIC was emplaced into Cretaceous sedimentary rocks (Chim Formation; Davies, 1983) in the latest Miocene (~6 Ma; Richards and McDougall, 1990; Ronacher et al., 2002). The sedimentary rocks are dominantly carbonaceous mudstones and calcareous siltstones deposited on the shelf of the Australasian plate margin (Davies, 1983; Gunson et al., 2000). Emplacement of the magmas occurred slightly prior to or during the uplift of the Papuan fold and thrust belt that occurred as a result of the collision of the Indo-Australian plate with the Bismarck Sea and Caroline oceanic plates (Hill et al., 1989, 2000).

The mineralizing event occurred immediately after the emplacement of the PIC (Ronacher et al., 2002), and was accompanied locally by intense phyllic alteration that affected the shallow level intrusions. A late steeply-dipping normal fault, the Roamane Fault, crosscuts all intrusions and hosts the richest gold-bearing veins and breccias.

Mineralization

Three mineralogically distinct gold-bearing vein parageneses are recognized at Porgera. Magnetite-sulfide-carbonate veins occur in the central and deep parts of the mine. Magnetite is the dominant mineral and contains lenses of pyrite, pyrrhotite, chalcopyrite, and rare inclusions of gold in pyrite. The main non-metallic mineral is calcite, and quartz is present in minor concentrations. This vein type is economically insignificant. Thin alteration selvages around the veins contain fine-grained biotite and

actinolite, and the age of the alteration biotite has been determined to be 5.98 ± 0.13 Ma (Ronacher et al., 2002). The magnetite-sulfide-carbonate veins are the oldest veins because they are cross-cut by all other vein types (Ronacher et al., 1999).

Higher gold grades than in the magnetite-sulfide-carbonate veins occur in base-metal-sulfide±gold-carbonate veins. Here, the dominant sulfide minerals are pyrite, sphalerite, and galena, with rare chalcopyrite, arsenopyrite, marcasite, freibergite, and proustite/pyrargyrite (Richards et al., 1991). Gold occurs as invisible gold in pyrite or as microscopic inclusions in pyrite. The gangue consists of complex Mn-Ca-Mg carbonates and subordinate quartz. Richards and Kerrich (1993) grouped these veins, together with disseminated, auriferous pyrite, as stage I mineralization. Both, the veins and the disseminated ore are accompanied by intense phyllic alteration consisting of fine-grained muscovite/illite and carbonate. Richards and Kerrich (1993) determined an average homogenization temperature (Th) of fluid inclusions in stage I quartz of 299° ± 33°C (n = 274), and a salinity of 9.5 ± 1.8 equivalent weight percent NaCl (equiv. wt. % NaCl). After correcting for estimated pressure, a trapping temperature (Tt) of ~ 325°C was calculated.

The economically most significant vein assemblage, stage II, is characterized by quartz-roscoelite[$K(V,Al)_2(Si_3AlO_{10})(OH)_2$]-pyrite-gold veins and breccia veins (Fig. 4-3). A list of all ore minerals described from stage II is shown in Table 4-1 (Fleming et al., 1986; Handley and Henry, 1990; Richards et al., 1991; Richards and Kerrich, 1993). Some pyrite was reported to be occasionally arsenian, and locally, arsenopyrite occurs in addition to pyrite; chalcopyrite is rare. Gold occurs dominantly as native gold and electrum. The Ag-Au tellurides petzite, krennerite, calaverite, and hessite were described from the deposit as well as coloradoite (HgTe) and altaite (PbTe; Handley and Bradshaw, 1986; Handley and Henry, 1990; Richards et al., 1991), but only minor hessite was observed in the samples analyzed for this study. Tellurides appear to have been most abundant in Zone VII, the richest zone of the mine hosted by the Roamane Fault Zone. In this area, proustite was also observed in rare cases as a late mineral intergrown with coarse grained quartz, and minor barite was reported to occur locally with roscoelite and quartz (Richards and Kerrich, 1993). In some veins from the North

Zone, tetrahedrite is intergrown with quartz, and qualitative electron microprobe analyses showed that this mineral is rich in Ag and contains traces of Fe and Zn. Vugs in the centers of stage II veins are locally filled with carbonate or anhydrite, and in some samples, earlier Ca-Fe-Mg carbonate is intergrown with the coarse grained quartz. Massive anhydrite fills late meter-wide veins within the Roamane Fault Zone; however, these veins contain no roscoelite and little gold. All other minerals listed in Table 4-1 occur only locally and in trace amounts.

Stage II veins in the high-grade areas within the Roamane Fault Zone (e.g., Zone VII) are texturally distinct from the North Zone stage II veins. The former are typically banded: the outermost band consists of fine-grained quartz with minor pyrite, barite, and carbonate, followed inward by a band of brown-green roscoelite intimately intergrown with pyrite, gold, minor quartz, and locally barite. This band is overlain by a layer of coarse-grained comb quartz. This sequence repeats in some places, and the vuggy vein centers are typically either empty or filled with Ca- Fe-Mg carbonate or anhydrite (Richards and Kerrich, 1993; Ronacher et al., 2000a). In contrast, stage II veins in the North Zone exhibit three different textural styles: (1) Banded veins with a layer of roscoelite, pyrite, gold, and minor quartz rimming the wall rock where roscoelite occurs abundantly as rosettes in the veins; this band is followed by a layer of quartz, and locally the vuggy center is filled with anhydrite or carbonate; these veins are typically not wider than one centimeter and locally, the quartz-rich center is missing and the veinlet consists of roscoelite, pyrite, gold, and minor quartz only; wall rock alteration around these veins consists of thin alteration haloes of fine-grained muscovite/illite, carbonate, and pyrite, and rare adularia. These altered haloes are typically only 5 mm wide (e.g., Figs. 3a,b; 4a,b,c); (2) breccias and breccia veins with angular clasts of wall rock rimmed by bands of roscoelite, pyrite, gold, and minor quartz; the clasts are supported by a matrix of quartz; the wall rock alteration in these brecciated zones may widen to several tens of centimeters (e.g., Fig. 4-3b); (3) thin (≤1 cm) veinlets with roscoelite, pyrite, gold in the wall rock alteration and quartz in the vein (e.g., Fig. 4-4d,e,h,f).

Fluid inclusions in the coarse-grained quartz of stage II veins from the Roamane Fault Zone are characterized by average Th values of 146° ± 13°C (n = 519; Richards

and Kerrich, 1993) and inclusions from the North Zone exhibit average Th values of 149° ± 15°C (n=137; Ronacher et al., 2001). Richards and Kerrich (1993) determined a bimodal salinity distribution of 4.2 ± 0.3 (n = 104) and 7.8 ± 0.7 equiv. wt. % NaCl (n = 346) in their samples; similar results were obtained in the present study except that the majority of inclusions fall in the high salinity group (see below).

Samples

Samples of quartz-roscoelite-pyrite-gold veins were collected from a high-grade ore zone, identified as the "North Zone", hosted by a diorite body and its surrounding sedimentary rocks in the footwall of the Roamane Fault (Figure 4-2). Because the ore shoot forms a steeply dipping tabular body parallel to the Roamane Fault but at depth its dip flattens towards the fault, it is interpreted to be a splay of the Roamane Fault. Its known depth extension down dip is approximately 600 m, and it consists dominantly of quartz-roscoelite-pyrite-gold veins, veinlets, and breccia veins with abundant gold, locally up to several hundred grams per tonne. Drill core samples were taken along a large part of the ore shoot with the aim of determining variations in ore and gangue mineral assemblages, and microthermometric properties and geochemical and isotopic compositions of fluid inclusions in quartz.

Analytical Methods

Fluid inclusion microthermometry

Fluid inclusion microthermometry was conducted on a Linkam THMSG 600 heating and freezing stage calibrated using synthetic fluid inclusions manufactured by Syn Flinc. Measurements below 31.1°C, the critical point of CO_2, are accurate to ±0.1°C, and measurements above this temperature are accurate to ±1°C. Salinities were modeled using the equation of Bodnar (1993) for the H_2O-NaCl system.

Gas and ion chromatography

Bulk crush-leach combined gas and ion chromatography was conducted on 19 samples of quartz from quartz-roscoelite-pyrite-gold veins. Large quartz grains (~1 mm^3) were hand-picked under a binocular microscope, then soaked in aqua regia followed by brief rinse with hydrofluoric acid to remove surface impurities. The samples were then washed with pure water, and three to five grams of this quartz were cleaned using electrolytic cleaning cells according to the technique outlined by Roedder (1958). The chromatographic analyses were conducted at the F.G. Smith Fluid Inclusion Laboratory at the University of Toronto. For gas chromatography, a 1 to 2 gram aliquot was placed into a stainless steel cylinder and flushed with He overnight. Subsequently, the sample was crushed in one step, and the gas released was analyzed using a Hewlett Packard HP 5890A gas chromatograph fitted with a thermo-conductivity detector and a photo-ionization detector. Standard gas mixtures were injected for calibration. Details of the protocol are outlined in Bray et al. (1991).

The crushed residue was leached with ultra-pure water, diluted to 10 ml leachate, and analyzed using a Dionex 2000i/SP ion chromatograph with an Ion Pac AG9-SC 4mm guard column and an Ion Pac AS9-SC 4mm analytical column. The technique is described in detail by Channer and Spooner (1992), and Channer and Spooner (1994) discuss accuracy, precision, and detection limits. The analytical precision for the gas species was determined using standard gas mixtures and is better than 10%; precision is better than 15% for ionic species based on 35 standard runs (Channer and Spooner, 1994). Brazilian quartz cleaned in the same manner as the samples was used as a blank. Analyses were rejected if the blank value exceeded 25% of the measured value.

The concentrations of the ionic species are calculated by combining the gas and ion chromatographic data and relating the amount of ionic species to the amount of H_2O analyzed (c.f. Channer and Spooner 1999).

Light stable isotopes

All stable isotope data are reported in the conventional delta notation; oxygen and hydrogen isotope ratios are reported relative to VSMOW, carbon isotopic ratios relative to VPDB, and sulfur isotopes relative to VCDT.

Oxygen isotopic analyses on quartz were conducted on 10 to 20 mg of cleaned, hand-picked quartz using the bromine pentafluoride method of Clayton and Mayeda (1963), and analyzed on a Finnigan MAT 252 multiple collector mass spectrometer. The analytical precision is ±0.2‰, and accuracy is ±0.2‰. Isotopic fractionation between quartz and water was calculated using the equation of Clayton et al. (1972) at temperatures defined by fluid inclusion homogenization. Oxygen isotopic analyses on Ca-Fe-Mg carbonates were conducted using 100% H_3PO_4 at 50°C and using an acid fractionation factor for ankerite of 1.01060 (Kontak and Kerrich, 1997). The analytical precision is ±0.2‰, and accuracy is ±0.5‰.

The hydrogen isotopic composition of fluid inclusion water was determined by thermal decrepitation (heating to ~1200°C) of fluid inclusions in hand-picked, cleaned quartz. CO_2 and H_2O were trapped in a U-tube cooled by liquid nitrogen, and all other gases (e.g., CH_4, N_2) were pumped away prior to cooling the U-tube with ethanol which releases CO_2 that is pumped away leaving H_2O behind. The water was reduced to H_2 by passing it over depleted uranium before transferring it to the mass spectrometer. The accuracy is within ±3‰.

Carbon isotopes were analyzed on Ca-Fe-Mg carbonate from stage II veins. CO_2 was extracted from ~20 grams of these carbonates using 100% H_3PO_4 at 50°C. The accuracy is ±0.2 ‰.

Organic carbon was analyzed by crushing the rock, removing carbonates by rinsing in dilute acid (10% HCl), and then running the dried residue through a combustion furnace at 1020°C in the presence of pure oxygen. The furnace is linked to a SIRA II mass spectrometer. Accuracy is ±0.5 ‰.

The carbon isotopic composition of CO_2 in fluid inclusions was analyzed on one sample by crushing the quartz in a ball mill with special gas ports, from which the gas was extracted with a syringe and transferred into a HP 6890 gas chromatograph.

The gas is carried by the He carrier gas to the mass spectrometer (Micromass IsoChrom mass spectrometer). The accuracy is within ±0.5 ‰.

Sulfur isotopes were analyzed using a continuous-flow isotope-ratio mass spectrometer (Carlo Erba *NA 1500* elemental analyzer interfaced to a magnetic-sector mass analyzer). The sulfide sample was oxidized with $O_{2(g)}$ and transported to the mass spectrometer in a He carrier gas. The accuracy is within ±0.7 ‰.

Results

Fluid inclusion microthermometry

Fluid inclusion microthermometry was conducted on 27 samples of stage II quartz-roscoelite-pyrite-gold veins from the North Zone high-grade area, and one sample from the Zone VII high-grade area in the Roamane Fault Zone. The dominant host of the fluid inclusions is the coarse-grained comb quartz that overlies the gold- and pyrite-bearing roscoelite bands. Inclusions in minor quartz intergrown with roscoelite are rare, small, and most are unworkable. Only primary and pseudosecondary inclusions were selected for analysis according to the criteria of Roedder (1984), and secondary inclusions are mostly small, unworkable, and volumetrically insignificant. Examples of representative groups of fluid inclusions are shown in Figure 4-5.

The fluid inclusions are typically 2-phase, liquid-rich, and irregular in shape, characteristic of low temperature trapping conditions (Bodnar et al., 1985). In seven of the 27 analyzed samples from the North Zone, vapor-rich inclusions were also observed coexisting with the dominant liquid-rich inclusions (Fig. 4-5c). These assemblages include heterogeneously trapped 3-phase inclusions consisting of liquid CO_2, CO_2-vapor, and minor amounts of liquid H_2O. No eutectic melting was observed in any of the samples.

Table 4-2 lists average homogenization temperatures (Th) and salinity values of two-phase aqueous inclusions of 27 samples from the North Zone and one sample from the Roamane Fault Zone (P98-2204), and Figure 4-6 shows Th-salinity graphs for representative individual samples, whereas Figure 4-7 shows a Th-salinity graph of *all*

samples from the North Zone. CO_2 concentrations known from gas chromatography may be used to correct salinity estimates from ice melting points but, because CO_2 concentrations are not known for all samples and because the CO_2 concentrations are variable, a general correction for all samples would be inappropriate (although corrections were calculated for those samples where CO_2 measurements are available; see below); apparent salinity values used to construct Figure 4-6 and 4-7 are therefore uncorrected.

The absence of liquid CO_2 in the liquid-rich aqueous inclusions constrains the CO_2 content to <2.2 molal CO_2 (Hedenquist and Henley, 1985). CO_2 concentrations ≤2.2 molal CO_2 can depress the ice melting point by up to 4°C in pure water, and thus increase apparent salinity by up to 6.5 equiv. wt % NaCl (Hedenquist and Henley, 1985: equation 4). The maximum concentration of CO_2 in the samples analyzed in this study is 1 molal CO_2, which equates to a freezing point depression of ~1.9°C and a maximum increase in apparent salinity of ~3.2 equiv. wt % NaCl.

All samples exhibit a dominant grouping of apparent salinity of ~7-10 equiv. wt. % NaCl, and 5 of the 27 samples from the North Zone show an additional cluster of salinity values from 4 to 5 equiv. wt. % NaCl. The number of individual inclusions containing the lower salinity fluid is significantly smaller than the number of inclusions of higher salinity (Fig. 4-8), and the low salinity inclusions are mostly located in the vein centers, whereas the high salinities occur towards the vein margin. Both groups exhibit similar average Th values. Three samples exhibit a more complete range of salinity values from ~4 to ~10 equiv. wt. % NaCl (P98-1164, P99-145, P98-611).

Average values of Th for different samples range from 127° ± 12°C (n = 37) to 167° ± 25°C (n = 27; Table 4-2; see below for a discussion of trapping temperature).

Vapor-rich inclusions were typically completely filled with vapor so that microthermometric phase changes were not visible. In the three-phase heterogeneously-trapped inclusions from samples from the North Zone (P98-1576, P98-701, P98-066C, P99-197, P98-1835, P98-611), Tm_{CO_2} could be measured (average Tm_{CO_2} = –56.6° ± 0.1°C, n = 27; Th_{CO_2} = 26.9 ± 1.9, n = 26), and clathrate melting (Tm_{clath}) ranged from 7.0° to 8.8°C (average 7.4° ± 0.5°C, n = 26; estimated by observing instantaneous

bubble movement). Salinity values calculated from these Tm_{clath} data using the software Flincor (Brown and Hagemann, 1994) range from 2.4 to 5.7 equiv. wt % NaCl (average 4.6 ± 0.9 equiv. wt % NaCl) and give an estimate of the salinity of the heterogeneously trapped aqueous phase in these inclusions. Heterogeneous entrapment is further indicated by the anomalously high total homogenization temperatures of approximately 300°C, and the fact that some inclusions homogenize to the liquid and others to the vapor phase; still others decrepitated before total homogenization.

In rare cases (P98-2204 and P 124 from the Roamane Fault Zone), a phase other than CO_2 was observed in some fluid inclusions. This phase formed a second bubble in addition to the H_2O vapor bubble, suggesting that this phase may be an immiscible organic compound that was trapped heterogeneously. In sample P124, the hydrocarbon occurred in an assemblage of low-salinity inclusions, and the H_2O vapor bubble homogenized at 135°C and the organic-rich bubble at 180°C, whereas in sample P98-2204 the hydrocarbon occurred in an assemblage of high-salinity inclusions, and the H_2O vapor bubble homogenized after the hydrocarbon bubble.

Gas and ion chromatography

Gaseous species detected include H_2O, CO_2, CH_4, N_2, C_2H_4, C_2H_6 (including C_2H_2), and COS (Table 4-3), and ionic species detected include Cl^- and Br^-, Li^+, Na^+, K^+, NH_4^+, Mg^{2+}, and Ca^{2+} (Table 4-4). SO_4^{2-} was also measured, but the SO_4^{2-} value reflects the original concentration of SO_4^{2-} in the fluid plus some reduced S, which is partially or fully oxidized during analysis in the chromatograph columns. Thus, H_2S, if present, would not have been detected, and the measured SO_4^{2-} value gives a minimum estimate for the total amount of sulfur in the fluid. Those samples in which vapor-rich inclusions were observed are distinguished with an asterisk after the sample number in Table 4-3, and were excluded from calculations of the gas content of the original hydrothermal fluid because boiling results in a concentration of gases in the vapor phase.

Q^+/Q^- (Table 4-4) is the ratio of total cationic to anionic charge (Channer and Spooner, 1992). Deviation from the ideal value of 1 is due to the presence of ions that

cannot be measured with this technique (e.g., CO_3^{2-}, HCO_3^-, HS^-, Fe^{2+}, Mn^{2+}) as well as analytical error and sulfide oxidation. Q^+/Q^- is >1 for all samples indicating a deficiency of anions. A correction for carbonate species was conducted using the measured amount of CO_2, because CO_2 is presumed to have been dissolved in the original liquid as carbonate/bicarbonate species (except in the case where fluid inclusion evidence for a vapor phase is present). The charge balance was recalculated assuming that all CO_2 was dissolved as either HCO_3^- or as CO_3^{2-}. The bicarbonate assumption resulted in reasonable values for Q^+/Q^- whereas carbonate ion resulted in exceedingly low values for Q^+/Q^-; and the values for charge balance shown in Table 4-4 are therefore recalculated for the presence of HCO_3^-. The corrected charge balance values are generally closer to one than the uncorrected values (even in those samples where minor liquid CO_2 was observed in vapor-rich inclusions) suggesting that bicarbonate was an important ionic constituent of the ore fluid. However, nearly all of the corrected Q^+/Q^- values are less than one, suggesting that the HCO_3^--only correction may have overcorrected. Such overcorrection is likely given that the pKa (H_2CO_3) is in the near-neutral pH range (e.g., pKa = 6.7 at 150°C). The wall rock alteration indicates that the fluid was moderately acidic, thus it is likely that a substantial amount of dissolved carbonate was H_2CO_3.

Light stable isotopes

Oxygen and hydrogen

$\delta^{18}O$ values for quartz from stage II veins range from 13.9‰ to 18.3 ‰. Values for water ($\delta^{18}O_{H_2O}$) in equilibrium with quartz were calculated using average Th values measured in each sample (assuming Th ≈ trapping temperature, Tt) because of local evidence for boiling; see Interpretation of Analytical Data), and the fractionation equation of Clayton et al. (1972). Calculated $\delta^{18}O_{H_2O}$ values range from –1.4 to 4.1‰ using average Th values. To assess the sensitivity of the method to temperature uncertainties, calculations were also conducted for Th + 25°, in which case the $\delta^{18}O_{H_2O}$ values range from 0.6 to 5.9‰ (a difference of approximately 2‰).

Oxygen isotope values of stage II carbonates intergrown with coarse-grained quartz (as opposed to the more abundant vug-filling carbonate) range from 15.2‰ to 16.6‰ (average = 15.9 ± 0.5‰, n = 5), and $\delta^{18}O$ of the fluid was calculated using the equation of Zheng (1999) for ankerite and a temperature of 160°C, and the values range from 2.2 to 3.6‰ (average = 2.9 ± 0.5‰, n = 5).

Hydrogen isotopic values of water in fluid inclusions in stage II quartz range from –81‰ to –52‰.

Carbon

Carbon isotopes were analyzed in stage II vein carbonate intergrown with coarse-grained, organic carbon and carbonate from the sedimentary country rocks, and one sample of CO_2 from bulk inclusion fluid; the results are shown in Table 4-6. Stage II carbonates display a narrow range of $\delta^{13}C$ of –3.3‰ to –2.4‰ with an average value of –2.7‰ (± 0.3, n = 6). $\delta^{13}C$ values for carbonate in unaltered mudstones and siltstones are between –1.5‰ and 0.0‰ (average –0.9 ± 0.6‰, n = 4), whereas carbonate in altered rocks exhibits values of -5.4‰ to –4.0‰ (average –4.6 ± 0.5‰, n = 4; Richards and Kerrich, 1993; this study). Organic carbon in the sedimentary rocks has a $\delta^{13}C$ of –23.6‰ to –16.8‰ (average -20.7 ± 2.2‰, n = 6). $\delta^{13}C_{CO_2}$ of CO_2 in fluid inclusions from sample P98-2204 is –9.5‰.

Sulfur

$\delta^{34}S$ values for pyrite range from –9.4 to 6.1‰, and values for late, vug-filling anhydrite range from 12.4 to 17.5‰ (Table 4-7). Sulfur isotope composition of the sedimentary host rocks was determined on a carbonaceous mudstone ($\delta^{34}S$ = 2.1‰), on a calc-arenite ($\delta^{34}S$ = 5.9‰), and on an altered carbonaceous mudstone ($\delta^{34}S$ = –12.7‰). The latter values are for bulk rock sulfur, but petrographic observations show that essentially all S is in pyrite.

Interpretation of analytical data

Fluid inclusion microthermometry

Apparent salinity values, shown in Table 4-4 and displayed against average Th in Figures 4-6 and 4-7, exhibit three patterns: (1) Most salinity values cluster between 7 and 9 equiv. wt. % NaCl (e.g., P98-846, P98-1448, P98-1170); (2) a bimodal distribution of ~4 to ~5 and ~7 to ~9 equiv. wt % NaCl was observed in several samples (e.g., P98-120, P99-231, P98-1537); and (3) some samples display a full range of salinities from ~4 to ~10 equiv. wt. % NaCl (P99-145, P98-611, P98-1164). The majority of samples from the North Zone (19 of 27) fall in category one, whereas six samples are bimodally distributed, and three exhibit a full range of salinity values. The salinity in the sample from The Roamane Fault Zone (P98-2204) is bimodally distributed, consistent with data previously reported by Richards and Kerrich (1993) in which most samples displayed bimodal populations (4.3 ± 0.4 equiv. wt. % NaCl, n = 119, and 7.8 ± 0.7 equiv. wt. % NaCl, n = 439).

The apparent salinity values plotted in Figure 4-6 are not corrected for the presence of up to 2 mole % CO_2 (as analyzed by gas chromatography) for reasons outlined in the Results section. Recalculation of salinity taking CO_2 into account (for those samples where the CO_2 concentration is known) was conducted according to the procedure described by Hedenquist and Henley (1985):

$$T_m = -(K_{Na^+} \times m_{Na^+} + K_{Cl^-} \times m_{Cl^-} + K_{CO_2} \times m_{CO_2})$$

where T_m is the melting point of ice, K_{Na^+} and K_{Cl^-} are 1.72 Kelvin/mole, K_{CO_2} = 1.86 Kelvin/mole, and m_{CO_2} is the molality of CO_2. The recalculation results in a decrease of the apparent salinity values by between 0.9 and 2.5 equiv. wt. % NaCl (Table 4-8).

Using Hedenquist and Henley's (1985) equation, salinity calculations based simply on the Cl^- values obtained from ion chromatography and assuming that Cl^- is present as NaCl resulted in bulk salinities between 1.8 and 3.7 equiv. wt. % NaCl (average 2.8 ± 0.5, n = 19), whereas values based on the slightly higher Na^+ concentrations resulted in bulk salinities between 3.7 and 7.5 equiv. wt. % NaCl

(average 5.9 ± 1.9, n = 19). Richards et al. (1997) explained the higher Na^+ concentration relative to Cl^- by assuming the presence of an additional anion such as bicarbonate. The bulk salinities calculated using Cl^- concentrations are generally lower than the salinities measured microthermometrically, and also lower than the salinities corrected for the presence of CO_2, but the salinities calculated using the Na^+ concentration are close to the microthermometrically measured and CO_2-corrected salinities. The presence of minor salts other than NaCl may account for some of the remaining difference but the microthermometric analyses do not indicate significant amounts of salts such as KCl or $CaCl_2$ (although small amounts of K^+ do occur in some samples; Table 4-4). Also note that there is a 15% uncertainty for the ion data which may account for some of the discrepancy. We interpret the CO_2 corrected microthermometry data as most representative of the true salinity because a salinity calculation base on a single ion only (e.g., Na^+ or Cl^-) ignores the effect of all other ions in the solution.

In samples that contain fluid inclusions exhibiting bimodal salinity groups, the high salinity inclusions occur close to the vein edge whereas the low salinity inclusions occur towards the vein center, suggesting that these fluids were not present coevally in the veins. Average Th values of inclusion groups with different salinities overlap within error, but in Figures 4-6c to 4-6f it appears that some samples exhibit lower Th values for the lower salinity group (e.g., P98-1164) whereas others show similar Th values (e.g., P99-145).

The different salinity patterns do not correlate to a particular vein type; for example, two of the three samples that show a continuous salinity trend are quartz veins with a roscoelite-pyrite-quartz band at the vein edges (P98-611, P98-1164), whereas the third sample (P99-145) is a breccia vein with angular clasts of altered mudstone in a matrix of quartz and minor carbonate; vuggy cavities contain euhedral quartz and carbonate. Visible gold was only found in sample P98-1164. Likewise, the samples exhibiting a bimodal salinity distribution show various textures: P98-1537 is a breccia vein with quartz matrix and a thin (1 mm) band of roscoelite-pyrite-quartz rimming the wall rock; P99-197 is also a breccia vein with quartz and carbonate matrix

and roscoelite rimming the wall rock; visible gold was found in this sample; P98-120 is a ~2cm thick quartz vein with thin (~2mm) roscoelite bands; P99-178 is a 8cm thick quartz vein with thin (~1mm) roscoelite bands in quartz; this sample also contained visible gold; and P99-231 consists of a network of quartz veinlets and veins (1mm to 1cm thick) where the thicker veins contain small clasts of black shale rimmed by roscoelite and abundant visible gold. Sample P98-2204 from the Roamane Fault Zone is a breccia with clasts of altered diorite rimmed by roscoelite-pyrite -gold-quartz and cemented by quartz. The high salinity group only pattern occurs in all vein texture types.

Whereas the continuous salinity trends are interpreted to be the result of fluid mixing, vapor-rich fluid inclusions coexisting with liquid-rich inclusions in some samples (Figure 4-5c) indicate that boiling took place during the formation of at least some stage II quartz veins. Gold was observed to be directly intergrown with quartz hosting coexisting liquid-rich and vapor-rich fluid inclusions in only one sample from a high-grade area close to the Roamane Fault Zone (Ronacher et al., 2000b), but not the samples from the North Zone. In the former case, a direct link between boiling and gold precipitation was suggested (Ronacher et al., 2000b), but this argument cannot be made so clearly for the North Zone.

No pressure correction was applied to the Th values because of local evidence for boiling; this approach is suggested by similar average Th values for fluid inclusion groups with and without coexisting vapor-rich inclusions (Figure 4-9). The highest average Th in stage II quartz is 167° ± 25°C (Th of individual inclusions reach values of 200°C), and this sample (P98-1835) contains vapor-rich, heterogeneously trapped inclusions indicating that boiling took place and that Th ≈ Tt.

Fluid inclusion gas contents

As described in the Results section, samples containing liquid-rich inclusions only and samples with coexisting liquid-rich and vapor-rich inclusions were analyzed. Their average gas contents are the same within error (e.g., average CO_2 content of

samples containing liquid-rich inclusions only is 1.31 ± 0.40 mole%, n = 16; and the average CO_2 content of samples containing rare vapor-rich inclusions in addition to liquid-rich inclusions is 1.13 ± 0.30 mole%, n = 4). This similarity suggests that the contribution of gas from gas-rich inclusions was insufficient to change the bulk gas content, which is consistent with the small number of gas-rich relative to liquid-rich inclusions observed. However, C_2H_6 appears to occur preferentially in samples exhibiting a bimodal salinity distribution as opposed to those samples in which high salinity inclusions only occur. For example, three of the five samples that show bimodal salinity also contain ethane (C_2H_6 = 0.0005 mole% to 0.00209 mole%) whereas only one of 11 samples exhibiting high salinity only contain C_2H_6 (0.0009 mole%). No clear correlation between gas content and salinity patterns or vein textures and could be observed for the other gases.

Ion chromatography

Concentrations of individual ions and ion ratios have been used to infer the sources of ore-forming fluids. Böhlke and Irwin (1992) determined characteristic Br^-/Cl^- and I^-/Cl^- ratios for the magmatic and geothermal environments and seawater, and the Br^-/Cl^- ratios are shown on Figure 4-10 together with the data from Porgera. Porgera fluids range from 0.8×10^{-3} to 1.9×10^{-3} with one outlier of 2.6×10^{-3} (average value of $1.2 \pm 0.2 \times 10^{-3}$, n = 22), and overlap the composition of seawater (1.5×10^{-3}). Böhlke and Irwin's (1992) value for magmatic water ($\sim 0.9 \times 10^{-3}$) lies just outside the Br^-/Cl^- range measured at Porgera, but data from Creede, Colorado (interpreted by Böhlke and Irwin (1992) to be typical of epithermal fluids) fall within the range of Porgera fluids.

Stable isotopes

Oxygen and Hydrogen

Oxygen isotope compositions of water in equilibrium with quartz fall between the values typical of meteoric water and Porgera magmatic water (Richards and

Kerrich, 1993; Fig. 4-11), and hydrogen isotopic compositions of stage II water range from slightly lower than Porgera magmatic water to similar to Porgera magmatic water. For comparison, Richards and Kerrich's (1993) data from the Roamane Fault Zone are also plotted in Figure 4-11. Note that for Richards and Kerrich's samples a 25°C temperature correction was applied to Th to calculate $\delta^{18}O_{H_2O}$ from $\delta^{18}O_{qtz}$ because no clear evidence for boiling was observed in the fluid inclusion record from these samples. A pressure correction was not applied to the Th values collected in this study for the reasons outlined above.

Both the oxygen and hydrogen isotope compositions of the samples from the North Zone are lighter than those from the Roamane Fault Zone (Richards and Kerrich, 1993). This difference is not an artifact of the Th values used to calculate $\delta^{18}O_{H_2O}$ from $\delta^{18}O_{qtz}$ and is still present if a 25°C correction is applied to Th for samples from the North Zone. Hence, the slightly distinct $\delta^{18}O$ are interpreted to reflect true differences in the isotopic composition of the fluid from which stage II veins formed in the Roamane Fault Zone and in the North Zone (see below for discussion).

There is no correlation between oxygen and hydrogen isotope data and fluid inclusion salinity patterns. For example, samples P98-611 and P98-1164 both show a continuous salinity trend but their $\delta^{18}O_{H_2O}$ values are at the opposite ends of the range, i.e. –0.5‰ and 3.1‰ respectively. Likewise, there is no relationship between $\delta^{18}O_{H_2O}$ and δD_{H_2O} and vein textures. $\delta^{18}O_{H_2O}$ values of breccias range from –1.2‰ to 3.3‰, and $\delta^{18}O_{H_2O}$ values of quartz-roscoelite-pyrite-gold veins range from –0.1‰ to 3.5‰.

Carbon

The average carbonate carbon isotope composition of altered sedimentary rocks is –4.6‰ which is similar to the composition of stage I carbonates (from –7.1 to –4.5‰; Richards and Kerrich, 1993). These values were interpreted to reflect a magmatic origin for the fluid that altered the sedimentary rocks and that formed stage I carbonate veins (Richards and Kerrich, 1993). In contrast, unaltered sedimentary rocks exhibit an average carbonate carbon isotope composition of -0.9 ± 0.6‰ ($n = 4$). The

average values of stage II carbonate is –2.7 ± 0.3‰ (n = 6) and is thus intermediate between the magmatic and the sedimentary values, suggesting that mixing between magmatic and sedimentary carbon may have occurred.

$\delta^{13}C$ of CO_2 in fluid inclusions from one sample of stage II quartz was –9.5‰. Lyon and Hulston (1984) reported $\delta^{13}C_{CO_2}$ values from Broadlands-Ohaaki, New Zealand, of –6.9‰ to –9.1‰ and they interpreted these values to represent magmatic carbon. Only one sample was analyzed for $\delta^{13}C_{CO_2}$, but the carbonate isotopic composition of stage II carbonates is consistent with the fractionation between CO_2 and carbonate (~6‰ for siderite at 150°C; Hoefs, 1997; Porgera stage II carbonates are Ca-Fe-Mg carbonates). The predicted $\delta^{13}C$ of Fe-rich carbonate precipitating from a fluid with $\delta^{13}C_{CO_2}$ of –9.5‰ is –3.5‰, which is similar to the analyzed average value of –2.7‰.

Sulfur

The variable $\delta^{34}S$ values for pyrite from the North Zone suggest that isotopic equilibrium between H_2S in the hydrothermal fluid and pyrite was not reached, which is consistent with a short-lived, dynamic hydrothermal system (Ohmoto and Rye, 1979; Ronacher et al., 2001). The negative $\delta^{34}S$ values for pyrite may be due to a change in the redox condition of the hydrothermal fluid (Ohmoto and Rye, 1979). For example, oxidation accompanying boiling may result in formation of sulfides with negative $\delta^{34}S$ values from heavier sulfur. The sedimentary host rocks exhibit positive $\delta^{34}S$ values (2.1‰ and 5.9 ‰) except for the altered mudstone (–12.7‰) indicating a significant change in either the S source or the oxidation state of S in altered relative to unaltered mudstones.

$\delta^{34}S$ values of late anhydrite (12.4‰ to 17.5‰) are similar to the sulfur isotopic values of sulfate in seawater suggesting that evolved seawater descending in faults during the waning stages of the hydrothermal system could have caused the formation of the late anhydrite.

Observational constraints on fluid sources and hydrothermal processes

The fluid inclusions in stage II quartz provide evidence for two fluids exhibiting different apparent salinities and possible explanations for this bimodality are provided below. Furthermore, the analytical data described above are used to constrain the sources of these two fluids. These data and possible hydrothermal processes that the fluids underwent to form the stage II veins are examined below.

Bimodal salinity distribution

Various possibilities may explain the bimodal salinity distribution observed in some samples: (1) The high apparent salinity fluid may have evolved to a lower apparent salinity fluid with time, for example by boiling thereby degassing CO_2 that could be responsible for the relatively high initial apparent salinity. However, the CO_2 corrected high salinity values are still higher than the low salinity values, and thus, this option does not appear to explain the difference in salinities.

(2) Two fluids of different salinities but similar Th had access to the veins at different times during the evolution of the hydrothermal system. The higher salinity fluid could have been a deep fluid that had cooled upon ascent, whereas the lower salinity fluid may have been a formation water at the ambient temperature at 2.0-2.5 km depth; at a normal geothermal gradient of 30°C/km, the temperature at 2.5 km would have been only 75°C. However the formation water appears to have been ~150° at this depth, suggesting a geothermal gradient of ~50°C/km. Such a gradient may be realistic for the aureole of a shallow-level intrusive complex. Alternatively, Richards and Kerrich (1993) suggested that both fluids sources were deep.

(3) The high salinity fluid could have been variably diluted by a lower salinity fluid of a similar temperature. The diluting solution may have been hosted by the surrounding sedimentary rocks as noted above. Option (3) would require the presence of a range of apparent salinities as observed in a minority of samples. The fact that a continuous salinity trend is present in at least some of the samples suggests that this process may have occurred locally.

Hence, option (2) appears to be the simplest explanation for the bimodal salinity pattern. This explanation is further emphasized by the observation that the low salinity inclusions occur towards the vein center whereas the high salinity inclusions cluster near the vein edge which indicates that, in these samples, the two fluids had access to the vein at different times.

Observations indicating boiling

The three-phase inclusions containing liquid CO_2, CO_2 vapor, and liquid H_2O are interpreted to have been trapped heterogeneously during boiling because final total homogenization (Th_{tot}) occurred to the vapor in some and to the liquid phase in others; Th_{tot} of some of the inclusions could not be measured because of decrepitation, and where it could be measured, Th_{tot} exceeded Th of the liquid-rich inclusions by more than 120°C. Such three-phase, CO_2-rich inclusions appear to be rare in epithermal deposits, although they were described from the geothermal fields of Tuscany by Belkin et al. (1985). Thompson et al. (1985) reported high CO_2 contents in fluid inclusions from the Cripple Creek District, Nevada, as did Saunders (1986) from the Bessie G deposit, Colorado. However, these authors did not quantify the CO_2 concentration in the fluid nor did they report the presence of CH_4 or N_2. Sawkins et al. (1979) analyzed fluid inclusion gases from the epithermal gold deposits in the Baguio district, Philippines, and determined CO_2 concentration between 0.06 and 0.73 mole %, and higher CO_2 contents in epithermal fluids were reported only rarely (e.g., Casadevall and Ohmoto, 1977). Spry et al. (1996) reported 3-phase inclusions from the Golden Sunlight gold-silver telluride and molybdenum porphyry deposit, Montana, but in this case the CO_2-rich inclusions occur in the porphyry-type Mo mineralization rather than in the telluride mineralization. The distribution of CO_2-rich fluid inclusions suggest that hydrothermal systems in alkalic rocks are richer in CO_2 than are systems in calc-alkaline rocks (Mutschler and Mooney, 1993; Richards, 1995; Jensen and Barton, 2000).

The importance of CO_2 in increasing the pressure at which boiling occurs was stressed by Barton and Chou (1993) who found that even small, undetected concentrations of CO_2 can significantly increase the depth of boiling, and can thus have

an impact on the depth of epithermal-type ore deposition. Wilkinson (2001) calculated boiling point curves for H_2O-NaCl-CO_2 fluids of various CO_2 concentrations and plotted them against depth. These diagrams suggest that the amount of CO_2 measured in fluid inclusions from Porgera may not have been sufficient in itself for boiling to have occurred at the estimated depth of 2.0 to 2.5 km and temperature of ore deposition (~160°C) at Porgera. However, other highly volatile gases such as CH_4 and N_2 occur in the inclusion fluid, and these components have an even greater effect than CO_2 in deepening the depth of boiling because of their greater volatility (Price, 1981; Duan et al., 1992). Duan et al. (1992) plotted a CO_2-CH_4 solubility in a 5 wt % NaCl fluid at 149°C and 345 bar from the data of Price (1981), and showed that CH_4 decreases the solubility of CO_2 significantly. Richards et al. (1997) superimposed the Porgera CH_4 and CO_2 data (from the Roamane Fault Zone) on Duan et al.'s (1992) curve (the P-T-salinity conditions of Duan et al.'s (1992) model resemble the conditions at Porgera), and showed that most of the data points fall close to the curve, suggesting that the Porgera fluids may have been saturated with gas (Fig. 4-12). We added the new gas data from the North Zone to Richards et al.'s (1997) plot, and most of the gas data from the North Zone (circles) fall slightly above Duan et al.'s (1992) CO_2-CH_4 solubility curve, which suggests that the conditions at which the saturation curve was modeled may not be correct for the North Zone, whereas they may be suitable for the Roamane Fault Zone. Higher pressures may have prevailed in the North Zone where boiling was rare.

Richards and Kerrich (1993) suggested that the breccias observed dominantly in the Roamane Fault Zone indicated that boiling occurred in this area. In addition, they interpreted the fine-grained silica margins that they observed in stage II veins from the Roamane Fault Zone as having formed during rapid precipitation due to boiling.

Observations indicating fluid mixing

Three samples from the North Zone (P98-611, P98-1164, P98-145) exhibit a continuous salinity trend from ~4.5‰ to ~10.0‰ suggesting *in situ* fluid mixing between a high and a low salinity fluid in these samples. In the five other samples where two fluids were observed (P98-120, P98-1537, P98-178, P98-197, P98-231), the

salinity trend was not continuous but bimodal. Hence, *in situ* mixing cannot be inferred in these samples.

Observations indicating fluid source(s)

Figure 4-13 shows a Br^-/Cl^- versus I^-/Cl^- diagram with data for Porgera from Richards et al. (1997; I^- was not determined in the present study) and for seawater, Broadlands and Wairakei, New Zealand, and Yellowstone from Böhlke and Irwin (1992). Br^-/Cl^- of most samples from Porgera are similar to Br^-/Cl^- for geothermal waters from Broadlands and Wairakei as well as to seawater, but they exhibit much higher I^-/Cl^- ratios than seawater, and higher I^-/Cl^- ratios than the New Zealand geothermal waters. Böhlke and Irwin (1992) attributed the high I^-/Cl^- values (up to $\sim 200 \times 10^{-6}$) in some waters to reaction with organic-rich material, and Kendrick et al. (2001) attributed the I^-/Cl^- values of 121×10^{-6} to mixing of magmatic water with a sedimentary formation water. Such an explanation may also apply for Porgera.

Br^-/Cl^- of seawater (1.5×10^{-3}) falls within the range of Br^-/Cl^- of Porgera fluid (average $1.3 \pm 0.3 \times 10^{-3}$) which may indicate a contribution from a connate seawater because the sedimentary rocks that surround the PIC are Cretaceous to Tertiary marine shelf sediments (Davies, 1983). Alternatively, the Br^-/Cl^- could be a result of interaction of a fluid with shales; Br^-/Cl^- of shales analyzed by Walter et al. (1989) and Kharaka et al. (1977) range from 0.9 to 2.6, and the Porgera values fall within this range.

CH_4 and N_2 concentrations in the Porgera fluid (0.0225 to 0.1226 mole %; 0.0094 to 0.1375 mole % respectively) appear to be high relative to, for example, the Acupan deposit, Philippines (which range from 0.0002 to 0.0100 mole% CH_4, and from 0.0096 and 0.0724 mole % N_2; Sawkins et al., 1979), and relative to the Ladolam deposit, Lihir Island, Papua New Guinea (which contain average values of 0.013 mole% CH_4 and 0.029 mole% N_2; Müller et al., 2002). A potential source of CH_4 and N_2 is a fluid that equilibrated with the organic-rich sedimentary rocks into which the Porgera Intrusive Complex was emplaced. Richards et al. (1997) showed that CH_4 was

critical for boiling to occur under the pressure and temperature conditions during stage II vein formation.

$\delta^{13}C$ of CO_2 in fluid inclusions from one sample of stage II quartz is –9.5‰, and this value is broadly similar to Lyon and Hulston's (1984) values of magmatic CO_2 from Broadlands-Ohaaki, New Zealand, of –6.9‰ to –9.1‰. Alternatively, the slightly lower value for the Porgera sample may be due to a contribution from CO_2 derived from pyrolysis or hydrolysis of organic matter or graphite (according to the reaction $2C + 2 H_2O \rightarrow CO_2 + CH_4$; Ohmoto and Rye, 1979). Given that the average $\delta^{13}C_{org}$ of the Porgera shales is -20.7 ± 2.2‰ (n = 6) and that the expected fractionation between graphite and CO_2 at temperatures below 300°C is between 12‰ and 14‰, the analyzed $\delta^{13}C_{CO_2}$ value of – 9.5‰ could reflect an organic origin if equilibrium were established.

NH_4^+ concentrations in the Porgera inclusion fluids are high (up to 61 mmoles/kg) relative to waters from geothermal systems: e.g., Fushime, Japan, 0.1 to 1.0 mmoles/kg (Akaku et al., 1991); Wairakei, New Zealand, 0.05 mmoles/kg (White et al., 1963). The Porgera ammonium concentrations are also high relative to brines, such as Searles Brine Lake, California (1mmole; White et al., 1963). Slightly higher values were recorded from sedimentary formation waters (2-4 mmoles/kg; Merino, 1975), and even higher values were detected in hydrothermal solutions from the Guayamas Basin, Gulf of California, where Von Damm et al. (1985b) found NH_4^+ concentrations of up to 15.6 mmoles/kg. In comparison, solutions from oceanic spreading centers such as the East Pacific Rise contain <0.01 mmoles/kg (Von Damm et al., 1985 a, b; Viets et al., 1996; Cruse and Seewald, 2001). Von Damm et al. (1985b) attributed the higher NH_4^+ concentrations to interaction of the hydrothermal solution with organic sediments in the Guayamas basin. A similar source is likely for the Porgera fluids.

A further indication of interaction of the hydrothermal fluid with the sedimentary country rocks is the presence of higher hydrocarbon species, such as C_2H_4, C_2H_6 (including C_2H_2; see Table 4-3) in the fluid inclusions. Although these species are

present in minor amounts, they are likely of organic origin and are thus useful for tracing fluid sources (Norman et al., 1966; Brathwaite and Faure, 2002).

Organic-rich fluids were observed in fluid inclusions in some samples from the North Zone. DeRonde and Blattner (1988) observed 3-phase inclusions from the Golden Cross epithermal Au-Ag deposit, Waihi, New Zealand, and one of the two immiscible liquids was reported to have been light brown and darkened upon heating, and was interpreted to be organic, originating from organic-rich sediments. DeRonde and Blattner (1988) state that this fluid separated into several parts before coalescing upon heating. Three-phase organic-rich fluid inclusions were also observed in the Lazio geothermal field, Italy, by Belkin et al. (1994), but they did not speculate on the origin of the organic fluid. In the case of Porgera, the organic fluid may have been derived from the organic-rich sedimentary rocks into which the Porgera Intrusive Complex was emplaced and which partly host mineralized veins. The ascending fluid could have interacted with the sedimentary rocks (as suggested by the observation that the organic liquid occurs in some high salinity fluid inclusions), and because the organic fluid also occurs in some low salinity inclusions, the lower salinity fluid must also have been in contact with organic-rich material, and this fluid was likely a formation water.

The variable sulfur isotopic composition of pyrite in the North Zone (−9.4‰ to +6.1‰) indicates that the system was not in sulfur isotopic equilibrium. Richards and Kerrich (1993) explained the negative $\delta^{34}S_{pyrite}$ (−1.6 to −14.0 ‰) values in the Roamane Fault Zone by oxidation of magmatic sulfur due to boiling. The difference in the range of $\delta^{34}S_{pyrite}$ value between the North Zone and the Roamane Fault Zone suggests that the precipitation process operating in the North Zone was either different or only partly the same as in the Roamane Fault Zone, with additional processes operating in the North Zone. The sulfur source for stage II pyrite remains ambiguous, and both magmatic sulfur and sedimentary sulfur may have contributed to the system. Sulfur could have been oxidized (e.g., by boiling) resulting in the negative values observed in the Roamane Fault Zone (Richards and Kerrich, 1993) and partly in the North Zone.

The $\delta^{18}O_{H_2O}$ and δD_{H_2O} graph (Fig. 4-11) shows the North Zone samples ($\delta^{18}O_{H_2O}$ = −1.2 ‰ to 4.1‰) fall between meteoric and magmatic water compositions suggesting that the Porgera hydrothermal fluid contains a magmatic and a meteoric water component. Similarly, the $\delta^{18}O$ values of H_2O calculated from $\delta^{18}O_{carbonate}$ and an estimated Th of 160° using the fractionation equation between ankerite and H_2O of Zheng (1999) range from 2.2‰ to 3.6‰. Figure 4-11 also shows two calculated isotopic exchange paths between igneous rocks from the PIC (calculated $\delta^{18}O_{H_2O}$ ~ 8.5‰, δD_{H_2O} = −55‰; Richards and Kerrich 1993) and two meteoric water compositions ($\delta^{18}O_{H_2O}$ ~ −7‰, δD_{H_2O} = −50‰; $\delta^{18}O_{H_2O}$ −10‰, δD_{H_2O} = −70‰). Samples from the North Zone differ somewhat from samples from the Roamane Fault Zone in terms of their $\delta^{18}O_{H_2O}$ and δD_{H_2O} composition: the Roamane Fault Zone samples tend to have higher values for $\delta^{18}O_{H_2O}$ and δD_{H_2O}, which may indicate different ratios of magmatic versus meteoric water in the two areas.

Richards et al. (1991) analyzed the lead isotopic compositions of igneous rocks (PIC), sedimentary host rocks of the Chim and Om Formations, and of gold and sulfides of stage I and II mineralization. They found that the lead isotopic composition of gold and sulfides falls between the lead isotopic compositions of the igneous and sedimentary rocks and concluded tentatively that the hydrothermal minerals formed from a mixture of Chim Formation, Om Formation, and igneous lead.

In summary, the analyzed fluid chemistry and the observed salinity distributions suggest that two distinct fluids were involved in the hydrothermal system. One end member (salinity of ~6 equiv. wt % NaCl, Th ≈ 160°C) may have been a magmatically derived fluid ascending from depth, whereas the second fluid (salinity of ~3 equiv. wt % NaCl, Th ≈ 150°C) could have been groundwater hosted by the country rock surrounding the Porgera Intrusive Complex. These two fluids appear locally to have mixed at the level of vein formation as suggested by Th-salinity plots of samples P98-1164 and P99-145, but in other samples (e.g., P98-1537 and P99-231) the fluid inclusion record shows no evidence for in situ mixing. In another group of samples (e.g., P98-1576 and P99-066C), the high salinity fluid was undergoing boiling, as

indicated by heterogeneously trapped fluid inclusions. Hence, it appears that both processes, boiling and fluid mixing, were involved in vein formation at Porgera. In addition, petrographic observations of gold in pyrite in the wall rock of some veins (Figure 4-4 h; Richards, 1998) indicate that fluid–wall rock reaction may also locally have played a role in gold precipitation.

Numerical Modeling

Numerical modeling was conducted to test the effectiveness of boiling, fluid mixing, fluid-rock reaction, and simple cooling for ore deposition in the North Zone of the Porgera deposit. The goal was to determine the process(es) that could precipitate the assemblage quartz-roscoelite-pyrite-gold, because these are the dominant minerals in ore-bearing veins.

CHILLER geochemical modeling – approach and limitations

The computer program CHILLER (Reed, 1982, 1998) was used to model the formation of stage II veins. CHILLER allows modeling of processes such as boiling, mixing, cooling, and wall rock reaction. The software uses a set of component species (Reed, 1982) to define the chemical composition of the system under investigation. All aqueous species, minerals, and gases in the system are assembled from the component species which are themselves also chemical species in the system. For example, the carbonate ion, CO_3^{2-}, can be assembled from the component species HCO_3^- and H^+:

$$CO_3^{2-} = HCO_3^- - H^+$$

Therefore, the value of the mass of the component species H^+ can be negative, for example in a high-pH solution. The same reasoning applies to species involved in redox reactions such as SO_4^{2-} and HS^-, with negative values of masses of SO_4^{2-} describing relatively reduced systems and negative values of masses of HS^- describing

relatively oxidized systems, respectively. No computational difficulties arise when dealing with negative values of masses of component species (Reed, 1998).

CHILLER sets up mass balance and mass action equations involving all chemical species, and these equations are solved simultaneously by iteration using the thermodynamic database Soltherm (Reed and Palandri, 1998). Thus, the mineral-gas-aqueous assemblage and concentrations of all species are determined, constrained by their thermodynamic properties. Processes such as boiling, cooling, and wall rock reaction are modeled by making stepwise changes in P, T, and composition, with an equilibrium calculation for each step.

Starting solution composition

A set of component species defining a starting solution has to be established. The composition of the inferred high-salinity fluid at Porgera was estimated using gas and ion chromatographic data of fluid inclusions and the mineral paragenesis observed in stage II veins (Table 4-9). Ion data were collected for Cl^-, Na^+, K^+, and NH_4^+, and average representative values of these species were used. The analyses for K^+ range from 0 to 398 mmoles/kg for samples from the North Zone. A value of 30 mmoles/kg was used for the calculation which is approximately what Richards et al. (1997) measured. The latter data do not exhibit as large a range as the data collected in this study. The component species NH_4^+ incorporates all N species, and therefore the gas analysis of N_2 was added to the ion analysis of NH_4^+. The component species HCO_3^- was calculated using the concentration of CO_2 from the gas chromatography. The analyzed CH_4 concentration was included by re-expressing its composition in terms of redox components in the system including a HCO_3^- adjustments to represent the carbon in CH_4 (Reed, 1998). Concentrations of Fe^{2+}, Ca^{2+}, and Mg^{2+} were estimated from near saturation with siderite, calcite, and magnesite, respectively, because Ca-Fe-Mg carbonate was observed in stage II veins. Al^{3+} was determined by saturating the solution with muscovite at 170°C. The pH was adjusted to put the solution in the muscovite stability field and slightly undersaturated with K-feldspar field. Saturation with quartz was used to fix SiO_2, and saturation with pyrite was used to fix the total

sulfur concentration. The fluid was also saturated with gold. Concentrations of other elements (e.g., Zn, Cu, or Pb) were low and poorly constrained, and so were not added to the starting solution.

The temperature of the solution was set at 170°C, corresponding to the highest average fluid inclusion homogenization temperature measured in stage II quartz.

Composition of the mixing solution

To simulate fluid mixing, a separate mixing solution was generated. Sedimentary formation water was chosen as the mixing solution because fluid inclusion and ion chromatographic analysis indicate the involvement of such a fluid (see above). We produce a "formation water" that had equilibrated with the sedimentary rocks that host the Porgera Intrusive complex, i.e. siltstones and mudstones, and minor sandstones that were interpreted to be shelf sediments (Davies, 1983; Gunson et al., 2000). The known composition of a mudstone (Richards, 1990b) was equilibrated with seawater (simplified from Berner and Berner, 1996), and the resulting solution (Table 4-10) mixed with the starting solution.

Assumptions and limitations of the method

The starting fluid composition was partly estimated from gas and ion chromatographic analyses performed on fluid inclusions from stage II vein quartz, and partly from the vein paragenesis (e.g., Cooke and McPhail, 2001; Saunders and Schoenly, 1995). The bulk fluid inclusion samples were taken from quartz overlying the roscoelite-pyrite-gold-quartz band, and therefore, the fluid inclusions may not represent the exact composition of the initial solution from which the ore precipitated because it was trapped after the main ore deposition. Nevertheless, it is the closest approximation available because few workable fluid inclusions occur in the roscoelite band. By including the ore-band mineralogy in the estimation of the composition of the starting solution, we made this solution as realistic as possible.

Roscoelite precipitation cannot be modeled at the present time because thermodynamic data for aqueous V species and V minerals are not included in the Soltherm database. However, we assumed that precipitation of muscovite occurs under

similar conditions as roscoelite because of the chemical similarity of the two micas [$KAl_2(Si_3AlO_{10})(OH)_2$ versus $K(V,Al)_2(Si_3AlO_{10})(OH)_2$]; therefore, muscovite was used as a proxy for roscoelite. In addition, Cameron (1998) modeled the stability of roscoelite and concluded that at 200°C roscoelite was stable between pH values of 4 and 12 and log f_{O_2} values of –35 and –60, thus overlapping the muscovite field.

The starting solution consists of a limited number of species and is thus an approximation of reality. However, all dominant minerals occurring in stage II veins can be modeled with the species included (if muscovite is accepted as an analogue for roscoelite). These species were estimated from analytical and petrographic data, and are therefore based on reliable information.

The program CHILLER computes thermodynamic equilibrium conditions and does not take kinetics into account. Although kinetics are important for some mineral precipitation reaction (e.g., graphite, Cooke and McPhail, 2001) and may be important for gold precipitation (Brown, 1989), the program has proved reliable in predicting mineral assemblages, not only in the geothermal and epithermal environments (Reed and Spycher, 1985; Spycher and Reed, 1989; Saunders and Schoenly, 1995; Simmons and Browne, 2000; Cooke and McPhail, 2001), but also for Carlin-type (Hofstra et al., 1991), MVT (Plumlee et al., 1994), greisen (Halter et al., 1998), VHMS (Reed, 1983) and laterite deposits (Getahun et al., 1992).

Experimental Models

Boiling

Adiabatic boiling was modeled starting at 170°C because the highest average Th observed was 167°±25°C. One kilogram of starting solution was adiabatically boiled from 170°C to 100°C.

Fluid mixing

The temperature of the mixing solution was set at 150°C comparable to the Th values of the low salinity fluid inclusions. In this numerical experiment, 3 kilograms of mixing solution were progressively mixed into 1 kilogram of starting solution at 170°.

Cooling

Simple cooling of the starting solution was modeled from 170°C to 100°.

Fluid—wall-rock reaction

Fluid-rock reaction runs were conducted to test whether this process could play a role as an ore precipitation mechanism, and to see whether the mineral assemblage produced during this process reflected the alteration assemblage observed around the quartz-roscoelite-pyrite-gold veins. This numerical experiment also serves as a test for the accuracy of the starting solution composition.

Fluid—wall-rock reaction was modeled by titrating 10 grams of a dioritic host rock of known composition (Roamane diorite; Richards, 1990a) into 1 kilogram of starting solution.

Modeling Results and Interpretation

Boiling

The mineral assemblage that precipitates upon adiabatic boiling is shown in Figure 4-14a. The assemblage consists of quartz, pyrite, and gold, which all precipitate during the earliest stages of boiling. Microcline forms when a temperature of 140° is reached.

The pH increases from 5.0 at 170°C to 7.5 at 100°C (Figure 4-14 b) due to loss of volatiles such as CO_2 to the vapor phase, according to the reaction:

$$HCO_3^-{}_{(aq)} + H^+{}_{(aq)} = H_2O_{(aq)} + CO_{2(g)}$$

where aq stands for aqueous and g for gaseous (cf. Reed, 1998).

Figure 4-14c shows the ratio of the sums of all oxidized and reduced sulfur species in the system ($\Sigma S^{6+}/\Sigma S^{2-}$), and is illustrative of the redox state of the fluid (Cooke and McPhail, 2001). The fluid becomes oxidized during boiling as reduced species such as H_2S and CH_4 enter the gas phase.

The experiment yields a paragenesis similar to that observed in stage II veins inasmuch as gold, pyrite, and quartz precipitate; however, it lacks muscovite.

Mixing

Figure 4-15 shows the effects of progressively mixing up to 3 kg of formation water at 150°C with 1 kg of starting solution at 170°C. The graph is to be read from left to right. After mixing 1 kg of formation water with the starting solution, the temperature is ~160°C, and after mixing with 3 kilograms of formation water the temperature is 155°C. Mixing results in the early precipitation of muscovite and pyrite, followed later by gold after mixing of 1.4 kg of formation water. The pH changes slightly from 5.0 to 5.2, and the oxidation state of the fluid increases upon mixing with the near-neutral formation water.

The minerals calculated to precipitate upon mixing are observed in the vein assemblage. Quartz, a dominant mineral in most veins, does not form during mixing. Also, gold precipitation is delayed relative to muscovite and pyrite.

Cooling

Simple cooling from 170° to 100°C results in precipitation of quartz, pyrite, muscovite, and gold during the first 5°C of cooling (Fig. 4-16a). Muscovite reacts out and is replaced by kaolinite at a temperature of 120°C which reflects the drop in pH from 5.0 at 170°C to 4.6 at 100°C (Fig. 4-16b). The oxidation state of the fluid increases upon cooling (Fig. 4-16c).

All minerals predicted to precipitate during cooling occur in stage II except kaolinite. Temperatures in the veins do not fall to 120°C, so kaolinite is not expected to precipitate.

Water-rock reaction

The minerals calculated to precipitate early upon reaction of 1 kg of the starting solution with dioritic wall rock include quartz, muscovite, pyrite, siderite, gold, and apatite followed by dolomite. After 5 grams of rock was titrated into the starting solution, ankerite also precipitated, followed by hematite at 7 grams (Fig. 4-17).

The observed alteration assemblage consists of carbonate-sericite-pyrite with minor quartz and gold hosted in pyrite which is similar to the model paragenesis. Hematite, clay minerals, and chlorite are also observed in small amounts in the altered wall rock, and apatite is present as a stable residual phase in the diorite.

Interpretation of modeling results

Modeling of fluid-rock reaction best reproduces the mineral paragenesis observed in the wall-rock alteration and in some of the mineralized veins at Porgera. However, because only a limited amount of wall-rock can interact with the hydrothermal fluid due to shielding of fresh rock by a layer of altered rock, this process, although observed locally, probably played a minor role in ore formation at Porgera.

Boiling precipitates quartz, pyrite, and gold, but muscovite (i.e. roscoelite) does not precipitate. This observation suggests that boiling alone is unlikely to have been responsible for stage II vein formation based on the thermodynamic modeling.

Fluid mixing results in pyrite-muscovite-gold formation, but no quartz is expected to precipitate upon mixing. Hence, this mechanism may account only for roscoelite-pyrite-gold formation. Boiling and mixing were accompanied by cooling which contributed to stage II vein formation. Cooling is very efficient in deposition of quartz, whereas only small amounts of muscovite, pyrite, and gold form upon cooling. Hence, it is likely that the coarse-grained quartz that forms the bulk of some veins was deposited by cooling.

In summary, the modeling results indicate that the individual bands of stage II veins may have formed by different processes, e.g. the roscoelite band formed by mixing or fluid-rock reaction (which form the largest amount of roscoelite of all processes) whereas some of the early quartz formed by boiling and the bulk of the coarse-grained

quartz in the vein centers may have formed by cooling. It is also likely that a combination of these processes, for example boiling and cooling or fluid mixing and cooling, occurred.

Discussion

Both processes, boiling and fluid mixing, have been suggested as ore forming mechanisms at Porgera. Arguments for boiling were based on textural observations of breccias and breccia veins abundant in the Roamane Fault Zone, and on mineralogical observations such as vein margins consisting of fine-grained quartz interpreted to be recrystallized chalcedony (Richards and Kerrich, 1993). Furthermore, vapor-rich fluid inclusions coexisting with liquid-rich inclusions were observed in stage II quartz intergrown with gold in one sample from near the Roamane Fault Zone (Ronacher et al., 2000b). In contrast, Wall et al. (1995) and Cameron et al. (1995) suggested – based on considerations of mobility of V^{3+} versus V^{5+} in a hydrothermal fluid – that precipitation of roscoelite was a result of reduction (rather than oxidation caused by boiling) and that mixing with a reduced fluid was a likely ore formation mechanism (see also Cameron, 1998).

The data on quartz-roscoelite-pyrite-gold veins collected for this study have been used to readdress the question of ore deposition at Porgera. The crucial results from the North Zone are summarized here, and are integrated in a model of ore formation for this zone. The presence of two fluids is indicated by a higher and a lower salinity inclusion group. Vapor-rich fluid inclusions observed in some samples indicate that boiling occurred, at least locally, and in the Roamane Fault Zone a direct link was made between boiling and gold deposition (Ronacher et al., 2000b). In the North Zone samples, vapor-rich fluid inclusions were not observed in quartz intergrown with gold, but their presence in quartz immediately overlying the gold-rich layer nevertheless demonstrates that conditions were favorable for boiling. Organic compounds in the fluid (e.g., C_2H_2, C_2H_4, C_2H_6) and organic-rich liquid in rare fluid inclusions indicate reaction of the fluid with organic-rich sedimentary rocks. Also, the gas and ion

compositions of stage II fluids suggest the involvement of a formation water (e.g., CH_4, N_2; I^-/Cl^-; NH_4, Br^-/Cl^-, presence of higher hydrocarbons and, in rare cases, organic liquid, $\delta^{13}C_{CO_2}$). The carbon isotopic signatures of stage II carbonates (~–2.5‰) are different from the magmatic value of stage I carbonates (~–5‰; Richards and Kerrich, 1993) and suggest carbon contribution from a source other than magmatic water, perhaps the sedimentary rocks. $\delta^{18}O$ and δD data suggest a significant contribution of meteoric water to the hydrothermal fluid (Richards and Kerrich, 1993 and this study). Numerical simulations indicate that the most efficient mechanisms to precipitate quartz are boiling and cooling, whereas muscovite (used as a proxy for roscoelite) is formed most efficiently by fluid-rock reaction and fluid mixing, and gold is more likely formed by boiling and fluid-rock reaction. Finally, petrographic observations showed that gold also occurs in the wall rock adjacent to veins, further suggesting that fluid-rock reaction/wall rock sulfidation played a role in vein formation.

These data indicate disparate processes – vapor-rich fluid inclusions in some samples suggesting boiling, continuous salinity trends on Th-salinity plots of some samples suggesting fluid mixing, gold in the wall rock suggesting fluid-rock reaction as precipitation mechanism – which can be combined and integrated into a model for ore formation at Porgera, because these processes are not mutually exclusive and they can be related to particular samples. For example, boiling can clearly be linked to seven samples (P98-1576, P98-701, P98-1320, P98-611, P99-066C, P99-197, P98-1835) and in these samples quartz is interpreted to have formed by boiling. However, these samples do not cluster in one location in the North Zone, but are spread over the entire depth extension of the high-grade area which indicates that boiling occurred intermittently along the entire North Zone. Likewise, samples that contain roscoelite in the wall-rock also occur over the entire depth of the ore zone and are not restricted to one particular area. Similarly, the three samples that exhibit continuous salinity trends and in which quartz was interpreted to have formed by fluid mixing, do not occur in one location only, although their occurrence has been observed over a depth interval of 100m only (Table 4-2). These observations indicate that boiling, mixing, and fluid-rock reaction, all accompanied by cooling, occurred intermittently along the North Zone.

Furthermore, more than one process was observed to have operated in one samples; for example, vapor-rich fluid inclusions (boiling) and roscoelite in the wall-rock (fluid-rock reaction) were observed in three samples (P98-1576, P98-701, P99-197). Also, sample P98-611 exhibits a continuous salinity trend (suggesting mixing) and vapor-rich fluid inclusions (boiling). These observations further emphasize that more than one process can operate during vein formation and that a combination of processes may have been involved in vein deposition, operating in the same location but at different times forming the individual bands of the quartz-roscoelite-pyrite-gold veins.

Hence, we suggest a model in which fluid, exsolved from the inferred parent pluton at depth, may have interacted with the country rocks, mudstones and siltstones of the Om and Chim Formations (Davies, 1983), and mixed with the fluid hosted by these rocks. As this homogenized/mixed fluid rose to shallower levels, it reacted with the dioritic and gabbroic wall-rocks and started to precipitate a paragenesis similar to the one predicted to form in the fluid-rock experiment. Fractured rock resulting from normal movement along the Roamane Fault may have allowed more formation water to interact with the ascending fluid, and locally, mineral precipitation may have cemented the available open space in the faults which resulted in overpressuring of the fluid, followed by hydrofracturing, decompression, brecciation and boiling (as evidenced by vapor-rich inclusions). Boiling may have been prevalent in the highest grade areas, such as Zone VII, located directly in the Roamane Fault Zone where quartz intergrown with gold contains both liquid and vapor inclusions (Ronacher et al. 2000b). In the North Zone of the footwall diorite, in contrast, where gold occurs partly in thin veinlets intergrown with abundant roscoelite and partly in the wall rock adjacent to thin quartz-roscoelite-pyrite-gold veinlets in addition to breccia veins, fluid-wall rock reaction may have been an additional ore precipitation mechanisms. Locally, fluid mixing may have been the dominant ore deposition mechanism as indicated by the fluid inclusion salinity trends observed in some samples from the North Zone. Given the size of the Porgera deposit, it is not surprising that more than one mechanism was responsible for ore formation. In this study, we presented a multi-process model that explains field observations, analytical data, and modeling results.

Porgera in the context of alkalic rock-related gold deposits

Gold deposits associated with alkalic rocks have been the topic of a number of reviews (e.g., Mutschler and Mooney, 1993; Richards, 1995; Jensen and Barton, 2000; Müller and Groves, 2002), in which the similarity between these deposits was stressed. In contrast, Sillitoe (2002) underlined the uniqueness of deposits like Porgera, Papua New Guinea, Emperor, Fiji, or Cripple Creek, Nevada. The following section is not intended to reiterate what the above authors have already stated, but to (1) compare depositional mechanisms inferred to have played a role at Porgera with the ore forming processes in other alkalic systems; and (2) comment on the potential uniqueness of Porgera and the implications for exploration.

Common depositional mechanisms

A variety of depositional processes was suggested for alkalic-rock related, low-temperature vein deposits (Jensen and Barton, 2000), including fluid phase separation, fluid mixing, cooling, and fluid—wall-rock reaction. For example, Ahmad et al. (1987) suggested based on the fluid inclusion record that ore deposition at the Emperor mine, Fiji, was dominantly due to phase separation, whereas Kwak (1990) argued that cooling due to fluid mixing and wall-rock reaction were responsible for ore formation in the same deposit. Kwak (1990) also based his argument on microthermometric observations of samples from the area of the Emperor mine that he studied. Poliquin and Simmons (1998), in another study on the Emperor mine, obtained similar results as Ahmad et al. (1987) and concluded that phase separation was involved in ore formation but that phase separation over a large vertical interval was "a puzzling feature of the ore-forming hydrothermal conditions of this deposit".

Other examples are the Cripple Creek deposit, Nevada, for which Thompson et al. (1985) suggested that cooling may have been the dominant ore deposition mechanism. In addition, Jensen and Barton (2000) stress that, locally, there is evidence for fluid—wall-rock reaction at Cripple Creek. Zhang and Spry (1994) and Spry and Thieben (1998) suggested for the Gies gold-silver telluride deposit, Montana, that

mixing was involved in ore deposition based on isotopic and microthermometric observations (except for the bonanza ore zones that may have formed by phase separation; P. Spry, pers. commun., 2002). Cooke and McPhail (2001) concluded for the Acupan deposit, Baguio district, Philippines, that phase separation, fluid mixing, cooling, and fluid—wall-rock reaction all contributed to vein formation at Acupan and that these processes may have occurred simultaneously. Cooke and McPhail (2001) based their conclusions on detailed petrographic, microthermometric, and isotopic studies of the deposit, as well as thermodynamic reaction path modeling (Cooke and Bloom, 1990; Cooke et al., 1996).

Hence it appears that original models of ore deposition in the epithermal environment that stressed the predominance of phase separation over alternative precipitation mechanisms (e.g., Drummond and Ohmoto, 1985) can be expanded and added to. Bogie and Lawless (1997, 1998) pointed out that there may even be two distinct types of epithermal deposit distinguished by the ore deposition mechanism, with phase separation being dominant in deposits characterized by chalcedony, adularia, pyrite, and a continuous high-grade zone, whereas mixing may have been prevalent in deposits of smaller vertical extent containing quartz, barite, pyrargyrite, and electrum.

In summary, the available evidence for low-temperature deposits associated with alkalic rocks suggests that a variety of ore deposition mechanisms can be invoked to explain ore formation in these deposits. Ore formation at Porgera is no exception: a comparison of the findings of our study with the above evidence from the literature further underlines that epithermal-type systems are rapidly evolving and dynamic (Cooke and McPhail, 2001), and a variety of depositional mechanisms are only a logical consequence of the fast-changing nature of these systems.

Is Porgera unique? Implications for exploration for "Porgera-type" deposits

Although frequently compared to other gold deposits associated with alkalic rocks (Richards, 1995; Ronacher et al., 1999), Sillitoe (2002) stressed the uniqueness of Porgera. Some characteristics of the deposit appear to be unique, for example the inferred depth of ore formation of ~2 to ~2.5 km. In addition, the host rocks of the PIC

consist of sedimentary rocks dominantly of the Chim Formation (siltstones and mudstones; Davies, 1983), and, perhaps more importantly, the PIC is underlain by carbonaceous mudstones and siltstones of the Om Formation (Davies, 1983), which is source of oil and gas (Davies, 1983). Hence, fluids exsolved from the inferred parent pluton at ~6 km depth (Richards, 1990a) passed through ~4 km of hydrocarbon-rich sedimentary rocks. The interaction with these rocks is argued to have enriched the fluids in CH_4 and N_2, which is the reason why these fluids were able to phase separate at depths of ~2.0 to 2.5 km (Figure 4-11). It remains unclear, however, whether the interaction with organic-rich sedimentary rocks had consequences other than enhancing phase separation. For example, it is possible that organo-metallic complexes played a role in transport of not only precious metals but also Al or Na (Shock, 2000; Giże, 2000).

The inferred paleodepth of ore formation at Porgera indicates that exploration for similar deposits could extend to depths greater than what was traditionally assumed to be the epithermal environment, especially in the vicinity of carbonaceous sedimentary rocks and CO_2-rich alkalic rocks. Likewise, areas where some degree of erosion was documented may still be explorable for epithermal-type deposits.

Porgera may be a giant deposit because of the interplay of various parameters: (1) Tectonic setting prone to yield alkalic magmatism (i.e., back-arc environment, post subduction or extensional setting; Richards, 1995; Sillitoe, 2002); (2) structural setting favorable for magma ascent (e.g., intersection of deep crustal structures; Corbett et al., 1995); (3) structural setting favorable for focused ore precipitation (e.g., Roamane Fault and its splays); (4) conditions favorable for phase separation, possibly due to interaction with the host sedimentary rocks; (5) conditions favorable for fluid mixing due to availability of mixing solutions and dilational zones were mixing could take place in addition to cooling. Lack of only one or more of these parameters may still result in formation of an ore deposit, but it is unlikely that a giant deposit would form. Hence, all of the above criteria have to be met in order for a giant "Porgera-type deposit" to form (see also Richards, 1997; Sillitoe, 1997).

Conclusions

Petrographic observations, fluid inclusion microthermometry, gas and ion chromatography, and stable isotopic analysis on high-grade quartz-roscoelite-pyrite-gold veins from the Porgera gold deposit, Papua New Guinea, indicate that more than one precipitation mechanism was responsible for ore formation at Porgera. Boiling may have been dominant in the highest-grade major fault hosted areas, whereas mixing of a magmatic fluid with a sedimentary formation water and fluid—wall rock reaction may have been more important in smaller splays of the main fault. All these processes were accompanied by cooling. These conclusions are corroborated by results of numerical simulations of mineral deposition using the programs CHILLER. The simulations suggest that gold is most efficiently precipitated by boiling and fluid-rock reaction, muscovite (used as an approximation for roscoelite) is most efficiently formed by fluid mixing, whereas quartz is more readily formed by boiling or cooling.

References

Ahmad, M, Solomon, M., and Walshe, J.L., 1987, Mineralogical and geochemical studies of the emperor gold telluride deposit, Fiji: Econ. Geol., v. 82, p. 345-370.

Akaku, K., Reen, M.H., Yagi, M., Kai, K., and Yasuda, Y., 1991, Chemical and physical processes occurring in the Fushime geothermal system, Kyushu, Japan: Geochem. Journal, v. 25, p. 315-333.

Arnorsson, S., Gunnlauggson, E.,a nd Svavarsson, H., 1983, The chemistry of geothermal waters in Iceland II. Mineral equilibria and independent variables controlling water composition: Geochim. Cosmochim. Acta, v. 47, p. 547-566.

Baron, P., and Chou, I-Ming, 1993, Refinement of the Evaluation of the Role of CO_2 in Modifying Estimates of the Pressure of Epithermal Mineralization: Econ. Geol., v. 88, p. 873-884.

Belkin, H. E., Cavarretta, G., and Tecce, F., 1994, Lazio geothermal fields, *in* De Vivo, B., and Frezzotti, M.L., eds., Fluid inclusions in minerals: Methods and applications, Short Course of the Intl. Mineral. Assoc. Working Group "Inclusions in Minerals", Virginia Tech, p. 327-343.

Belkin, H., De Vivo, B., Gianelli, G., and Lattanzi, P., 1985, Fluid inclusions from the geothermal fields of Tuscani, Italy: Geothermics, v. 14, p. 59-72.

Berner, E.K., and Berner R.A., 1996, Global Environment, Water, Air and Geochemical Cycles: Prentice Hall, 376p.

Bodnar, R.J., 1993, Revised equation and table for determining the freezing point depression of H_2O-NaCl solutions: Geochim. Cosmochim. Acta, v. 57, p. 683-8-684.

Bodnar, R.J., Reynolds, T.J., and Kuehn, C.A., 1985, Fluid-inclusion systematics in epithermal systems: Rev. Econ. Geol., v. 2, p. 73–97.

Bogie, I., and Lawless, J.V., 1997, North Island epithermal gold: Processes of mineralization: New Zealand Minerals and Mining Conference Proceedings 1997, p. 125-132.

Bogie, I., and Lawless, J.V., 1998, Ore shoot targeting by recognition of upflow and outflow, low sulfidation epithermal deposits: Proceedings of the Pacific Rim Congress '99, Australasian Institute of Mining and Metallurgy, p. 649-653.

Böhlke, J.K., and Irwin, J.J., 1992, Laser microprobe analyses or Cl, Br, I, and K in fluid inclusions: Implications for sources of salinity in some ancient hydrothermal fluids: Geochim. Cosmochim. Acta, v. 56, p. 203-225.

Bowers, T.S., 1991, The deposition of gold and other metals: Pressure-induced fluid immiscibility and associated stable isotope signature: Geochim. Cosmochim. Acta, v. 55, p. 2417-1434.

Brathwaite, R.L., and Faure, K, 2002, The Waihi epithermal gold-silver-basemetal sulfide-quartz vein system, New Zealand: Temperature and salinity controls on electrum and sulfide deposition: Econ. Geol., v. 97, p. 269-290.

Bray, C.J., Spooner, E.T.C., and Thomas, A.V., 1991, Fluid inclusion volatile analysis by heated crushing, on-line gas chromatography; applications to Archean fluids: J. Geochem. Exploration, v. 42, p. 167-193.

Brown, K.L., 1986, Gold deposition from geothermal discharges in New Zealand: Econ. Geol., v. 81, p. 979-983.

Brown, K.L., 1989, Kinetics of gold precipitation from experimental hydrothermal sulfide solutions: Econ. Geol. Mon., v. 6, p. 320-327.

Brown, P.E., and Hagemann, S.G., 1994, Macflincor: A computer program for fluid inclusion data reduction and manipulation. In: De Vivo, B. and Frezzotti, M.L., 1994, Fluid inclusions in minerals: Methods and Applications: Short Course Notes, Virginia Polytechinical Institute, p. 231-250.

Cameron, G.H., 1998, The hydrothermal evolution and genesis of the Porgera gold deposit, Papua New Guinea: Unpubl. Ph.D. Thesis, Canberra, Australian National University, 137 p.

Cameron, G.H., Wall, V.J., Walshe, J.L., and Heinrich, C.A., 1995, Gold mineralization at the Porgera gold mine, Papua New Guinea, in response to fluid mixing: Proceedings of the Pacific Rim Congress '95, Australian Institute of Mining and Mettalurgy, p. 99-100.

Casadevall, T., and Ohmoto, H., 1977, Sunnyside mine, Eureka, mining district, San Juan County, Colorado: Geochemistry of gold and base metal ore deposition in a volcanic environment: Econ. Geol, v. 72, p. 1285-1320.

Channer, D.M.DeR., and Spooner, E.T.C., 1992, Analysis of fluid inclusion leachates from quartz by ion chromatography: Geochim. Cosmochim. Acta, v. 56, p. 249-259.

Channer, D.M.DeR., and Spooner, E.T.C., 1994, Combined gas and ion chromatographic analysis of fluid inclusions: Application to Archean granite pegmatite and gold-quartz vein fluids: Geochim. Cosmochim. Acta, v. 58, p. 1101-1118.

Channer, D.M.DeR., and Spooner, E.T.C., 1999, Integrated cation-anion/volatile fluid inclusion analysis by gas and ion chromatography; methodology and examples: Chem. Geol., v. 154, p. 59-82.

Clayton, R.N, and Mayeda, T.K., 1963, The use of bromine petafluoride in the extraction of oxygen form oxides and silicates for isotopic analyses: Geochim. Cosmochim. Acta, v. 27, p. 43-52.

Clayton, R.N., O'Neil, J.R., and Mayeda, T.K., 1972, Oxygen isotope exchange between quartz and water: J. Geophys. Research, v. 77, p. 3057-3067.

Cline, J.S., Bodnar, R.J., Rimstidt, J.D., 1992, Numerical simulation of fluid flow and silica transport and deposition in boiling hydrothermal solutions: application to epithermal gold deposits: J. Geophysical Research, v. 97, p. 9085-9103.

Cooke, D.R, and McPhail, D.C., 2001, Epithermal Au-Ag-Te mineralization, Acupan, Baguio District, Philippines; Numerical simulations of mineral deposition: Econ. Geol., v. 96, p. 109-132.

Cooke, D.R., and Bloom, M.S., 1990, Epithermal and subjacent porphyry mineralization, Acupan, Baguio district, Philippines: A fluid inclusion and paragenetic study: J. Geochem. Exploration, v. 35, p. 297-340.

Cooke, D.R., and Simmons, S.F., 2000, Characteristics and genesis of epithermal gold deposits: Reviews Econ. Geol., v. 13, p. 221-244.

Cooke, D.R., McPhail, D.C., and Bloom, M.S., 1996, Epithermal gold mineralization, Acupan, Baguio district, Philippines: Geology, mineralization, alteration, and

the thermochemical environment of ore deposition: Econ. Geol., v. 91, p. 243-272.

Corbett, G., Leach, T., Stewart, R., and Fulton, B., 1995, The Porgera gold deposit: Structure, Alteration and Mineralisation: Proceedings of the Pacific Rim Congress '95, Australasian Institute of Mining and Metallurgy, p. 151-156.

Cruse, A.M., and Seewald, J.S., 2001, Metal mobility in sediment-covered ridge-crest hydrothermal systems: Experimental and theoretical constraints: Geochim. Cosmochim. Acta, v. 65, p. 3233-3247.

Davies, H.L., 1893, Wabag, Papua New Guinea, 1:250 000 Geological Series – Explanatory Notes, Port Moresby, Geological Survey of Papua New Guinea, 84 p.

Deines, P., Langmuir, D., and Harmon, R.S., 1974, Stable carbon isotope ratios and the existence of a gas phase in the evolution of carbonate ground waters: Geochim. Cosmochim. Acta, v. 38, pp. 1147-1164.

DeRonde, C.E.J., and Blattner, P., 1988, Hydrothermal alteration, stable isotopes, and fluid inclusions of the Golden Cross epithermal gold-silver deposit, Waihi, New Zealand: Econ. Geol, v. 83, p. 895-917.

Drummond, S.E., and Ohmoto, H., 1985, Chemical evolution and mineral deposition in boiling hydrothermal systems: Econ. Geol., v. 80, p. 126-147.

Duan, Z., Møller, N., Weare, J.H., 1992, An equation of state for the CH_4-CO_2-H_2O system: II. Mixtures from 50 to 1000°C and 0 to 1000 bar: Geochim. Cosmochim. Acta, v. 56, p. 2619-2631.

Field, C.W., and Fifarek, R.H., 1985, Light stable-isotope systematics in the epithermal environment: Reviews in Economic Geology, v. 2, p. 99-128.

Fleming, A.W., Handley, G.A., Williams, A.L., Hills, A.L., and Corbett, G.J, 1986, The Porgera gold deposit, Papua New Guinea: Econ. Geol., v. 81, p. 660-680.

Fournier, R.O., 1985, Silica minerals as indicators of conditions during gold precipitation: USGS Bulletin 1646, p. 15-26.

Getahun, A., Reed, M.H., Retallack, G.J., 1992, A numerical simulation of the chemical development of laterite and china clay: Abstracts with Programs – Geol. Soc. America, Cordilleran Section Annual Meeting, v. 24, p. 27.

Gunson, M., Hall, G., Johnston, M., 2000, Foraminiferal coloration index as a guide to hydrothermal gradients around the Porgera intrusive complex, Papua New Guinea: Econ. Geol., v. 95, p. 271-282.

Halter, W.E., Williams-Jones, A.E., and Kontak, D.J., 1998, Modeling fluid-rock interaction during greisenization at the East Kemptville tin deposit: Chem. Geol., v. 150, p. 1-17.

Handley, G.A., and Bradshaw, P.M.D., 1986, The Porgera gold deposit, Papua New Guinea, *in* MacDonald, A.J., ed., Gold '86: International Symposium on the Geology of Gold Deposits: Willowdale, Ontario, Konsult International, p. 416-424.

Handley, G.A., and Henry, D.D., 1990, Porgera gold deposit, *in* Huges, F.E., ed., Geology of the mineral deposits of Australia and Papua New Guinea: Melbourne, The Australian Institute of Mining and Metallurgy, p. 1717-1724.

Hedenquist, J.W., and Henley, R.W., 1985, The importance of CO_2 on freezing point measurements of fluid inclusions: Evidence from active geothermal systems

and implications for epithermal ore deposition: Econ. Geol., v. 80, p. 1379-1406.
Hedenquist, J.W., Arribas, A., and Gonzalez-Urien, E., 2000, Exploration for epithermal deposits: Reviews in Economic Geology, v. 13, p. 245-277.
Henley, R.W., 1982, Metals in hydrothermal fluids: Rev. Econ. Geol., v. 1, p. 115-128.
Hill, K.C., and Gleadow, A.J.W., 1989, Uplift and thermal history of the Papuan Fold Belt, Papua New Guinea: Austalian J. of Earth Sciences, v. 36, p. 515-539.
Hill, K.C., and Raza, A., 1999, Arc-continent collision in Papua New Guinea: Constraints from fission track thermochronology: Tectonics, v. 18. p. 950-966.
Hoefs, J., 1997, Stable Isotope Geochemistry: Berlin, Springer, 201 p.
Hofstra, A.H., Leventhal, J.S., Northrop, H.R., Landis, G.P., Rye, R.O., Birak, D.J., and Dahl, A.R., 1991, Genesis of sediment-hosted disseminated-gold deposits by fluid mixing and sulfidization: chemical-reaction-path modeling of ore-depositional processes documented in the Jerritt Canyon District, Nevada: Geology, v. 19, p. 36-40.
Jensen, E.P., and Barton, M.D., 2000, Gold deposits related to alkaline magmatism: Reviews in Econ. Geol., v. 13, p. 279-314.
Kendrick, M.A., Burgess, R., Pattrick, R.A.D., and Turner, A., 2001, Fluid inclusion noble gas and halogen evidence on the origin of Cu-Porphyry mineralising fluids: Geochim. Cosmochim. Acta, v. 65, p. 2651-2668.
Kharaka, Y., Callender, E., and Carohters, W., 1977, Geochemistry of geopressured geothermal waters from the Texas Gold Coast: Geopressured Geothermal Energy Conference Porceedings, vol. 3, p. Gl.121-Gl.165.
Kontak, D.J., and Kerrich, R., 1997, An isotopic (C, O, Sr) study of the vein gold deposit in the Mguma Terrane, Nova Scotia: Implication for source and reservoirs: Econ. Geol., v. 92, p. 161-180.
Kwak, T.A.P., 1990, Geochemical and temperture controls on ore mineralization at the Emperor gold mine, Vatukoula, Fiji: J. Geochem. Exploration, v. 36, p. 297-337.
Le Bas, M.J., Le Maitre, R.W., Streckeisen, A., and Zanettin, B., 1986, A chemical classification of volcanic rocks based on the total alkali-silica diagram: J. Petrol., v. 27, p. 745-750.
Lyon, G.L., and Hulston, J.R., 1984, Carbon and hydrogen isotopic composition of New Zealand geothermal gases: Geochim. Cosmochim. Acta, v. 48, p. 1161-1171.
Müller, D., and Groves, D.I., 2000, Potassic igneous rocks and associated gold-copper mineralization, 3rd ed., Springer, Berlin.
Müller, D., Kaminski, K., Uhlig, S., Graupner, T., Herzig, P.M., and Hunt, S., 2002, The transition from porphyry- to epithermal-style gold mineralization at Ladolam, Lihir island, Papua New Guinea: a reconnaissance study: Mineralium Deposita, v. 37, p. 61-74.
Mutschler, F.E., and Mooney, T.C., 1993, Precious-metal deposits related to alkalic igneous rocks: Provisional classification, grade-tonnage data and exploration frontiers: Geological Association of Canada Special Paper, v. 40, p. 479-520.
Norman, D.I., Moore, J.N., Yonaka, B., and Musgrave, J., 1966, Gaseous species in fluid inclusions: a tracer of fluids and indicator of fluid processes: Proceedings

of the 21st Workshop on Geothermal Reservoir Engineering, Stanford University, Stanford, California, p. 233-240).

Ohmoto, H. and Rye, R.O., 1979, Isotopes of Sulfur and Carbon: Geochemistry of Hydrothermal Ore Deposits, 2rd edition: John Wiley & Sons, p. 509-567.

Ohmoto, H., and Goldhaber, M.B., 1997, Sulfur and Carbon Isotopes: Geochemistry of Hydrothermal Ore Deposits, 3rd edition: John Wiley & Sons, p. 517-612.

Plumlee, G.S., Leach, D.L., Hofstra, A.H., Landis, G.P., Rowan, E.L., and Viets, J.G., 1994, Chemical reaction path modleing of ore deposition in mississippi valey-type Pb-Zn deposits of the Ozark region, U.S. Midcontinent: Econ. Geol., v. 89, p. 1361-1383.

Poliquin, M.J., and Simmons, S.F., 1998, Mineralogical and fluid inclusion studies of the R-1 Zone, Emperor gold mine, Fiji: Geological Society of America Program with Abstracts, vol. 30, p. A302.

Potter, R.W. II, and Brown, D.L., 1977, The volumetric properties of aqueous sodium chloride solutions from 0°C to 500°C at pressures up to 2000 bars based on a regression of available data in the literature: U.S. Geol. Survey Bulletin, 1421-C.

Price, L.C., 1981, Methane solubility in brines with application to the geopressured resource: Proceedings of the 5th Geopressured and Geothermal Energy Conference, Louisiana State University, Baton Rouge, p. 205-214.

Ramboz, C., Pichavant, M, and Weisbrod, A., 1982, Fluid immiscibility in natural processes: Use and misuse of fluid inclusion data II. Interpretation of fluid inclusion data in terms of immiscibility: Chem. Geol., v. 37, p. 29-48.

Reed, M. H., 1983, Seawater-basalt reaction and the origin of greenstones and related ore deposits: Econ. Geol., v. 78, p. 466-485.

Reed, M.H., 1982, Calculation of multicomponent chemical equilibria and reaction process in systems involving minerals, gases and an aqueous phase: Geochim. Cosmochim. Acta., v. 46, p. 513-528.

Reed, M.H., 1998, Calculation of simultaneous chemical equilibria in aqueous-mineral-gas systems and its application to modeling hydrothermal processes: Rev. Econ. Geol., v. 10, p. 109-124.

Reed, M.H., and Palandri, J., 1998, SOLTHERM database: A compilation of thermodynamic data from 25° to 300° C for aqueous species, minerals and gases: Unpublished report, Dept. of Geological Sciences, University of Oregon, Eugene, Oregon.

Reed, M.H., and Spycher, N.F., 1984, Calculation of pH and mineral equilibria in hydrothermal waters with application to geothermometry and studies of boiling and dilution: Geochim. Cosmochim. Acta, v. 48, p. 1479-1492.

Reed, M.H., and Spycher, N.F., 1985, Boiling, cooling, and oxidation in epithermal systems: A numerical modeling approach: Rev. Econ. Geol., v. 2, p. 249-272.

Richards, J.P., 1990a, Petrology and geochemistry of alkalic intrusives at the Porgera gold deposit, Papua New Guinea: J. Geochem. Exploration, v. 35, p. 141-199.

Richards, J.P., 1990b, The Porgera gold deposit, Papua New Guinea: Geology, Geochemistry and Geochronology: Unpublished Ph.D. Thesis, Canberrra, Australian National University, 106 p.

Richards, J.P., 1995, Alkalic-type epithermal gold deposit: a review: Mineralogical Association of Canada Short Course Series, v. 23, p. 367-400.

Richards, J.P., 1997, Controls on scale of Porgera-type porphyry/epithermal gold deposits associated with mafic, alkalic magmatism: Transaction of the Institution of Mining and Metallurgy (Section B), v. 106, p. B1-B8.

Richards, J.P., 1998, Porgera '97 drillcore samples: Unpubl. Company Report, Porgera Joint Venture, Porgera, Papua New Guinea, 20 p.

Richards, J.P., and Kerrich, R., 1993, The Porgera gold mine, Papua New Guinea: Magmatic hydrothermal to epithermal evolution of an alkalic-type precious metal deposit: Econ. Geol., v. 88, p. 1017-1052.

Richards, J.P., Bray, C.J., Channer, D.M.DeR., and Spooner, E.T.C., 1997, Fluid chemistry and processes at the Porgera gold deposit, Papua New Guinea: Mineral. Deposita, v. 32, p. 119-132.

Richards, J.P., Chappell, B.W., and McCulloch, M.T., 1990, Intraplate-type magmatism in continent-island-arc collision zone: Porgera intrusive complex, Papua New Guinea: Geology, v. 18, p. 958-961.

Richards, J.P., McCullock, M.T., Chappell, B.W., and Kerrich, R., 1991, Sources of metals in the Porgera gold deposit, Papua New Guinea: Evidence form alteration, isotope, and noble metal geochemistry: Geochim. Cosmochim. Acta, v. 55, p. 565-580.

Roedder, E., 1958, Technique for the extraction and partial chemical analysis of fluid-filled inclusions from minerals: Econ. Geol., v. 53, p. 235-269.

Roedder, E., 1984, Fluid inclusions: Reviews in Mineralogy, v. 12, 646 p.

Ronacher, E., Richards, J.P., and Johnston, M.D., 1999, Environments of ore deposition at the Porgera gold deposit, Papua New Guinea: Proceedings of the 5th biennial SGA meeting: Mineral Deposits: Processes and Processing, London, Balkema, Rotterdam, p. 95-98.

Ronacher, E., Richards, J.P., and Johnston, M.D., 2000a, Evidence for phase separation in high-grade ore zones at the Porgera gold deposit, Papua New Guinea: Mineralium Deposita, v. 35, p. 683-688.

Ronacher, E., Richards, J.P., and Johnston, M.D., 2000b, Evidence for boiling during ore deposition at Porgera, Papua New Guinea: Geological Society of America Program with Abstracts, vol. 32, p. A280.

Ronacher, E., Richards, J.P., Villeneuve, M.E., and Johnston, M.D., in press, Short life-span of the hydrothermal system at Porgera, Papua New Guinea: Laser $^{40}Ar/^{39}Ar$ dates for roscoelite, biotite, and hornblende: Mineralium Deposita Thematic Issue ("Gold Deposits Associated with Alkalic Rocks").

Saunders, J.A., and Schoenly, P.A., 1995, Boiling colloid nucleation and aggregation, and the genesis of bonanza Au-Ag ores of the Sleeper deposit, Nevada: Mineral. Deposita, v. 30, p. 199-210.

Sawkins, F.J., O'Neil, J.R., and Thompson, J.M., 1979, Fluid Inclusion and Geochemical Studies of Vein Gold Deposits, Baguio District, Philippines: Econ. Geol, v. 74, p. 1420-1434.

Sheppard, S.M.F., 1986, Characterization and isotopic variations in natural waters: Reviews in Mineralogy, v. 16, p. 165-184.

Sibson, R.H., 2001, Seismogenic framework for hydrothermal transport and ore deposition, *in*: Richards, J.P. and Tosdal, R.M., eds., Structural Controls on Ore Genesis, Rev. Econ. Geol., v. 14, p. 25-50.

Sibson, R.H., Moore, J.M., and Rankin, A.H., 1975, Seismic pumping: A hydrothermal fluid transport mechanism: Journal of the Geological Society of London, v. 131, p. 653-659.

Sillitoe, R.H., 1997, Characteristics and controls of the largest porphyry copper-gold and epithermal gold deposits in the circum-Pacific region: Australian Journal of Earth Sciences, v. 44, p. 373-388.

Sillitoe, R.H., 2002, Some metallogenic features of gold and copper deposits related to alkaline rocks and consequences for exploration: Mineral. Deposita, v. 37, p. 4-13.

Simmons, S.F., and Browne, P.R.L., 2000, Hydrothermal minerals and prcious metals in the Broadlands-Ohaaki geothermal system: Implications for Understanding low-sulfidation epithermal deposits: Econ. Geol., v. 95, p. 971-1000.

Smith, R.I., 1990, Tertiary plate tectonic setting and evolution of Papua New Guinea, *in* Carman, G.J. and Carman, Z. (eds), Petroleum exploration in Papua New Guinea: Proceedings of the first PNG Petroleum Convention, Port Moresby, p. 229-244.

Spry, P.G., and Thieben, S. E., 1998, The origin of gold-silver telluride deposits of the central Montana alkalic belt: Geological Society of America Program with Abstracts, vol. 30, p. A301.

Spry, P.G., Paredes, M.M., Foster, F., Truckle, J., and Chadwick, T.H., 1996, Evidence for a genetic link between gold-silver telluride and porphyry molybdenum mineralization at the Golden Sunlight deposit, Whitehall, Montana: Fluid inclusion and stable isotope studies: Econ. Geol, v. 91, p. 507-526.

Spycher, N.F., and Reed, M.H., 1989, Evolution of a Broadlands-type epithermal ore fluid along alternative P-T paths: Implications for the transport and deposition of base, precious, and volatile metals: Econ. Geol., v. 84, p. 328-359.

Taylor, B.E., 1986, Magmatic volatiles: Isotopic variation of C, H, and S, *in* Valley, J.W., Taylor, H.P., O'Neil, J.R., eds., Stable isotopes in high-temperature geological processes: Reviews in Mineralogy, v. 16, p. 185-225.

Thomas, A.V., and Spooner, E.T.C., 1992, The volatile geochemistry of magmatic H_2O-CO_2 fluid inclusions from the Tanco zoned granitic pegmatite, southeastern Manitoba, Canada: Geochim. Cosmochim. Acta, v. 56, p. 49-65.

Truesdell, A.H., 1985, Introduction to chemical calculations: Reviews in Economic Geology, v. 1, p. 1-8.

Viets, J.G., Hofstra, A.H., and Emsbo, P., 1996, Solute compositions of fluid inclusions in sphalerite from North American and European Mississippi Valley-Type ore deposits: Ore fluids derived from evaporated seawater: Society of Economic Geologists Special Publication, no. 4, p. 465-482.

Von Damm, K.L., Edmond, J.M., Grant, B., and Measures, C.I., 1985a, Chemistry of submarine hydrothermal solutions at the 21°N, East Pacific Rise: Geochim. Cosmochim. Acta, v. 49, p. 2197-2220.

Von Damm, K.L., Edmond, J.M., Measures, C.I., and Grant, B., 1985b, Chemistry of submarine hydrothermal solutions at Guayamas Basin, Gulf of California: Geochim. Cosmochim. Acta, v. 49, p. 2221-2237.

Wall, V.J., Munroe, S.M., Cameron, G.H., Heinrich, C.A., Cox, S.F., and Walshe, J.L., 1995, Porgera: plumbing and processes of gold mineralization, in Clark, A.H., ed., Giant ore deposits – II. Proceedings of the Second Giant Ore Deposits Workshop, Queens University, Kingston, Ontario, p 649-667.

Walter L.M., Stueber, A.M, and Huston, T.J., 1989, Cl/Br ratios of Illinois basin brines: Constraints on origin of fluids: Geological Society of America Program with Abstracts, vol. 21 p. A316

White, D.E., Hem, J.D., and Waring, G.A., 1963, Chemical composition of subsurface waters: USGS Prof. Paper, 440-F, 1-67.

Wilkinson, J.J., 2001, Fluid inclusions in hydrothermal ore deposits: Lithos, v. 55, p. 229-272.

Zhang, X., and Spry, P.G., 1994, Petrological, mineralogical, fluid inclusion, and stable isotope studies of the Gies gold-silver telluride deposit, Judith Mountains, Montana: Econ. Geol., v. 89, p. 602-627.

Zheng, Y.-F., 1999, Oxygen isotope fractionation in carbonate and sulfate minerals: Geochemical Journal, v.33, p. 109-126.

Table 4-1: Ore and gangue minerals in stage II veins (in approximate order of decreasing abundance)

early late		
quartz	SiO_2	
roscoelite	$K(V,Al)_2Si_3AlO_{10}(OH)_2$	▬▬
pyrite	FeS_2	▬▬—
anhydrite	$CaSO_4$	
Ca-Fe-Mg carbonate	$(Ca,Fe,Mg)CO_3$	—
gold, locally tellurides	Au (~20% Ag)	———
hessite	$AgTe_2$	---------
petzite	*Ag_3AuTe_2*	---------
krennerite	*$(Au,Ag)Te_2$*	---------
calaverite	*$AuTe_2$*	---------
coloradoite	*HgTe*	---------
altaite	*PbTe*	---------
tetrahedrite	$(Cu,Ag,)_{10}(Fe,Zn)_2Sb_3S_{13}$	———
arsenopyrite	FeAsS	———
barite	$BaSO_4$	---------
adularia	$KAlSi_3O_8$	---------
pyrargyrite/prousite	Ag_3SbS_3/Ag_3AsS_3	----------
chalcopyrite	$CuFeS_2$	---------
sphalerite	ZnS	———
marcasite	FeS_2	---------
hematite	*Fe_2O_3*	---------
galena	PbS	----------
acanthite	Ag_2S	----------

Mineral names in italics were not observed in this study (cf. Fleming et al., 1986; Richards et al., 1991)

--- : rare

— : moderately abundant

▬ : abundant

Table 4-2: Average microthermometric data of liquid-rich fluid inclusions hosted by stage II quartz from samples from the footwall diorite. Samples are listed in order of increasing depth.

Sample	Elevation (m a.s.l.)	Th (°C)	Salinity (equiv. wt. % NaCl)	n	Au (ppm)[1]
Roamane Fault Zone:					
P98-2204*	2390	153±15	4.7±0.2, 8.6±0.4	10, 27	n.a.[2]
North Zone:					
P99-120	2335	140±16	6.2±0.2, 8.2±0.3	7, 7	0
P98-1576*	2330	144±9	7.9±0.8	18	4
P98-992	2315	157±18	9.6±0.2	9	15
P98-1466	2190	145±12	8.4±0.5	18	2
P98-1459	2190	154±13	8.1±0.6	36	1
P98-1600	2150	139±22	9.0±0.4	13	5
P98-1448	2120	149±12	8.5±0.3	18	7
P98-1413	2120	127±12	8.3±0.5	37	60
P98-701*	2080	137±13	8.3±1.1	40	11
P98-1379	2030	150±10	8.2±0.7	52	10
P98-1320*	2030	157±14	7.9±0.5	47	8
P98-1631	2020	145±11	7.5±1.0	34	3
P98-846	2000	148±20	8.6±0.4	25	9
P98-1111	1980	132±11	7.8±0.3	6	3
P99-145	1980	160±10	4.5 to 9.2	48	5
P99-178	1945	146±14	5.0±0.0, 7.8±0.4	3, 69	51
P98-611*	1930	156±11	5.0 to 8.7	101	9
P98-612B	1930	142±19	8.3±0.7	38	11
P98-1162	1915	161±11	8.2±0.7	12	9
P98-1537	1910	151±10	4.8±0.1, 6.8±0.6	10, 49	28
P98-1164	1900	163±19	4.5 to 10.2	96	9
P99-066C*	1880	155±16	8.7±0.6	68	2
P99-095C	1875	161±13	8.4±0.4	47	15
P99-197*	1855	148±12	4.8±0.0, 8.1±0.4	4, 36	0
P98-1170	1850	153±13	8.5±0.4	71	0
P98-1835*	1845	167±25	8.3±0.4	27	0
P99-231	1820	152±11	4.4±0.3, 8.8±0.4	13, 5	70

Asterisk (*) denotes samples where vapor-rich inclusions were observed.

[1] Gold assayed over a 2 meter interval

[2] no gold assay data are available for this sample, but it was collected from a high-grade stope within the Roamane Fault Zone

n = number of fluid inclusions analyzed (two values represent the number of inclusions in each of the two salinity groups).

m a.s.l. = meters above sea level

Table 4-3: Results of gas chromatographic analysis. For all other samples, the values represent the gas dissolved in the aqueous liquid phase (see text).

Sample #	N_2[1] mole%	CH_4 mole%	CO_2 mole%	H_20 mole%	C_2H_4 mole%	C_2H_6[2] mole%	COS mole%
Roamane Fault Zone							
P98-2204*	0.04553	0.07431	1.820	98.06	0	0	0
P98-2204A[3]*	0.11011	0.02255	1.108	98.76	0	0	0
North Zone							
P99-120	0.01314	0.03965	1.815	98.12	0	0.00209	0.00793
P98-992A	0.03115	0.10982	1.187	98.67	0	0	0
P98-1466	0.02624	0.03537	2.004	97.93	0	0	0
P98-1459	0.01426	0.03249	1.415	98.54	0	0	0
P98-1600	0.00938	0.02073	1.393	98.58	0	0	0
P98-1448	0.01479	0.03818	1.627	98.32	0	0	0
P98-1320A*	0.04923	0.08114	0.621	99.25	0	0	0
P99-145	0.04043	0.09273	1.384	98.48	0	0	0.00214
P99-178	0.06471	0.12656	0.718	99.09	0.00012	0.00112	0
P99-178X[3]	0.05208	0.10255	0.575	99.27	0	0.00063	0
P98-611*	0.03041	0.04844	1.547	98.37	0	0	0
P98-612B	0.03737	0.03717	1.444	98.48	0	0	0
P98-1162	0.01551	0.03573	1.407	98.54	0	0	0.00069
P98-1537	0.03908	0.09279	0.850	99.02	0	0	0
P99-066C*	0.02413	0.04093	1.106	98.83	0.00003	0.00090	0
P99-095B	0.06388	0.03546	1.846	98.05	0	0	0
P99-197*	0.04013	0.05695	1.227	98.67	0	0.00050	0.00243
P99-197X[3]*	0.04017	0.05789	1.167	98.73	0.00005	0.00061	0.00175
P98-1170	0.02100	0.04539	1.198	98.73	0	0	0.00275
P99-231C	0.02351	0.09177	0.948	98.93	0	0	0.00166

[1] The N_2 peak is a composite peak of N_2+Ar+CO+O_2

[2] C_2H_6 values are combined values of C_2H_6 and C_2H_2

[3] two samples from the same quartz vein were analyzed; differences in concentrations may be due to crusher efficiency and abundance of fluid inclusions in the sample, or to the proportion of liquid- versus vapor-rich inclusions.

* Samples contain liquid-rich and vapor-rich fluid inclusions

Table 4-4: Results of the ion chromatographic analyses in milli moles per liter.

Sample #	Cl^-	Br^-	"ΣS"[1]	Li^+	Na^+	NH_4^+	K^+	Mg^{2+}	Ca^{2+}	Q^+/Q^-	Q^+/Q^-_{corr}[2]
Roamane Fault Zone											
P98-2204	633	1.62	n.a.	0	2008	0	828	n.a.	n.a.	4.47	0.28
P98-2204A[3]	298	0.40	75.1	2.41	448	27	153	0.0	0.0	1.95	0.85
North Zone											
P99-120	529	0.42	99.8	1.72	584	56	81	2.8	184.9	2.20	0.61
P98-992A	429	0.63	26	4.4	620	0	0	0.0	0.0	1.30	0.09
P99-066C	609	0.68	89.6	5.77	876	55	47	0.0	28.3	1.94	1.12
P98-1537	347	0.50	74.4	5.51	479	37	0	0.0	0.0	1.71	0.90
P98-1320A	575	0.69	42.3	3.08	776	16	100	2.5	15.7	1.63	1.09
P98-1448	485	0.71	89.8	5.16	884	23	0	0.0	0.0	1.68	0.73
P98-1466	538	0.75	96.9	4.58	996	18	30	0.0	0.0	1.65	0.67
P98-1170	539	0.52	n.a.	1.58	829	0	372	n.a.	n.a.	2.23	1.03
P99-145	353	0.36	0.0	6.04	462	12	121	0.0	0.0	2.00	0.65
P99-178	474	0.65	18.5	6.47	654	43	28	7.0	0.0	2.20	1.27
P99-178X[3]	279	0.53	n.a.	4.85	545	n.a.	0	n.a.	n.a.	1.97	0.94
P98-611	335	0.31	42.1	8.80	473	20	371	0.0	0.0	2.50	0.85
P98-1600	420	0.56	69.9	5.44	780	14	24	0.0	0.0	1.70	0.73
P98-1162	446	0.65	71.1	3.40	780	12	0	0.0	0.0	1.54	0.68
P98-1459	356	0.36	44.6	3.89	557	30	0	0.0	0.0	1.94	0.72
P98-612B	495	0.54	76.6	3.32	904	14	281	0.0	0.0	2.05	0.94
P99-095B	510	0.63	226.4	2.97	1126	10	28	0.0	0.0	1.31	0.65
P99-197	399	0.50	90.2	4.32	731	23	0	0.0	0.0	1.66	0.78
P99-197X[4]	310	0.28	n.a.	2.60	613	n.a.	n.a.	n.a.	n.a.	1.98	0.66
P99-231C	421	0.51	32.6	1.25	659	0	0	0.0	0.0	1.36	0.67

[1] Values for "ΣS" were analyzed as SO_4^{2-} because sulfur species are partially oxidized to SO_4^{2-} during analysis; however, because the oxidation may not be complete, "ΣS" is presented in quotation marks.

[2] Q^+/Q^- is the cation/anion ratio and Q^+/Q^-_{corr} is the cation/anion ratio corrected for the presence of CO_2 dissolved as HCO_3^- (after Channer et al., 1992; see text for details).

[3] Two samples from the same quartz vein were analyzed; differences in concentrations may be due to crusher efficiency and relative abundance of low versus high salinity fluid inclusions in the sample.

n.a. = not analyzed.

Table 4-5: Oxygen and hydrogen isotopic data in permil relative to VSMOW. Hydrogen isotopic compositions were obtained from bulk fluid inclusion (FI) analyses in quartz.

sample #	$\delta^{18}O_{qtz}$ (‰)	Average Th (°C)	$\delta^{18}O_{H_2O}$ (‰)[1]	$\delta^{18}O_{H_2O}$ (‰)[2]	δD_{H_2O} (‰)
Roamane Fault Zone					
P98-2204	18.3	156	3.3	5.2	-64
North Zone					
P98-1576	16.4	144	0.6	2.7	-63
P98-981	16.5	no workable FI			
P98-992	15.2	157	0.6	2.5	-67
P98-1466	14.9	145	-0.8	1.3	-55
P98-1600	15.1	139	-1.1	1.1	-57
P98-1448	13.9	149	-1.4	0.6	-77
P98-1413	16.5	127	-0.9	1.5	
P98-701	15.8	137	-0.6	1.2	
P98-1631	17.0	145	1.3	3.4	-64
P98-1379	14.8	150	-0.5	1.6	-58
P98-846	15.9	148	0.5	2.6	-53
P98-1111	16.4	132	-0.5	1.8	
P98-611	14.6	156	-0.1	1.9	-57
P98-1162	14.5	161	0.2	2.1	-52
P98-1537	13.9	151	-1.2	0.8	-81
P98-1164	17.6	163	3.5	5.4	-64
P98-1170	16.9	153	1.2	3.2	-66
P98-1833	16.7	no workable FI			-76
P98-1835	17.9	167	4.1	5.9	

[1]: calculated assuming average Th ≈ Tt; fractionation equation of Clayton et al. (1972)
[2]: calculated using average Th+25°C; fractionation equation of Clayton et al. (1972)

Table 4-6: Carbon isotopic values for carbonate and organic carbon from various rocks from Porgera, stage II vein carbonate, and from CO_2 in fluid inclusion fluid. $\delta^{13}C$ values are reported in ‰ relative to V-PDB. $\delta^{13}C_{carb}$ data of the sedimentary rocks are similar to the data of Richards and Kerrich (1993). $\delta^{18}O_{fluid}$ calculated using the equation of Zheng (1999) for ankerite and a temperature of 160°C.

sample #	Comments	$\delta^{13}C_{carb}$	$\delta^{13}C_{org\text{-}shale}$	$\delta^{13}C_{CO_2}$	$\delta^{18}O_{carb}$	$\delta^{18}O_{fluid}$
		‰	‰	‰	‰	‰
P98-1538	stage II carbonate	-2.4			16.6	3.6
P98-1532	stage II carbonate	-2.6			15.5	2.5
P98-1325	stage II carbonate	-2.5			16.2	3.2
P98-1537	stage II carbonate	-2.7			16.0	3.0
P98-1344	stage II carbonate	-3.3			15.2	2.2
P144	carbonaceous mudstone (Om Fm)	-1.5	-20.0			
RJR-69	cm, altered (qtz, carbonate, pyrite; Chim Fm)	-4.6	-22.9			
RJR-75	cm, altered (qtz, carbonate, pyrite; Chim Fm)	-5.4	-20.3			
P139	mudstone (Chim Fm)	-0.8	-20.5			
P141	siltstone	0.0	-16.8			
RJR-68	cm, altered (qtz, carbonate, pyrite; Chim Fm)	-4.0	-23.6			
RJR-74	calc-arenite (disseminated py; altered?; Chim Fm)	-4.3				
RJR-73	calc-arenite (Chim Fm)	-1.4				
P143[1]	limestone (Nipa Gr)	1.2				
P98-2204	inclusion fluid			-9.5		

carb: carbonate
cm: carbonaceous mudstone
org: organic
qtz: quartz
py: pyrite
Fm: formation
Gr: group
[1] Nipa Gr limestone overlies the Porgera deposit; analysis from Richards and Kerrich (1993)

Table 4-7: $\delta^{34}S$ data for pyrite and late, vug-filling anhydrite/gypsum from the North Zone and the Roamane Fault Zone in permil relative to VCDT.

Sample	Mineral	Area	$\delta^{34}S$ (‰)
P98-2204	stage II pyrite	Roamane Fault Zone	6.0
P98-1466	stage II pyrite	North Zone	-8.2
P98-1459	stage II pyrite	North Zone	2.5
P98-1600	stage II pyrite	North Zone	-6.7
P98-145	stage II pyrite	North Zone	1.7
P98-1162	stage II pyrite	North Zone	6.1
P98-1170	stage II pyrite	North Zone	-9.4
P99-197	stage II pyrite	North Zone	1.0
P97-2	anhydrite, vug-filling	North Zone	12.4
P97-6	anhydrite, vug-filling	North Zone	17.5
P97-16	gypsum, vug-filling	North Zone	14.7
P97-93	anhydrite, vug-filling	Roamane Fault Zone	16.0
P97-94	anhydrite, vug-filling	Roamane Fault Zone	16.0
P97-95	anhydrite, vug-filling	Roamane Fault Zone	17.0
P97-96	anhydrite, vug-filling	Roamane Fault Zone	17.2
P98-2206	anhydrite, vug-filling	Roamane Fault Zone	17.2
P144	mudstone (Om Fm)	host rocks[1]	2.1
RJR-145	calc-arenite	host rocks[1]	5.9
RJR-68	mudstone (Chim Fm)	altered host rocks[1]	-12.7

Fm: formation

[1] sulfur in pyrite

Table 4-8: Average inclusion fluid salinity corrected for the presence of CO_2 in the fluid inclusions, and salinity estimated from Cl^- and Na^+ concentrations analyzed by ion chromatography (see Table 4-4). Note that only the high salinity values was corrected for CO_2 because clathrate was not observed in the low salinity inclusions.

Sample	Salinity[1] (uncorrected; equiv. wt. % NaCl)	CO_2 mole%	Salinity corrected for CO_2 (equiv. wt. % NaCl)[2]	Salinity based on Cl^- concentration (equiv. wt. % NaCl)[3]	Salinity based on Na^+ concentration (equiv. wt. % NaCl)[4]
P99-120	6.2, 8.2	1.815	5.6	3.2	5.4
P98-992	9.6	1.187	8.0	2.6	6.0
P98-2204A	4.7, 8.6	1.108	5.9	1.8	3.7
P98-1466	8.4	2.004	5.5	3.2	6.7
P98-1459	8.1	1.415	6.1	2.2	5.1
P98-1600	9.0	1.393	7.0	2.5	5.6
P98-1448	8.5	1.627	6.1	2.9	7.5
P98-1320	7.9	0.621	7.0	3.5	4.6
P99-145	7.1	1.384	5.0	2.1	6.0
P99-178	5.0, 7.8	0.718	6.7	2.9	5.1
P98-612B	8.3	1.444	6.2	3.0	5.8
P98-611	7.4	1.547	5.1	2.1	6.1
P98-1162	8.2	1.407	6.1	2.7	5.3
P98-1537	4.8, 6.8	0.850	5.5	2.1	4.1
P99-066C	8.7	1.106	7.1	3.7	6.9
P99-095C	8.4	1.846	5.7	3.1	5.9
P99-197	4.8, 8.1	1.227	6.3	2.4	4.6
P98-1170	8.5	1.198	6.8	3.2	4.9
P99-231	4.4, 8.8	1.182	7.0	2.7	4.9

[1] Salinity calculated from ice melting point. The two values for salinity represent the low and the high salinity group.
[2] Salinity calculated according to the method outlined by Hedenquist and Henley (1985).
[3] Salinity calculated assuming all Cl^- analyzed by ion chromatography is present in the fluid as NaCl.
[4] Salinity calculated assuming all Na^+ analyzed by ion chromatography is present in the fluid as NaCl.

Table 4-9: Composition of the starting solution used for numerical modeling expressed as component species. See text for details.

T (°C)	170
pH	5.00
$\log f_{O_2}$	–42.59

Component Species	Concentration (total molality)
Cl^-	7.3×10^{-1}
$SO_4^{=}$	1.2×10^{-2}
HCO_3^-	6.5×10^{-1}
HS^- [1]	-1.1×10^{-2}
SiO_2	2.4×10^{-3}
Al^{+++}	7.3×10^{-8}
Ca^{++}	2.8×0^{-5}
Mg^{++}	5.5×10^{-6}
Fe^{++}	2.9×10^{-8}
K^+	3.0×10^{-2}
Na^+	7.1×10^{-1}
NH_4^+	2.9×10^{-2}
Au^+	5.6×10^{-9}

[1]: The negative value of HS^- is a reflection of the relatively higher abundance of SO_4^{2-} than HS^- in this water (see text for details).

Table 4-10: Chemical composition of the formation water use for the CHILLER fluid mixing run.

T (°C)	150
pH	6.1
log f_{O_2}	-44.16

Component Species	Concentration (total molality)
Cl^-	5.2×10^{-1}
SO^{4--}	3.6×10^{-2}
HCO_3^-	2.3×10^{-2}
HS^-	3.3×10^{-6}
SiO_2	1.7×10^{-3}
Al^{+++}	2.9×10^{-7}
Ca^{++}	3.2×10^{-3}
Mg^{++}	1.4×10^{-4}
Fe^{++}	1.1×10^{-6}
K^+	2.8×10^{-3}
Na^+	5.9×10^{-1}
Au^+	2.3×10^{-12}

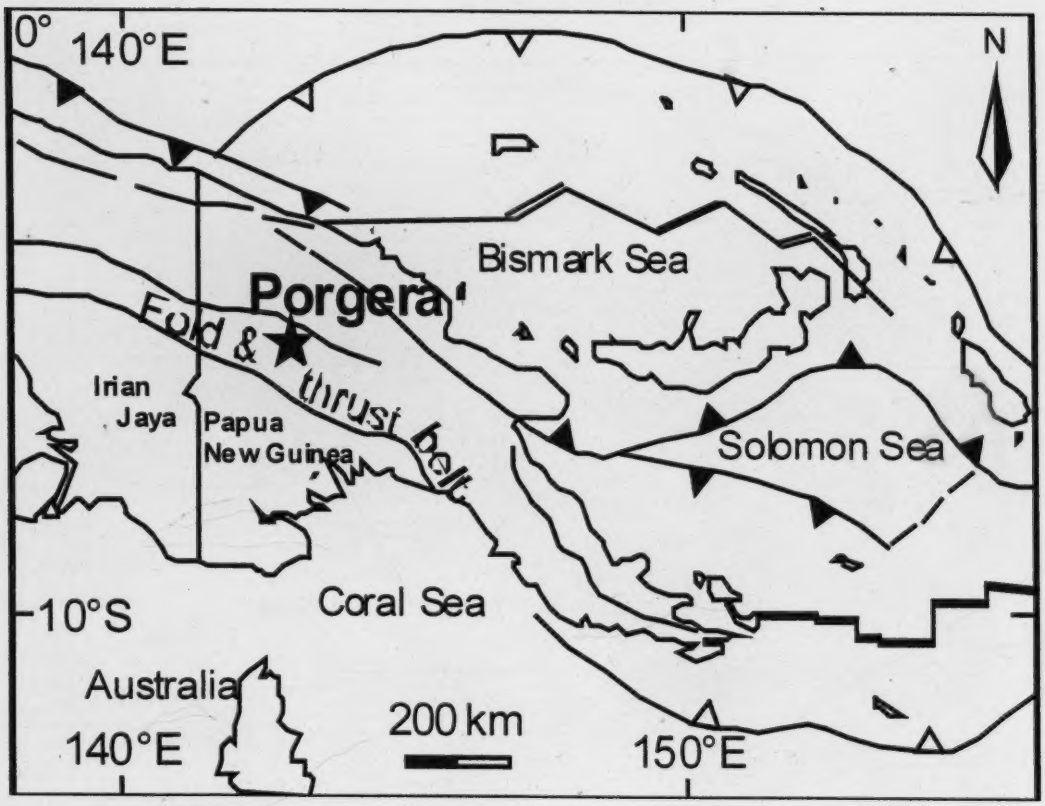

Figure 4-1: Simplified map of Papua New Guinea showing the location of the Porgera gold mine in the Pliocene fold and thrust belt. Modified after Richards et al. (1990) and Smith (1990).

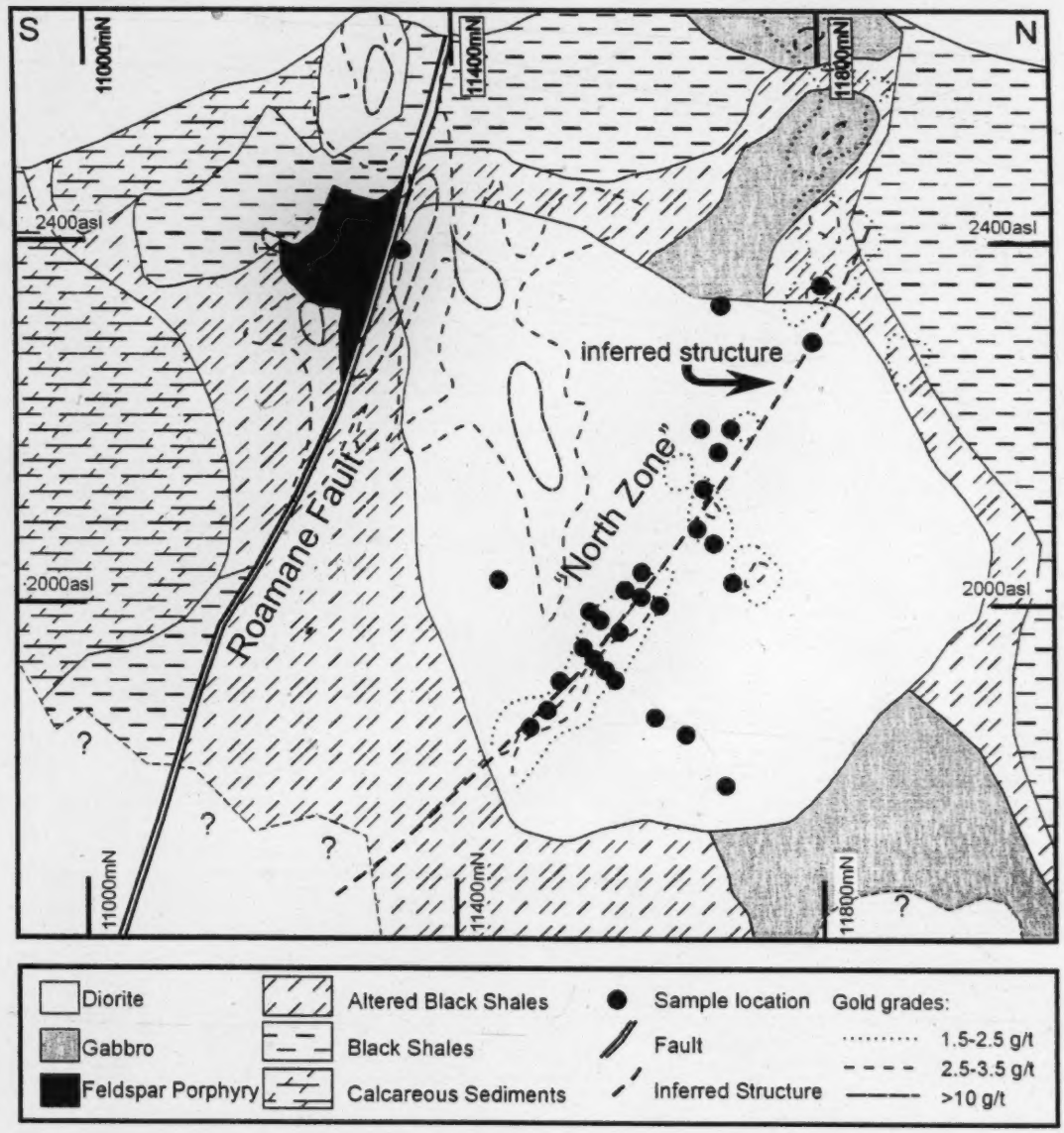

Figure 4-2: Sketch NS cross section through the Porgera mine showing a dioritic intrusion in the center, and smaller gabbroic and feldspar porphyry bodies. The intrusions are hosted by altered black shales that grade into unaltered black shales. Samples were taken along a high-grade ore zone, the "North Zone", that strikes parallel to the Roamane Fault, a steeply dipping normal fault. The black dots represent sample locations projected onto this section and they mimic the North Zone. a.s.l. is the elevation above sea level, and the northing refers to the Porgera mine grid. Contour lines refer to average gold grades modeled by Porgera Joint Venture staff (grades averaged over 10 × 10 × 15 meter blocks from assays of 2m of drillcore, individual assays are up to several hundred grams per tonne).

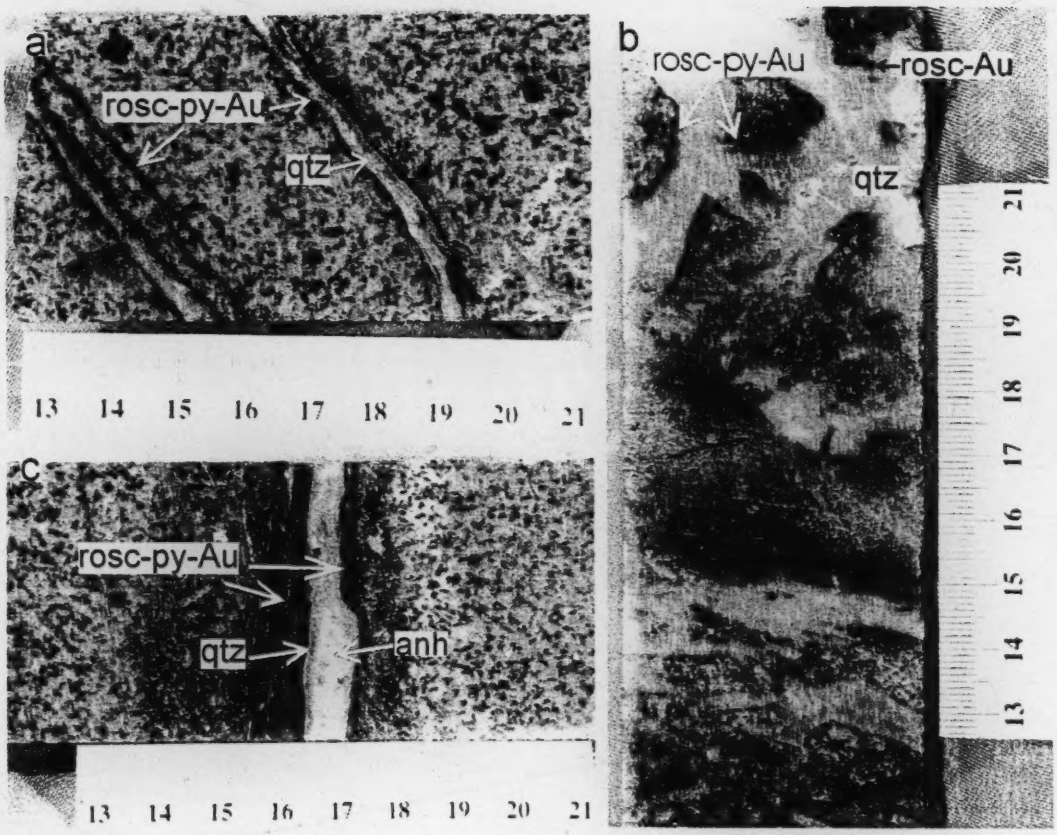

Figure 4-3: Drill core photographs of typical stage II quartz-roscoelite-pyrite-gold veins. (a) 4mm-wide quartz veinlets with roscoelite-pyrite-gold rimming the vein edges (P99-061B); (b) breccia vein with roscoelite-pyrite-gold rimming parts of the breccia clasts (P99-016); (c) stage II vein with roscoelite-pyrite-gold band forming the vein edge, followed by a layer of quartz, and anhydrite filling the vein center (P99-093). Scale in centimeters. Au = gold, anh = anhydrite, py = pyrite, qtz = quartz, rosc = roscoelite.

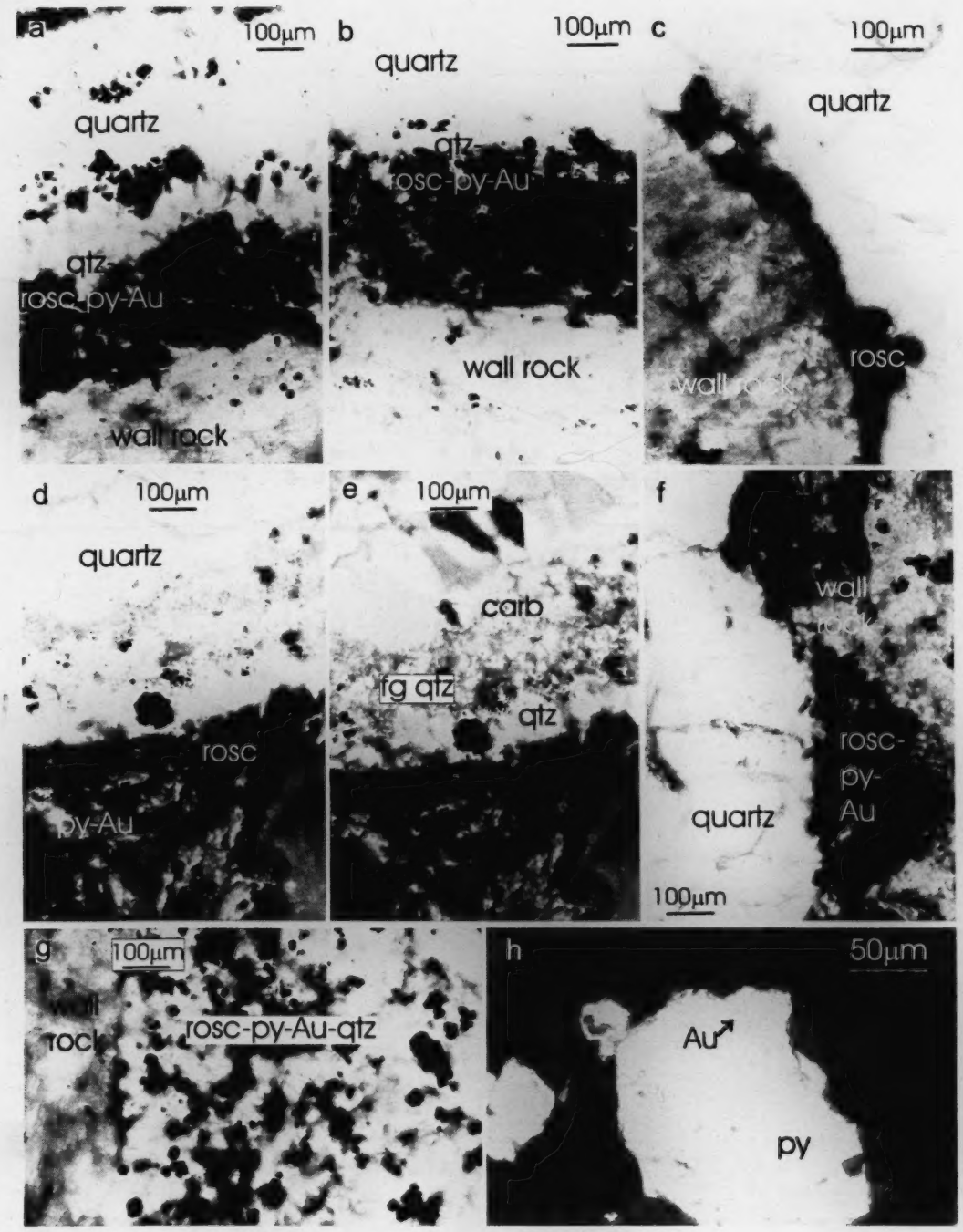
a
100μm
quartz
qtz-
rosc-py-Au
wall rock
b
100μm
quartz
qtz-
rosc-py-Au
wall rock
c
100μm
quartz
rosc
d
100μm
quartz
rosc
py-Au
e
100μm
carb
fg qtz
qtz
f
wall
rosc-
py-
Au
quartz
100μm
g
100μm
wall
rock
rosc-py-Au-qtz
h
50μm
Au
py

Figure 4-4: Photomicrographs of stage II veins. (a) and (b) Wall-rock rimmed by a layer of roscoelite-pyrite-gold with minor quartz and followed by coarse-grained comb quartz (P98-1157; P98-618); (c) band of roscoelite-pyrite-gold and minor quartz forming the vein margin (P98-932); (d) roscoelite and pyrite±gold in wall rock; the first layer in the vein consists of quartz which is followed by a band of fine-grained quartz, pyrite, and carbonate, and coarse-grained quartz in the vein center (P98-1466); (e) same as (d) photographed under crossed polarizing light; the bright colors of quartz under polarized light are due to the thickness of the section (~80 to 100μm; fluid inclusion section); (f) roscoelite and pyrite±gold in the wall-rock (P98-618); (g) intergrown quartz-pyrite-roscoelite forming the vein edge (P98-1234A); and (h) gold in pyrite in wall-rock (P97-16; photo from Richards, 1998). Au = gold, py = pyrite, qtz = quartz, rosc = roscoelite.

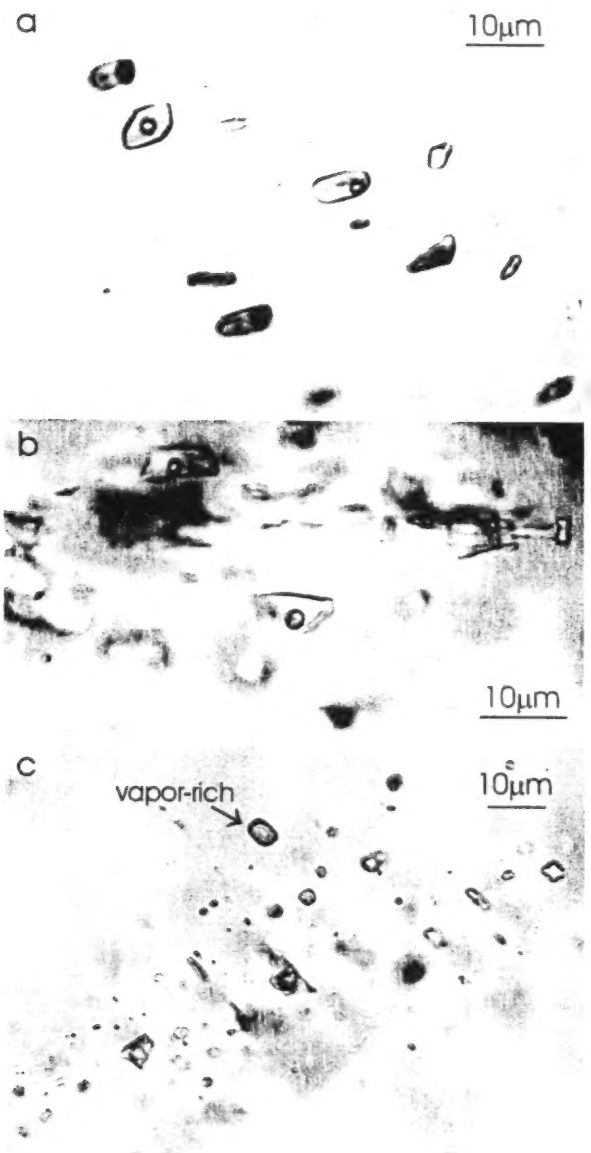

Figure 4-5: Photomicrographs of fluid inclusion assemblages from quartz in quartz-roscoelite-pyrite-gold veins. (a) Group of primary inclusion (P99-197). (b) primary fluid inclusion in growth zone (P98-701); (c) liquid-rich and vapor-rich inclusions in growth zone (P99-1320).

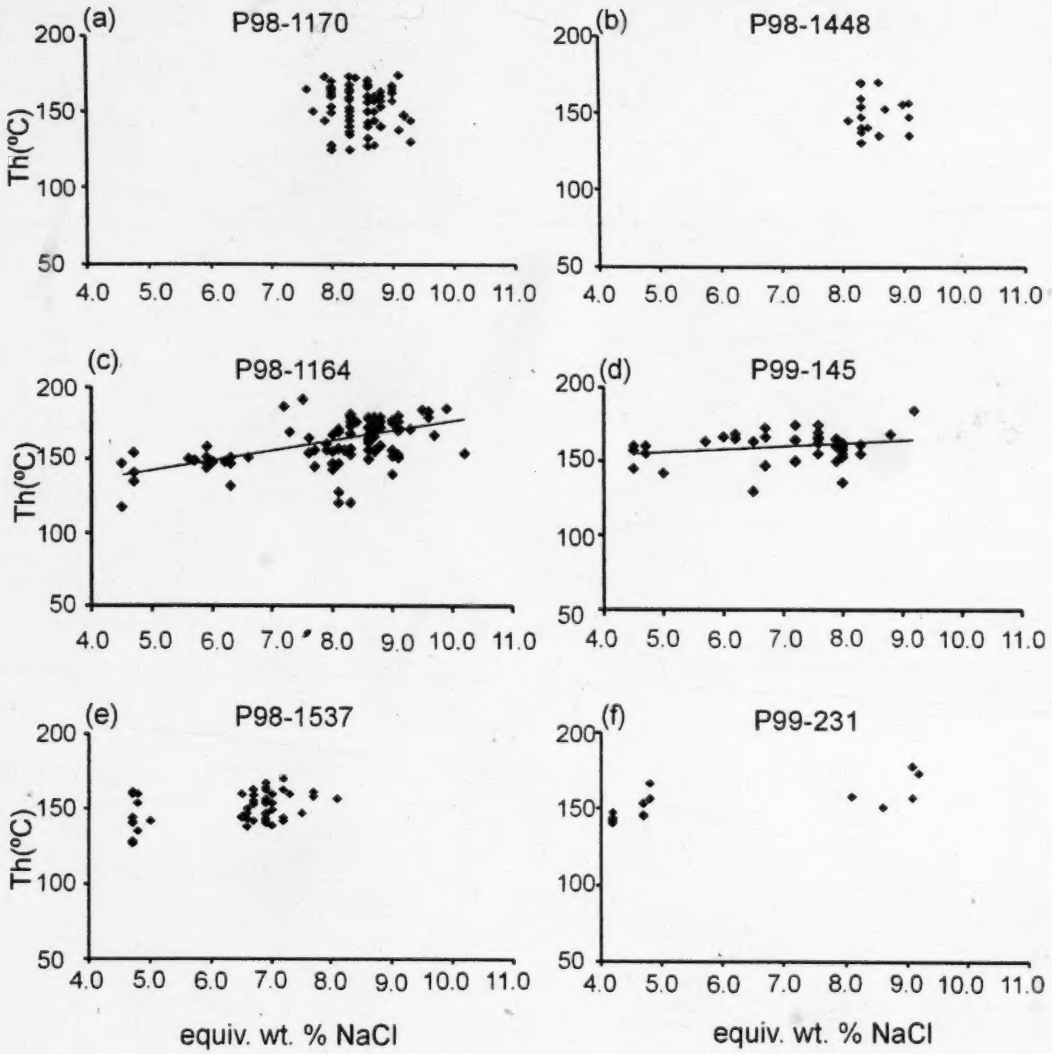

Figure 4-6: Apparent salinity (in equivalent weight percent NaCl) versus homogenization temperature (Th) of representative samples of quartz-roscoelite-pyrite-gold veins. Three distinct patterns can be recognized: the examples in (a) and (b) show a single group of salinity between ~8 and 9 equiv. wt. %; examples in (c) and (d) exhibit a range of salinities from ~4 to ~10 equiv. wt. % NaCl; regression lines indicated slightly lower temperatures for the low salinity inclusions; and examples (e) and (f) show a bimodal salinity distribution with one cluster at ~4-5 and a second cluster at ~7 and ~9 equiv. wt. % NaCl respectively.

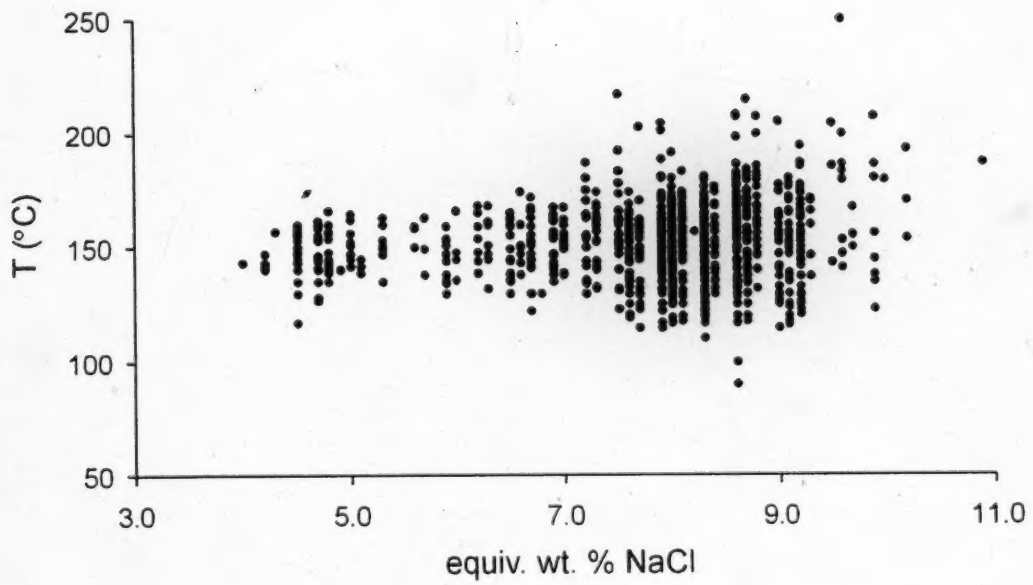

Figure 4-7: Apparent salinity (in equivalent weight percent NaCl) versus homogenization temperature (Th) of *all* samples from the North Zone.

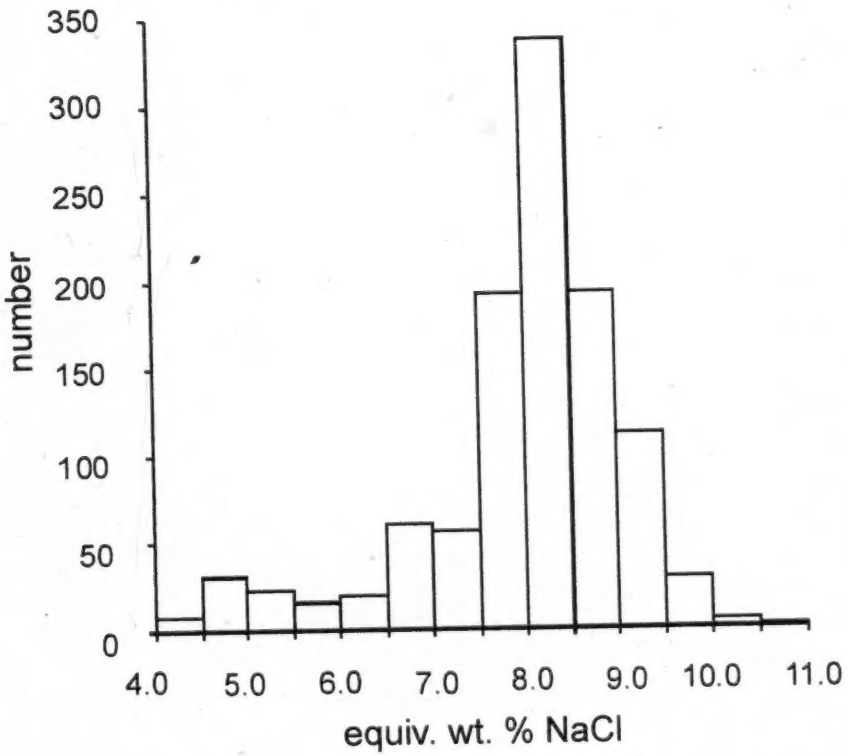

Figure 4-8: Histogram of all measured salinities. The salinity ranges from ~4 to ~10 equiv. wt. % NaCl, but the high salinity population is clearly more dominant.

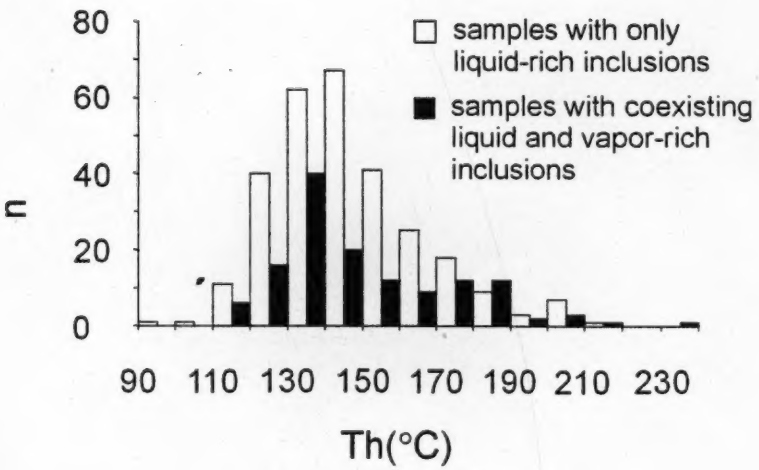

Figure 4-9: Histogram showing the distribution of Th of samples that contained liquid-rich inclusions only (white bars) and samples that contained vapor-rich inclusions in addition to liquid-rich inclusions (black bars). n = number of samples. Note that the distributions are broadly similar except for a possible bimodal distribution for the samples from assemblages where vapor-rich inclusions were observed.

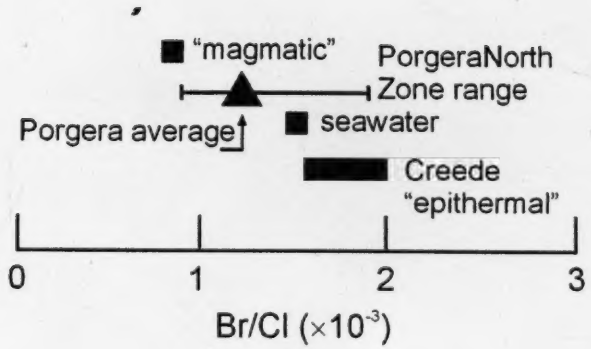

Figure 4-10: Comparison of Br^-/Cl^- ratios from various environments. The average Br^-/Cl^- of the Porgera fluid falls between Br^-/Cl^- of seawater and magmatic water; data from Böhlke and Irwin (1992).

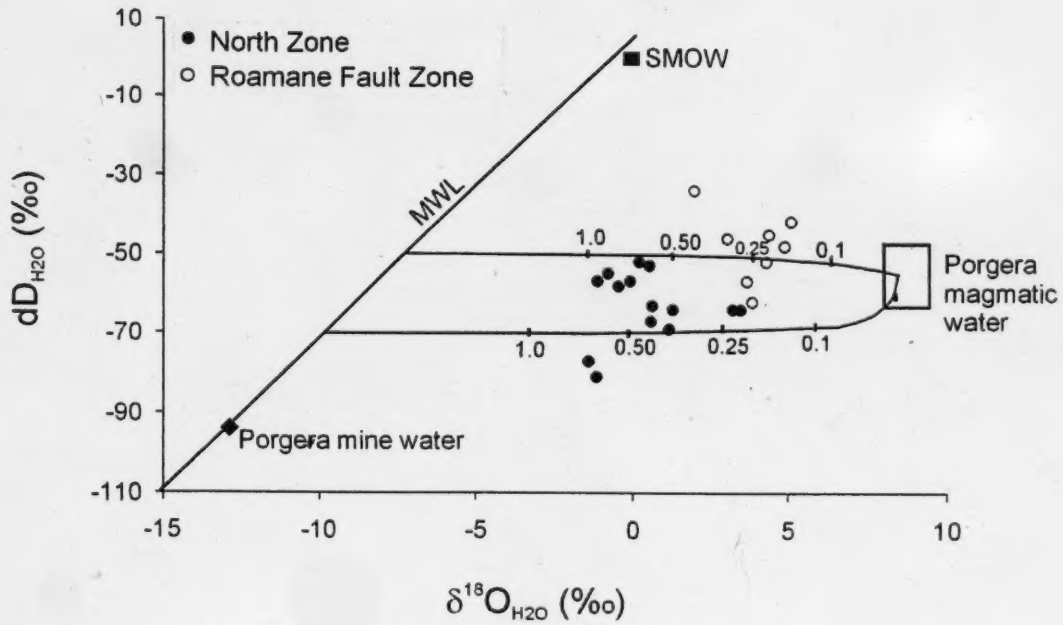

Figure 4-11: Oxygen and hydrogen isotope data of water in equilibrium with stage II quartz. $\delta^{18}O_{H_2O}$ was calculated from $\delta^{18}O_{qtz}$ using the fractionation equation of Clayton et al. (1972) and measured homogenization temperatures (assumed to be the trapping temperatures; see text for details). The isotopic composition of present day Porgera mine water was plotted for reference (data from Richards and Kerrich, 1993). The filled circles represent data from the North Zone (this study) whereas the open circles represent data from the Roamane Fault Zone from Richards and Kerrich (1993; see text for details). The isotopic exchange paths were calculated using the method of Field and Fifarek (1985), and the numbers along the exchange paths are water/rock ratios. Data Porgera magmatic water from Richards and Kerrich (1993). MWL = meteoric water line.

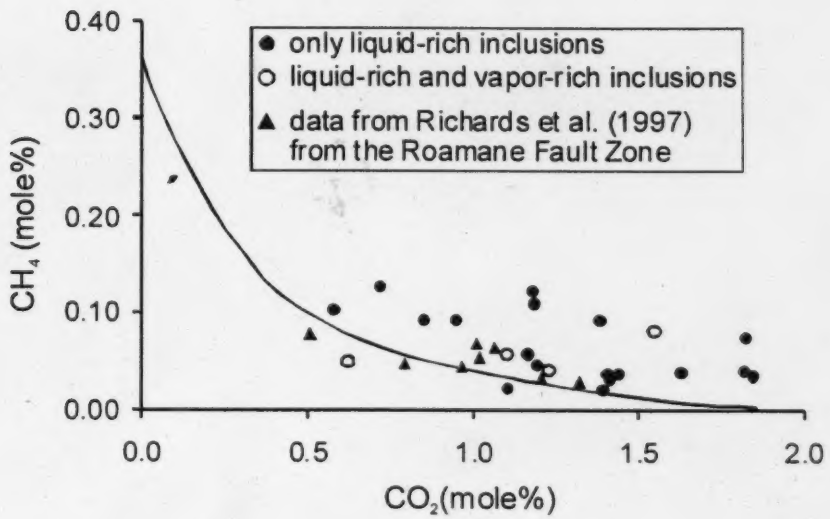

Figure 4-12: Solubility curve of CO_2 and CH_4 in a 5 wt % NaCl solution at 150°C and 345 bar from Price (1981) and Duan et al. (1992). Data from Porgera are overlain on the curve. Black circles represent samples that contain liquid-rich inclusions only, and open circles represent samples that contain vapor-rich inclusions in addition to liquid-rich inclusions. Triangles represent data from Richards and Kerrich (1993).

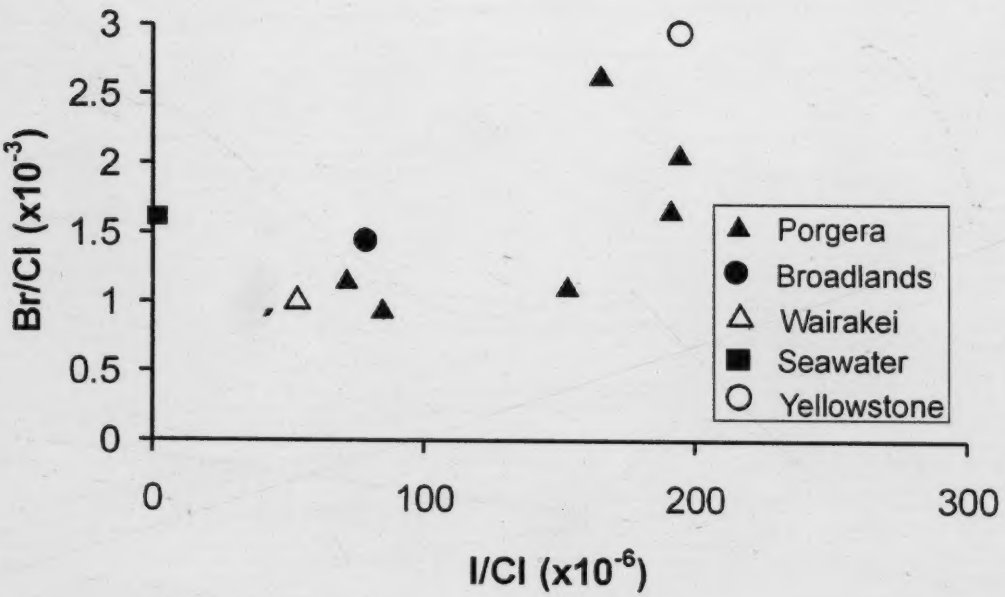

Figure 4-13: Br^-/Cl^- versus I^-/Cl^-; data from Richards et al. (1997) and Böhlke and Irwin (1992). Br^-/Cl^- of seawater falls within the range of Br^-/Cl^- of the Porgera fluid, but the two fluids are distinctly different in their I^-/Cl^- ratios. Values from Broadlands and Wairakei (New Zealand) and Yellowstone (USA) for reference (from Böhlke and Irwin,1992).

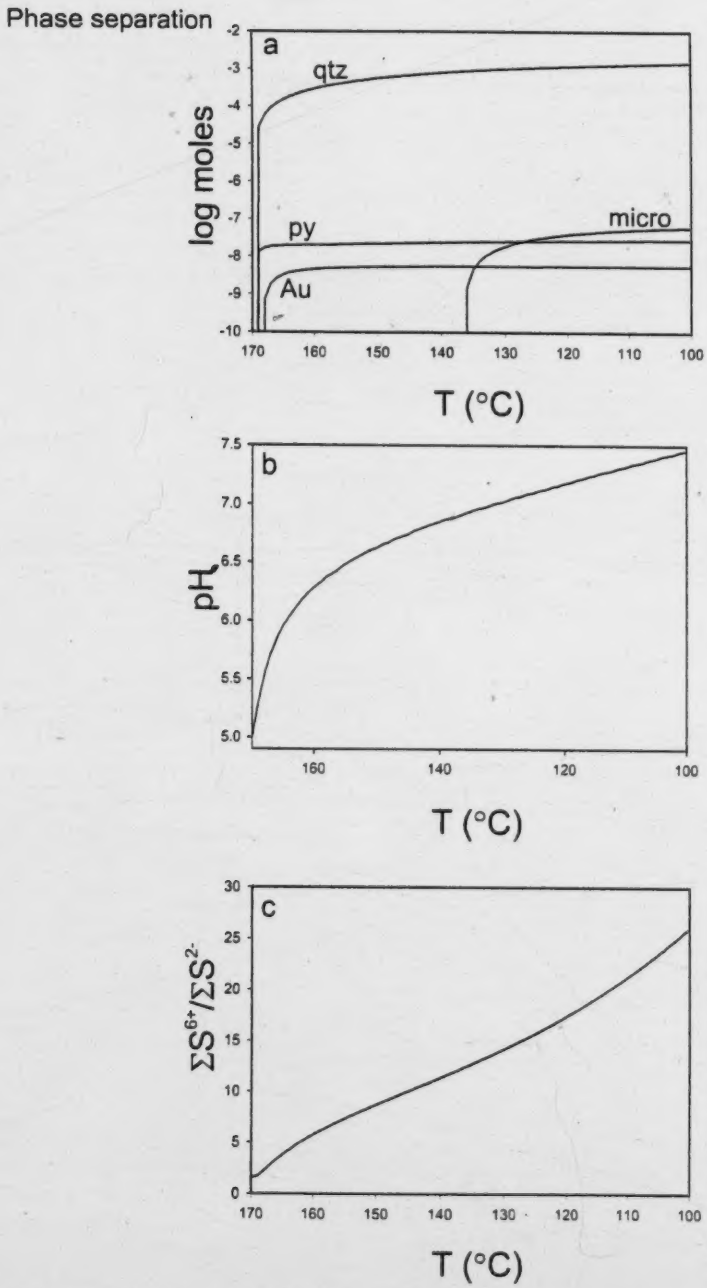

Figure 4-14: (a) Minerals precipitating upon adiabatic boiling from 170°C to 100°C. The plot is to be read from left to right as phase separation proceeds from higher to lower temperature. The curves symbolize minerals precipitating from the solution. (b) Change of pH during phase separation. (c) S^{6+}/S^{2-} is an indication of the redox state of the fluid (Cooke and McPhail, 2001). Abbreviations: Au = gold, micro = microcline, py = pyrite, qtz = quartz.

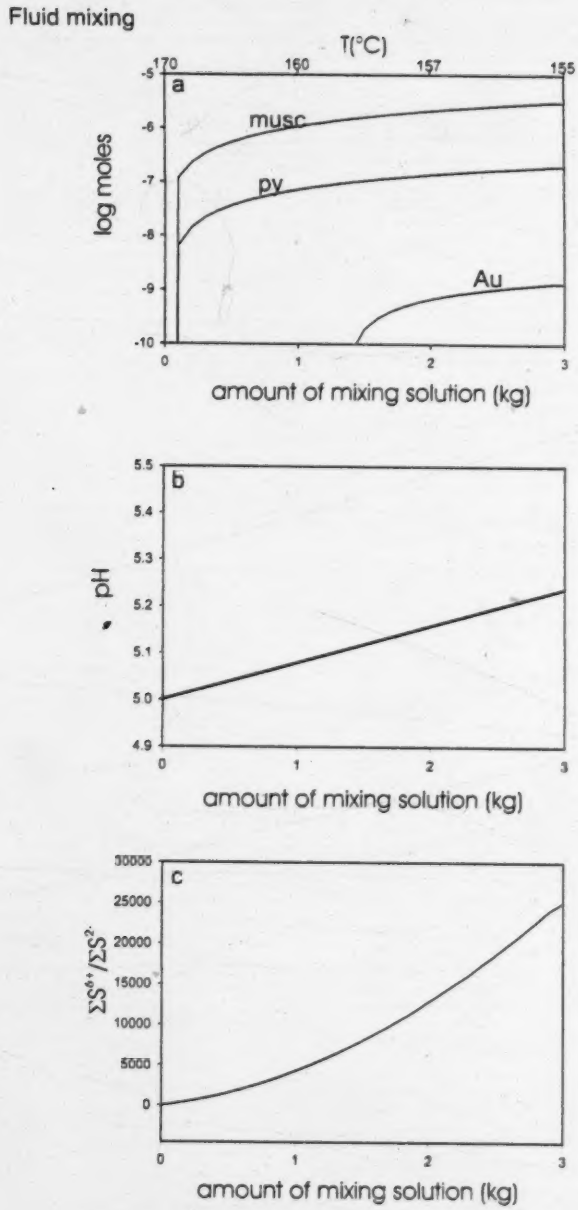

Figure 4-15: Modeling results for mixing of 1 kg of starting solution (170°C) with up to 3 kg of formation water (150°C). The amount of mixing solution (in kilograms) increases from left to right. (a) Minerals precipitating from the solution. The temperature change is indicated on the top axis of the plot. (b) Development of pH during mixing. (c) Evolution of the redox state of the fluid. Abbreviations: Au = gold, musc = muscovite, py = pyrite.

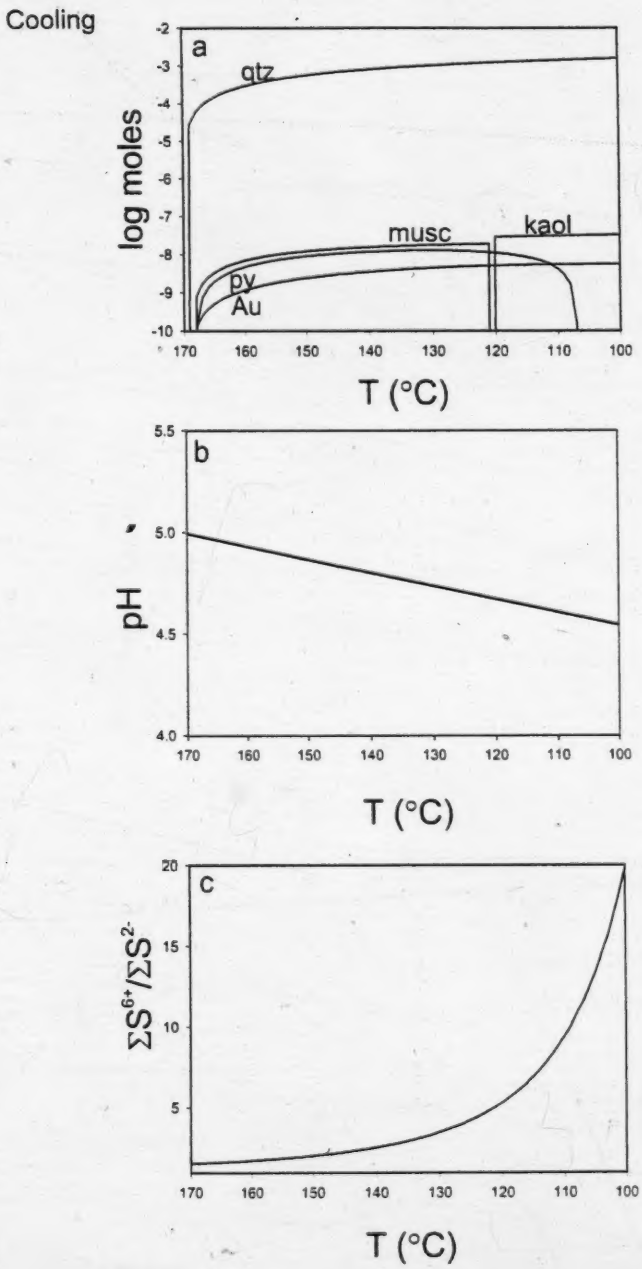

Figure 4-16: Modeling results of simple cooling. (a) Mineral assemblage formed upon cooling from 170°C to 100°C. (b) Evolution of pH during cooling. (c) Evolution of the redox state of the fluid. Au = gold, musc = muscovite, py = pyrite, qtz = quartz.

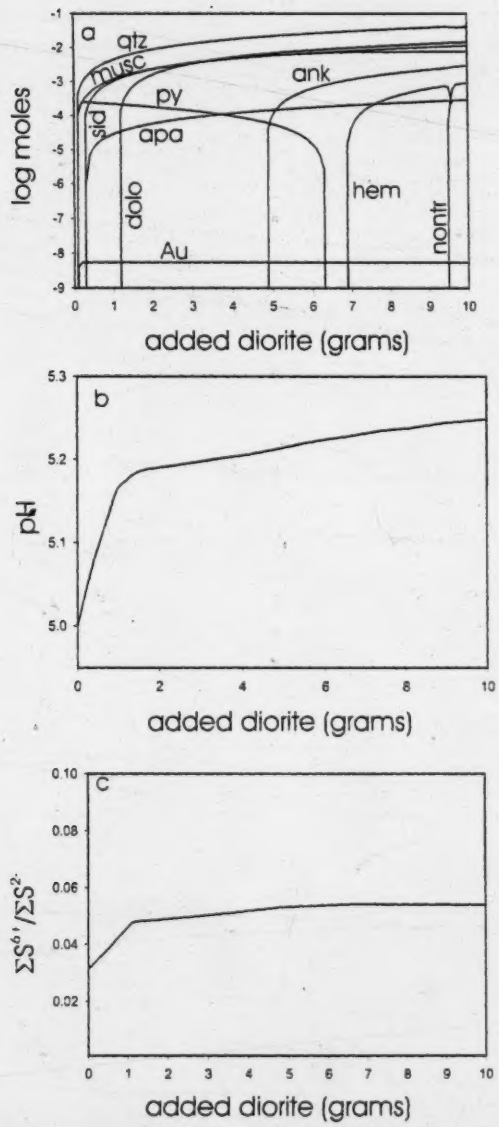

Figure 4-17: (a) Minerals precipitated upon interaction of the starting solution with dioritic wall rock. Diorite (composition from Richards, 1990b) is titrated into 1 kilogram of solution. The amount of titrated diorite increases from 0 to 10 gram of diorite titrated. (b) pH evolution during water-rock interaction. (c) Redox state of the fluid. Abbreviations: ank = ankerite, apa = apatite, Au = gold, dolo = dolomite, hem = hematite, musc = muscovite, ntr = nontronite, py = pyrite, qtz = quartz, sid = siderite.

Chapter 5

Conclusions

This dissertation contributed to a more comprehensive understanding of ore deposition at the Porgera gold deposit by determining the duration of ore formation, characterizing the hydrothermal fluid believed to have been responsible for vein formation, and by integrating the available data to a consistent ore deposition model.

It was possible for the first time to constrain well the age of the main ore stage at Porgera (roscoelite: 5.99 ± 0.08 Ma). Relate this roscoelite age to the age of the earliest stage of vein formation (biotite: 5.98 ± 0.13 Ma) allowed to constrain the duration of the mineralizing event, which could then be tied to the age of the intrusions (biotite: 5.99 ± 0.11) that are associated with the deposit. Thus, it was shown that ore formation immediately succeeded the intrusive event, further underlining the link between the alkalic intrusions and the gold deposit (Richards et al., 1991). These results further indicate that even short-lived hydrothermal systems are capable of producing world-class ore deposits, and that the duration of the mineralizing process may therefore not be directly related to the magnitude of the metal enrichment (cf. Stein and Cathles, 1997).

The fluid that was responsible for the formation of gold-bearing veins was characterized using fluid inclusion microthermometry and solute chemistry. Vapor-rich fluid inclusions were observed locally and analyzed for the first time, which was a crucial piece of evidence confirming that the conditions for phase separations were locally favorable during stage II quartz formation. In one sample from near the Roamane Fault it was even possible to directly tie gold precipitation to this process (Ronacher et al., 2000b).

The relatively high salinities of inclusions hosted by stage II quartz (~6 equiv. wt % NaCl; corrected for CO_2) suggest the contribution of magmatic water to the hydrothermal fluid, but a second, lower salinity fluid was also present during stage II vein formation. In some cases, a continuous salinity trend in the fluid inclusion record suggests that fluid mixing took placed locally. In addition, gold was observed in the

wall rock adjacent to stage II veins which indicates that water—wall rock interaction played a role in ore formation. The results of numerical modeling indicate that cooling may have been a dominant vein formation mechanism. Thus, we showed that four distinct processes – cooling, phase separation, fluid mixing, and water/rock interaction, and possibly combinations of these processes – were involved in ore formation, and it was possible to show that apparently contradictory evidence can be resolved to form a multi-process model that explains field observations, analytical data, and modeling results.

References

Richards, J.P., McCulloch, M.T., Chappell, B.W., and Kerrich, R., 1991, Sources of metals in the Porgera gold deposit, Papua New Guinea: Evidence from alteration, isotope, and noble metal geochemistry: Geochim. Cosmochim. Acta, v. 55, p. 565-580.

Ronacher, E., Richards, J.P., and Johnston, M.D., 2000b, Evidence for boiling during ore deposition at Porgera, Papua New Guinea: Geological Society of America Program with Abstracts, v. 32, p. A280.

Stein, H.J., and Cathles, L.M., 1997, A Special Issue on timing and duration of hydrothermal events: Preface: Econ. Geol., v. 92, p. 763-765.